



FAKULTÄT FÜR
MASCHINENBAU

Phase Field Based Study of Microstructure Evolution in Solidification of Mo-rich Mo-Si-B Alloys

Dissertation

zur Erlangung des akademischen Grades

Doktoringenieur (Dr.-Ing.)

von M.Sc. Omid Kazemi
geb. am 17.08.1987 in Amol-Iran
genehmigt durch die Fakultät für Maschinenbau
der Otto-von-Guericke-Universität Magdeburg

Gutachter: Prof. Dr.-Ing. Habil. Thorsten Halle
Prof. Dr.-Ing. Daniel Juhre
Prof. Dr.-Ing. habil. Manja Krüger

Promotionskolloquium am 29.01.2021

Declaration of Honor

I hereby declare that I prepared this thesis without prohibited external assistance and that none other than the listed references and tools have been used. I did not make use of any commercial consultant concerning graduation. A third party did not receive any non-monetary perquisites neither directly nor indirectly for activities which are connected with the contents of the presented thesis. All sources of information are clearly marked, including my own publications. In particular I have not consciously:

- Fabricated data or rejected undesired results
- Misused statistical methods with the aim of drawing other conclusions than those warranted by the available data
- Plagiarized data or publications
- Presented the results of other researchers in a distorted way

I do know that violations of copyright may lead to injunction and damage claims of the author and also to prosecution by the law enforcement authorities. I hereby agree that the thesis may need to be reviewed with an electronic data processing for plagiarism. This work has not yet been submitted as a doctoral thesis in the same or a similar form in Germany or in any other country. It has not yet been published as a whole.

Omid Kazemi

Magdeburg, den 8. Februar 2021

Abstract

During the past decades, the Mo-Si-B alloys have received significant scientific attention since they combine excellent creep behavior and acceptable oxidation resistance at high temperatures. Due to these properties, this class of refractory materials has been considered as potential candidates for high temperature applications such as aerospace engines and the power-generating industries. However, among the scientific research sufficient attention has not been paid to investigate this alloy system numerically. The present Ph.D. thesis deals with the development of phase-field based model to study the solidification behavior of Mo-rich Mo-Si-B alloy compositions including the ternary eutectic composition and near eutectic compositions which tend to form a primary phase during the solidification. In order to develop the model, thermodynamic data published within the literature and thermodynamic database have been considered within the model. The ternary alloy compositions investigated within the model were taken from the so called “ Berczik triangle ” region of the Mo-Si-B system which consist of the molybdenum solid solution phase (Mo_{SS}) and the two intermetallic phases Mo_3Si and Mo_5SiB_2 . The solidification behavior of the considered alloy compositions was investigated by exploring the microstructure and the sequence of the phase transition reactions during the solidification. The solidification path has been carefully investigated by monitoring the chemical composition of the melt through the temperature reduction. The outcome of the model has been verified with published experimental data within the literature and an acceptable accordance between the simulation results and experimental observations has been noticed. As an outcome of the present work, a phase-field based model has been developed which is capable of simulating the solidification behavior of Mo-rich Mo-Si-B alloy compositions therefore enables the materials designers to investigate the microstructure and phase structure of the Mo-rich Mo-Si-B alloys.

Deutsche Kurzfassung

In den letzten Jahrzehnten haben die Mo-Si-B-Legierungen erhebliche wissenschaftliche Aufmerksamkeit erhalten, da sie ein ausgezeichnetes Kriechverhalten und eine akzeptable Oxidation kombinieren Widerstand bei hohen Temperaturen. Aufgrund dieser Eigenschaften wurde diese Klasse feuerfester Materialien als potenziell angesehen Kandidaten für Hochtemperaturanwendungen wie Luft- und Raumfahrtmotoren und die Stromerzeugungsindustrie. In der wissenschaftlichen Forschung wurde jedoch nicht genügend Aufmerksamkeit geschenkt, um dieses Legierungssystem numerisch zu untersuchen. Der vorliegende Ph.D. Die Arbeit befasst sich mit der Entwicklung eines phasenfeldbasierten Modells zur Untersuchung des Erstarrungsverhaltens von Mo-reichen Mo-Si-B-Legierungszusammensetzungen, einschließlich der ternären eutektischen Zusammensetzung und nahezu eutektischen Zusammensetzungen, die dazu neigen, während der Verfestigung eine Primärphase zu bilden. Um das Modell zu entwickeln, wurden thermodynamische Daten, die in der Literatur und in der thermodynamischen Datenbank veröffentlicht wurden, im Modell berücksichtigt. Die im Modell untersuchten ternären Legierungszusammensetzungen wurden aus der sogenannten "Berczik-Dreieck"-Region des Mo-Si-B-Systems entnommen die aus der festen Molybdänlösungsphase (Mo_{SS}) und den beiden intermetallischen Phasen Mo_3Si bestehen und Mo_5SiB_2 . Das Erstarrungsverhalten der betrachteten Legierungszusammensetzungen wurde untersucht, indem die Mikrostruktur und die Abfolge der Phasenübergangsreaktionen während der Verfestigung untersucht wurden. Der Erstarrungsweg wurde sorgfältig untersucht, indem die chemische Zusammensetzung der Schmelze durch Temperatursenkung überwacht wurde. Das Ergebnis des Modells wurde mit veröffentlichten experimentellen Daten in der Literatur verifiziert und eine akzeptable Übereinstimmung zwischen den Simulationsergebnissen und experimentellen Beobachtungen festgestellt. Als Ergebnis der vorliegenden Arbeit wurde ein phasenfeldbasiertes Modell entwickelt, das das Erstarrungsverhalten von Mo-reichen Mo-Si-B-Legierungszusammensetzungen simulieren kann und es den Materialdesignern daher ermöglicht, die Mikrostruktur und Phasenstruktur des zu untersuchen Mo-reiche Mo-Si-B-Legierungen.

Contents

Abstract	V
Deutsche Kurzfassung	VII
1 Introduction	1
2 Mo-Si-B alloys for high temperature applications	5
2.1 Mo ₅ SiB ₂ (T2)	7
2.2 Mo ₅ SiB ₂ (T2)	11
2.3 Mo ₃ Si (A15)	12
2.4 Phase diagram of Mo-Si-B system	14
2.5 Numerical studies on Mo-Si-B system	16
3 Description of the phase-field method	19
4 Aim and outline of the present thesis	27
5 Simulation procedure	29
5.1 Diffusion parameters	31
5.2 Temperature trend	32
5.2.1 Temperature trend for eutectic composition solidification	32
5.2.2 Temperature trend for near eutectic composition solidification	33
5.2.3 Initial temperature	33
5.3 Phase diagram input data	34
5.3.1 Phase diagram input data for eutectic composition solidification	34
5.3.2 Phase diagram input data for near eutectic compositions	35
5.4 Simulation domain	37
5.5 Phase interaction data	38
5.6 Emerging solid nuclei	38
5.7 Morphology study of directional ternary eutectic solidification	39
6 Results and discussion	43
6.1 Ternary eutectic solidification	44
6.1.1 3D simulation of eutectic solidification	46
6.1.2 Component distribution pattern	47
6.1.3 Effects of solidification conditions on lamellae growth structure	47

6.2	Near eutectic compositions	50
6.2.1	Selecting the referral compositions	53
6.3	Solidification reactions of considered compositions	53
6.3.1	Alloys with Mo_{55}Si primary phase	53
6.3.1.1	Mo-15.0Si-8.0B (Alloy 1)	54
6.3.1.2	Mo-16.4 Si-6.7 B (Alloy 2)	56
6.3.2	Alloys with Mo_5SiB_2 primary phase	60
6.3.2.1	Mo-15.0Si-10.0B (Alloy 3)	60
6.3.2.2	Mo-18.0Si-8.0B (Alloy 4)	62
6.3.3	Alloys with Mo_3Si primary phase	65
6.3.3.1	Mo-20.4 Si-5.0 B (Alloy 5)	66
6.3.3.2	Mo-20.2 Si-5.8 B (Alloy 6)	69
6.4	Microstructure evolution of considered compositions	72
6.4.1	Alloys with Mo_{55}Si primary phase	72
6.4.2	Alloys with Mo_5SiB_2 primary phase	73
6.4.3	Alloys with Mo_3Si primary phase	74
6.5	Discussion	76
7	Summary and Conclusion	79
A	Initial temperature of the simulations	83
B	Additional simulation results	84
	Bibliography	87

List of Figures

1.1	A scheme of a GP7200 engine including its main sections; fan, LPC: low-pressure compressor, HPC: high-pressure compressor, CC: combustion chamber, LPT: low-pressure turbine and HPT: high-pressure turbine [1].	1
1.2	An overview of maximum working temperature of the gas turbines and development of turbine materials adapted for rising operating temperatures, the straight line indicates the application limit of Ni-based superalloys [5].	2
2.1	Isothermal section of the ternary Mo-Si-B system at 1600 °C [54, 55]. The Mo-rich compositions highlighting both important triangles investigated by Berczik et al. [50, 51], and Akinc et al. [41–46],.	7
2.2	Body centered cubic structure of Mo [56].	8
2.3	Binary phase diagram of Mo-Si [58].	8
2.4	Yield strength of Mo ₅₅ S versus temperatures in presence of different Si content (wt.%) and grain size [39].	9
2.5	Room temperature fracture toughness of Mo ₅₅ S as a function of the Si concentration (wt.%) [39].	10
2.6	Crystal structure of Mo ₅ SiB ₂ (T2) [56].	11
2.7	Stress-strain curves of Mo ₅ SiB ₂ single crystals at 1500° [63].	12
2.8	Crystal structure of Mo ₃ Si (A15) phase [56].	13
2.9	Comparison of the Mo-Si-B liquidus projection predicted by Yang and Chang [78, 79] (shown in blue) with the experimental results obtained by Hasemann et al. [81] (shown in red).	16
3.1	Diffusive interface versus sharp interface, a) variables grow continuously in diffusive interface model, b) variables are discontinues at the interface [32].	19
5.1	The work flow followed in present research for performing the phase-filed simulation of microstructure evolution.	30
5.2	Phase diagram linerisation process; two different isotherm cross sections are selected from Mo-Si-B ternary phase diagram and the composition of two corresponding points are derived; one at each temperature. The compositions along with the slope of connecting points are defined to the simulations.	35

5.3	Liquidus surface of Mo-Si-B, data based on reference [111].	36
6.1	Microstructure and Lamellae growth pattern observed in the directional solidification simulations of ternary eutectic Mo-Si-B alloy composition.	46
6.2	3D simulation of ternary eutectic composition Mo-Si-B alloy solidification (left picture) and a perpendicular cross section of lamellae growth direction along with the experimental observations (right picture). On the left picture the data for the vertical and horizontal cross sections are projected onto a parallel virtual plane for better visualization. . . .	47
6.3	Concentration distribution of component. The value of each element along with the illustrated line is revealed.	48
6.4	Different lamellar growth pattern predicted by the developed model at considered growth velocity for the various lamellae spacing: a)1 b)2 c)6 d)12 μm	49
6.5	A comparison between the prediction of phase-field simulations of ternary eutectic Mo-Si-B alloy composition and analytical expression of Choudhury et al. [114].	50
6.6	Alkemade line between the stoichiometric Mo_3Si (blue point) and Mo_5SiB_2 (red point) in the respective published liquidus projections, a) Yang and Chang [78, 79] b) Hasemann et al. [81].	52
6.7	Examined alloys with Mo_{SS} primary solidifying phase considering the corresponding liquidus surface [78, 79].	54
6.8	Sequence of solidification reactions and volume fraction of different solid phases generating during solidification of Mo-15.0Si-8.0B	55
6.9	Solidification path of the Mo-15.0Si-8.0B alloy.	56
6.10	Formation sequence and volume fraction of different solid phases during solidification of Mo-16.4Si-6.7B.	57
6.11	solidification path of the alloy Mo-16.4 Si-6.7 B. The composition of the melt was monitored during the solidification and has shown to be changing by formation of the solid phases.	58
6.12	Chemical composition of different solid phases formed during solidification of Mo-15.0Si-8.0B. The value of each component along with the illustrated line is presented.	59
6.13	Component distribution pattern within the phases formed during solidification of Mo-16.4Si-6.7B alloy and the value of each component along with the illustrated line.	59
6.14	sequence of different solidification reactions and the corresponding temperatures during solidification of Mo-15.0Si-10.0B alloy composition. . .	61
6.15	Schematic of the solidification path of Mo-15.0Si-10.0B alloy composition achieved through the simulations.	62

6.16	Portion of the volume of different rising solid phases within solidification process of Alloys with Mo-18Si-8B composition	63
6.17	solidification path of the alloy Mo-18 Si-8 B. At the beginning of solidification the composition of the melt contains 18 at.% Si and 8.0 at.% B. However, by proceeding of the solidification the chemical composition of the melt changes and moves toward Mo ₅ SiB ₂ -Mo ₃ Si eutectic valley. The solidification proceed until the composition od the melt reaches the ternary eutectic composition.	64
6.18	Distribution pattern of different elements among the solid phases within Mo-15.0Si-10.0B alloy and along with the illustrated line.	65
6.19	Pattern of distribution of the elements among the phases within solidified Mo-18 Si-8 B alloy, the amount of every component is demonstrated along with the illustrated line.	66
6.20	Considered alloy compositions within the Mo ₃ Si primary solidification area	67
6.21	Formation sequence of different solid phases during the solidification simulation of Mo-20.4Si-5.0B (at.%) alloy.	67
6.22	Solidification path of the Mo-20.4Si-5.0B (at.%) composition based on the outcome of the simulations.	68
6.23	Solidification process of Mo-20.2Si-5.8B (at.%) based on the outcome of the simulations.	69
6.24	Solidification path of Mo-20.2Si-5.8B. By nucleation and growth of solid primary Mo ₃ Si phase, composition of the melt moves toward binary Mo ₅ SiB ₂ - Mo ₃ Si eutectic valley. As the solidification proceeds, the composition goes toward ternary eutectic point. The process end by turning the residual melt into ternary eutectic composition.	70
6.25	Distribution of the constituents within solid phases of alloy Mo-20.4Si-5.0B and along with the illustrated line.	71
6.26	Distribution pattern of components inside the solid phases within alloy Mo-20.2Si-5.8B as well as along with the illustrated line.	72
6.27	Microstructure of the Mo-15.0Si-8.0B (at.%) composition a) achieved by simulations b) observed in the experiments of Hasemann et al. [81] and Mo-16.4Si-6.7B (at.%) composition c) based on the simulations d) experiments of Hasemann et al. [81].	73
6.28	Microstructure of the Mo-15.0Si-10.0B (at.%) composition a) achieved by simulations b) observed in the experiments of Hasemann et al. [81] and Mo-18.0Si-8.0B (at.%) composition c) based on the simulations d) experiments of Hasemann et al. [81].	74
6.29	Microstructure of the Mo-20.4Si-5.0B (at.%) composition a) achieved by simulations b) observed in the experiments of Hasemann et al. [81].	75

6.30	A phase diagram with tie lines for small solidification region (LS) and a bigger solidification region (L'S) for a binary system.	76
B.1	Microstructure evolution and solidification reaction of Mo-18.3Si-4.7B (at.%) alloy composition.	84
B.2	Microstructure evolution and solidification reaction of Mo-16.9Si-7.4B (at.%) alloy composition.	84
B.3	Microstructure evolution and solidification reaction of Mo-21.3Si-4.7B (at.%) alloy composition.	85

List of Tables

5.1	Diffusion information for the considered species within the different phases	32
5.2	Phase diagram input data for ternary eutectic solidification simulations derived from [111].	35
5.3	Phase diagram input data for solidification simulations of near eutectic alloy compositions for the temperature between 2340 (K) and 2268 (K) based on the information of [111].	36
5.4	Phase diagram input data for solidification simulations of near eutectic alloy compositions for the temperature between 2268 (K) and below [111].	37
5.5	Data for phase interaction between different phases	38
5.6	considered criteria for predicting the nucleation behaviour of different solid phases. The maximum temperature of nucleation of the solidi phases was derived from thermodynamic database [78, 79].	39
6.1	Different considered lamellae spacing in simulation of ternary eutectic Mo-Si-B alloy solidification and corresponding undercooling at solidification front.	48
6.2	considered alloys within the simulations in the framework of the present thesis including their primary solidifying phase [78, 79]. The concentration of the components indicated within table are at. %.	53
6.3	composition of alloys solidifying with the Mo_5SiB_2 primary phase. . . .	60
A.1	considered alloys and their corresponding initial temperature within the simulation domain (K) according to the thermodynamic data [78, 79]. .	83

1 Introduction

Obtaining new functionality and expanded utility in materials has become increasingly important for next generation materials and emerging innovations in so many areas such as stationary gas turbines and aircraft engines. Increasing the efficiency of the aircraft engines, specially for the sake of preserving resources and reducing environmental impacts, has been target of various studies. In the figure 1, an aircraft engine particularly GP7200 engine [1] is represented as an example. As it is shown, the engine can be separated into four principal parts: the fan, the compressor which is subdivided into the low-pressure compressor (LPC) and high-pressure compressor (HPC), the combustion chamber and the turbine which is also subdivided into low-pressure turbine (LPT) and high-pressure turbine (HPT). For each part different materials are considered depending the working situations and particular loads of the individual engine parts. The present work specifically deals with the high-pressure turbine where any increase in working temperature would result in an increase in working efficiency.

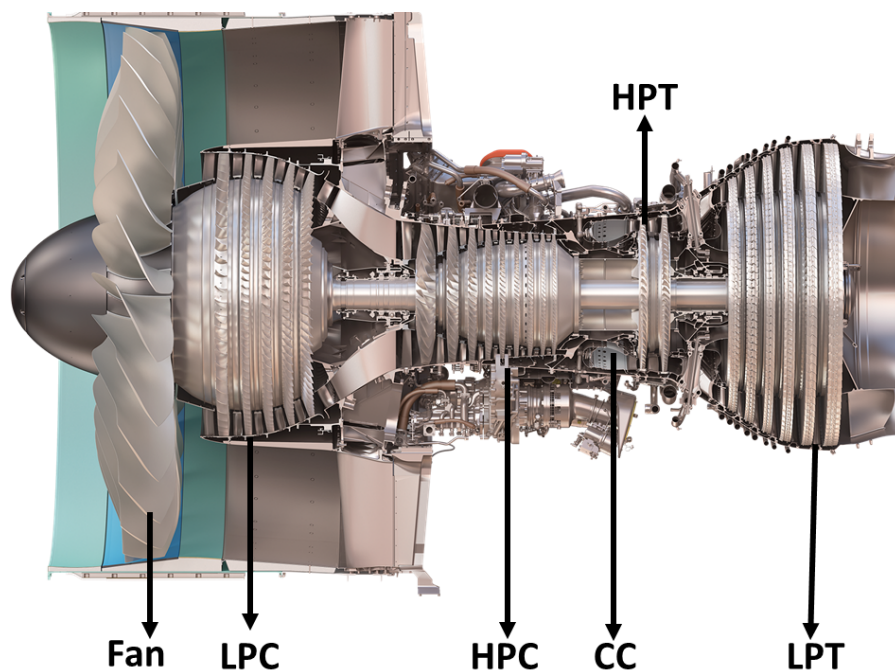


Figure 1.1: A scheme of a GP7200 engine including its main sections; fan, LPC: low-pressure compressor, HPC: high-pressure compressor, CC: combustion chamber, LPT: low-pressure turbine and HPT: high-pressure turbine [1].

The impact of operating temperature of the engine on the efficiency can be expressed based on thermodynamics. As the “Joule cycle” says; the thermodynamic efficiency of a turbine can be calculated by equation 1.1. Which means, increasing the temperature of operating engine will result in an efficiency increase which consequently reduces the fuel consumption.

$$\eta_{therm} = 1 - \frac{T_{min}}{T_{max}} \quad (1.1)$$

According to equation 1.1, in order to maximize the efficiency of the aircraft engine, the temperature in the combustion chamber (T_{max}) and consequently the gas inlet temperature should be increased. In this regard, a specific attention should be paid to the high-pressure turbine blades, since they are the most critical components, due to high thermal loading and stresses caused by temperature hot-spots and gradients between the airfoil and root. For a comprehensive description of the aim and efforts of research on structural materials for turbine engines, the reader is referred to reference [2].

For more than 60 years, Ni-based superalloys have been improved continuously and applied in mentioned high temperature industries [3, 4]. Ni-based superalloys are currently used as single-crystals in aircraft engines representing the state-of-the-art turbine blade material. Figure 1.3 shows an overview of the evolution of maximum operating temperatures in gas turbines and applied turbine materials adapted to the working temperature.

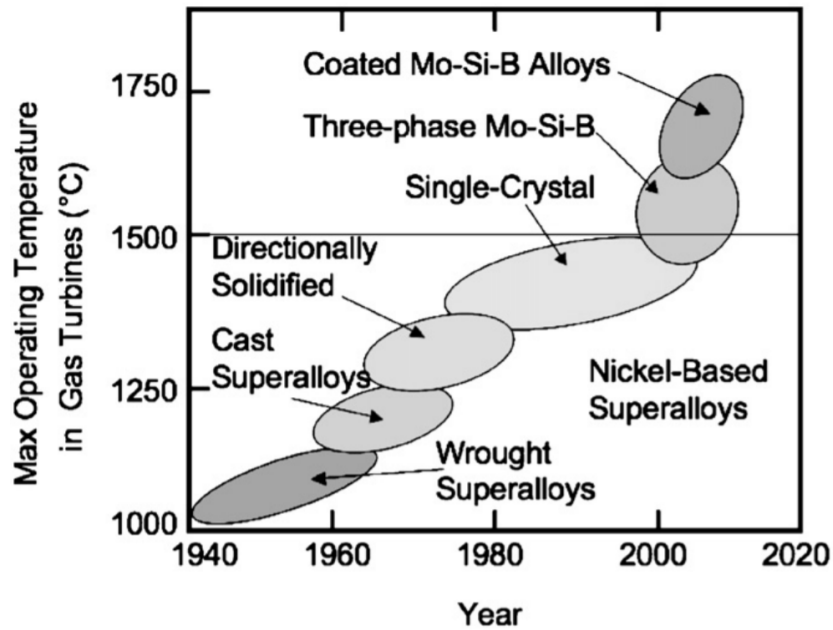


Figure 1.2: An overview of maximum working temperature of the gas turbines and development of turbine materials adapted for rising operating temperatures, the straight line indicates the application limit of Ni-based superalloys [5].

As it is shown in the figure 1.3, the currently applied high temperature materials in high temperature industries such as gas turbines and spacecraft engines are running pretty close to their maximum operating temperature [2] therefore, although the advanced cooling systems and coating are considered, the turbine's efficiency cannot be substantially increased any more [5]. Consequently, in order to increase the operating temperatures of gas turbine engines and their efficiency as a result, advanced alloys are required that are capable of tolerating the higher working temperature along with corrosive operating environment [2, 6].

The demand for new high-performance alternative materials with higher melting temperature has resulted in applying refractory metal alloys. In which the considered alloys are often alloyed with Si and/or B. Utilizing of Si and B in these Me-Si-B (Me = metal) alloys is because of forming strengthening silicides and borides which improve the creep performance and oxidation resistance of the alloy. In this regard, different multiphase systems such as Mo-Si-B [2, 7, 8], Nb-Si(-B) [9, 10], and V-Si-B [11, 12] have been investigated and proved the ability of being promising candidates for future high temperature applications. According to Fleischer [13], high melting temperature would result in high modulus of elasticity and thus leads to the improved dimensional stability of components under tough working conditions such as complex thermal loading. Moreover, the higher melting temperature results in lower coefficient of thermal expansion. Thereupon refractory materials show a desirable behavior under thermocyclic loading [14]. Thus, because of the high melting temperature of Mo, which is around 2600 °C [15], the Mo-based alloys provide the highest melting point among the ternary systems which are investigated so far and therefore provide the highest potential for being applied in high temperature applications. Based on high melting point and because of showing excellent creep behavior and acceptable oxidation resistance at high temperatures, multi-phase Mo-based alloys have absorbed particular attention to be considered as potential alternative materials in aerospace engines and power generating industries [16–19]. It should be considered that the processing techniques for preparing the Mo-Si-B alloys can be categorized into four main groups: the ingot metallurgy, the directional solidification, the powder metallurgy, and a the additive manufacturing. Therefore, the solidification process plays an important role in preparing the Mo-Si-B alloys. Hence, the major aim of present work is to investigate the solidification behavior of Mo-rich Mo-Si-B alloys.

A promising microstructure investigations can be achieved in the Integrated Computational Materials Engineering (ICME) approach. ICME approach attempts to reduce the time and cost of design and development of new materials through the use of computational material models. ICME seeks for devising material models that quantitatively describe the relationship of a materials processing, structure, and properties in two different divisions; firstly correlating the materials processing to the material

structure, which is the aim of the present research and then correlating the structure of materials to their properties [20, 21].

Providing the ability to model a wide variety of materials processes and microstructure evolution, the phase-field approach has received significant attention since the early 1990s [22]. Phase-field modeling is nowadays considered as a significant subset of computational materials science. By applying the thermodynamic data to study the kinetics of microstructure evolution, phase-field has been used successfully to study phase transitions, order-disorder transitions, nucleation and spinodal decomposition, grain growth, coarsening, the growth of dendrites in a super-cooled liquid, directional solidification, faceted crystal growth, diffusion controlled processes, solute drag, and the effects of anisotropy [21, 23, 24]. A considerable amount of researches have focused on the application of phase-field models to these areas. For more information, the reader is referred to articles published by author of present thesis [25–28] as well as the review articles that could provide a wide vision to the topic [29–34].

2 Mo-Si-B alloys for high temperature applications

In order to look for new materials for applying in high temperature applications such as spacecraft engines, the functionality and thermal stability of the constituent phases in the considered material should be taken into account from several aspects. The most important feature is durability and serviceability of the phases in high temperatures, which obviously require an inherently high melting temperature. In addition, due to the thermal cycling and the effect of creep under varying stress states, it is crucial to modify the microstructure. Considering the application of the alloy, the microstructure should be modified to produce a practical alloy. Moreover, the possible reactions between the phases at bulk or interfaces between phases and the evolution of microstructure during phase transformations should be considered whereby the thermodynamic and kinetic data of every considered alloy system are required. With this approach a comprehensive study of advanced materials should be pursued which is essential for successful development of new functional materials[35].

Regarding the considered criteria, multi-phase Mo-based alloys have been the particular interest of several researches and have been studied as potential materials for high temperature industries such as aerospace engines. Among different Mo-based alloys, Mo silicides have absorbed significant amount of attention since they show excellent creep behavior combined with acceptable oxidation resistance at high temperatures applications [16–19]. Moreover, Mo-borides have shown desired properties for high temperature applications such as; high melting points, elevated thermal and chemical stability and high hardness along with mechanical stiffness [36–38]. Despite showing favorable properties, the referred binary compositions are not suitable to be applied alone in the high temperature applications because adding just Si or B component to the Mo crystal, would increase the brittleness of the material. This effect is more obvious in the Mo-Si system [39, 40]. Therefore, considering the ultimate goal of designing a material which exhibits both creep and oxidation resistance at high temperatures as well as an adequate crack tolerance at room temperature and deformation potential, a solution should be devised to preserve the considered features in an optimal way. In this regard, the major focus of following chapters is multiphase Mo-Si-B systems.

As it is shown in the figure 2.1, there are two main regions in the Mo-Si-B phase diagram. The first region was characterized by Akinc et al. [41–46], which is high-

lighted in green, contains binary intermetallic phases Mo_3Si and Mo_5Si_3 (T1) as well as the ternary intermetallic phase Mo_5SiB_2 (T2). It is worth to mention that the alloys located in Akinc region show excellent oxidation resistance. Their oxidation resistance feature is because of forming a continuous and protective $\text{SiO}_2\text{-B}_2\text{O}_3$ layer on the materials surface during the oxidation exposure [47, 48]. To obtain a protective and self-healing oxide layer a relatively high boron concentration is needed in which the Mo_5SiB_2 phase serves as reservoir for boron in these alloys. Because the boron content reduces the viscosity of the passive $\text{SiO}_2\text{-B}_2\text{O}_3$ layer, it is a crucial component for the oxidation protection. Despite showing desired oxidation resistance, these alloys are not suitable for high temperature applications because these alloys are composite of pure intermetallic phases and exhibit a very high brittle-to-ductile transition temperature (BDTT) and low fracture toughness [49]. Therefore, using the alloys from this region would not lead to an adequate fracture toughness at room temperature.

Another highlighted region in the figure 2.1 is called “Berczik triangle”, because it was investigated by Berczik et al. [50, 51]. As it is shown in the figure 2.1, the Berczik triangle is located between the Mo_{ss} phase and the intermetallic phases Mo_3Si and Mo_5SiB_2 . As it is discussed before, the Mo-Si and Mo-Si-B intermetallics phases constituted in Mo-Si-B system improve the creep resistance and oxidation behavior of the alloy in high operating temperatures [6, 18, 52], however in correlation with their very high brittle-to-ductile transition temperature (BDTT) and low fracture toughness at room temperature [6, 49] these intermetallics can arise significant challenges for applying them in to high temperature industries. So considering a modified combination of Mo_{ss} and Mo_3Si and Mo_5SiB_2 phase could be appealing [6, 18, 52]. The three-phase microstructure shows a wide stability range up to high temperatures of around 1800 °C [53]. In contrast to the Akinc alloys, the Berczik alloy compositions benefit presence of the ductile Mo_{ss} phase which is able to improve the room temperature and high temperature fracture toughness. However, the volume fraction of Mo_{ss} within the alloy should be considered in regard with the application. Concluding the discussed considerations, the Berczik triangle phase field is major focus of the present study. The properties of corresponding phases are discussed in the following.

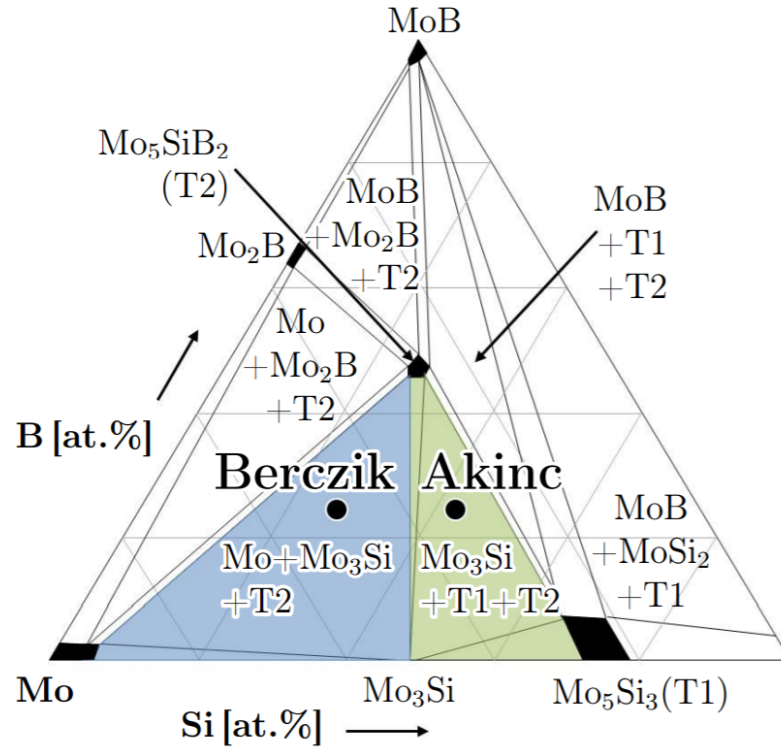


Figure 2.1: Isothermal section of the ternary Mo-Si-B system at 1600 °C [54, 55]. The Mo-rich compositions highlighting both important triangles investigated by Berczik et al. [50, 51], and Akinc et al. [41–46],.

2.1 MoSS

The Mo_{SS}, which is referred as α -Mo in some literature, is a solid solution of Si content inside Mo crystal. The Mo has a body centered cubic crystal structure. Figure 2.2 shows the crystal structure of Mo [56].

It is worth to mention that the solubility of B inside Mo is negligible [57] but the solubility of Si inside Mo depends on the temperature [40]. For example it reaches to 2 at.% at 1400 °C and around 4 at.% (1.2 wt. %) at 2025 °C. The Mo_{SS} is shown in the far left part of Mo-Si phase diagram in figure 2.3 [58]. The desired properties of Mo, which made it a favorable refractory metal for the high temperature industries are: high melting temperature, low thermal expansion and high thermal conductivity [56]. In reverse, the Mo shows some unsatisfactory behavior in high temperatures. For example, it oxidizes readily above 600°C and has poor creep resistance at high temperatures. However, presence of Mo_{SS} in ternary Mo-Si-B alloys can improve the ductility and fracture toughness alloy. [6, 18, 39, 59].

Sturm et al. [39] have reported that the strength of the Mo_{SS} is dependent on the amount of Si content. As it is shown in the figure 2.4, small amount of Si increases the yield strength of Mo_{SS} comparing to Mo obviously, and adding 1 wt.% Si to Mo, can

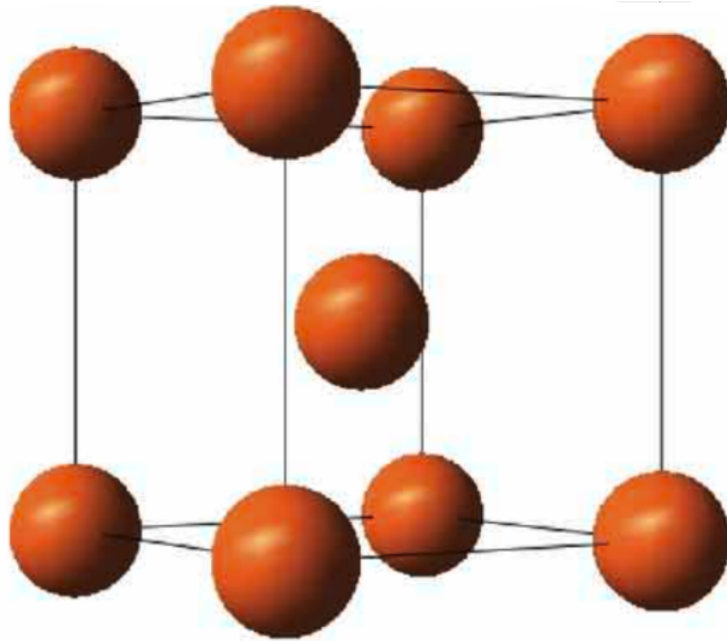


Figure 2.2: Body centered cubic structure of Mo [56].

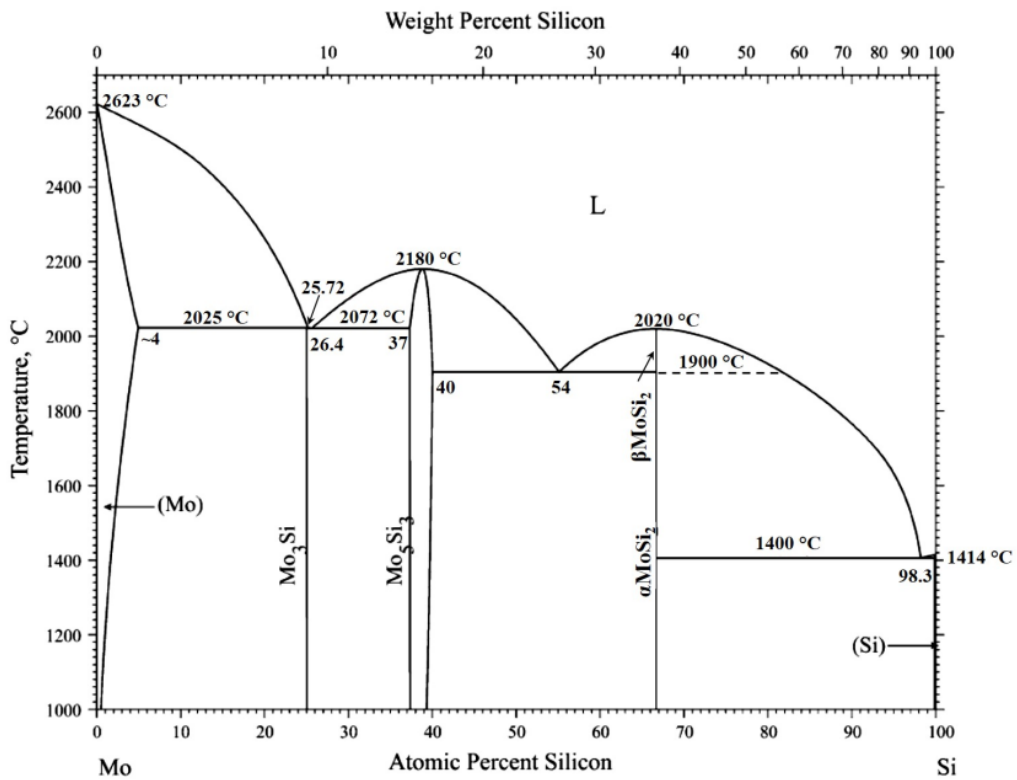


Figure 2.3: Binary phase diagram of Mo-Si [58].

increase the yield strength approximately six times more than Mo. Another effect of adding Si to Mo is decreasing the fracture toughness and ductility [39]. As it is shown in the figure 2.5, the fracture toughness of polycrystalline MoSS reduces with the Si concentration. Sturm et al have reported the fracture mechanism of polycrystalline Mo without Si as solid solution is different with MoSS. Fracture in Mo without Si happens trangranularly at room temperature, while it happens in polycrystalline MoSS predominantly intergranularly. This difference in fracture mechanism could be due to grain boundary embrittlement by Si segregation at grain boundaries. Hence, the fracture toughness decreases with increasing Si content [39].

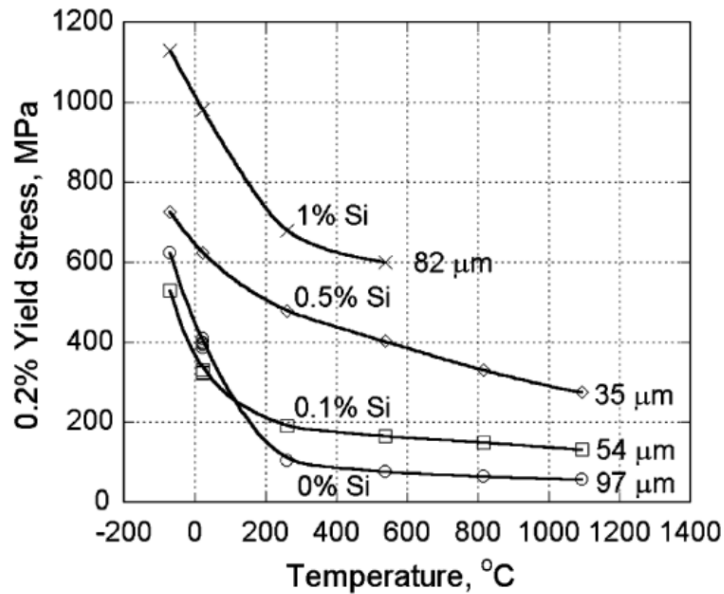


Figure 2.4: Yield strength of MoSS versus temperatures in presence of different Si content (wt.%) and grain size [39].

Despite showing favorable features, molybdenum is vulnerable to embrittlement because of nitrogen or oxygen segregation at the grain boundaries. A potential solution for this problem could be reducing the grain size of molybdenum-based alloys, and consequently a reduction in the concentration of these components on the grain boundaries. Another solution could be microalloying with an appropriate component that could suppress oxygen and nitrogen segregation at the grain boundaries. For example, Mousa et al. [60] have shown that alloying small amounts of zirconium to a solid solution of Mo-1.5Si alloy improves the formation of phases containing molybdenum, silicon and oxygen, and therefore lowers the amount of oxygen at the grain boundaries.

Considering all discussed features, for developing new material with high Mo constituent Mo-Si-B composition, presence of MoSS phase results in an improved fracture

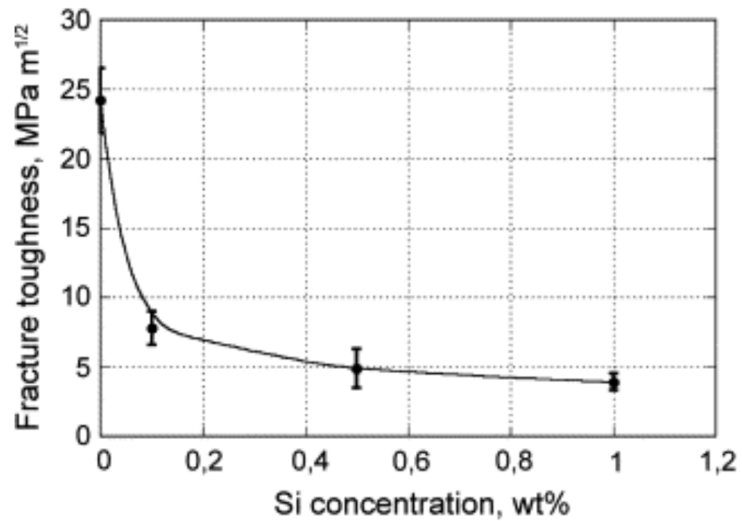


Figure 2.5: Room temperature fracture toughness of Mo_{SS} as a function of the Si concentration (wt.%) [39].

toughness [61]. In order to decrease the BDTT of multiphase Mo-Si-B alloy, a high volume fraction of continuously formed Mo_{SS} phase would be helpful.

2.2 Mo_5SiB_2 (T2)

The intermetallic Mo_5SiB_2 phase develops through a peritectic reaction during solidification. Due to the mechanical properties and oxidation resistance, the Mo_5SiB_2 phase is a very important component in Mo-Si-B alloys. The Mo_5SiB_2 represents the only ternary phase in the Mo-Si-B system and exhibits a range of solubility of components. According to Perepezko et al. [57], the Mo_5SiB_2 phase has a solubility range of 9 at.% to 13.8 at.% of Si and 24 at.% - 27.5 at.% B. Moreover, by decreasing the temperatures the Si and B concentration increases while the Mo concentration decreases [53, 55].

The Mo_5SiB_2 is a strong but brittle phase. First time, Aronsson has determined the body-centered tetragonal crystal structure of Mo_5SiB_2 and related it to the T2 structures of Nb_5Si_3 and Ta_5Si_3 [62]. Figure 2.6 shows the crystal structure of Mo_5SiB_2 . Ito et al. have measured the elastic constants of Mo_5SiB_2 from room temperature up to 1100°C [63].

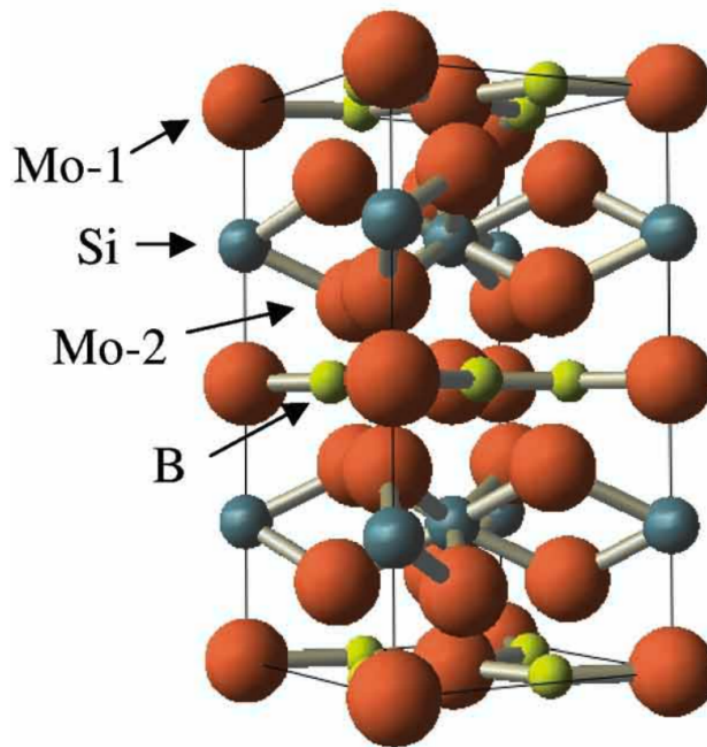


Figure 2.6: Crystal structure of Mo_5SiB_2 (T2) [56].

The high melting temperature of Mo_5SiB_2 (more than 2500 K) along with its relatively low density ($8.864 \frac{\text{g}}{\text{cm}^3}$) [47] made it a high potential candidate to be applied in high temperature industries. Due to its crystal structure, a distinct feature of Mo_5SiB_2

phase is extreme creep resistance, even at high temperatures [63]. It should be considered that the Mo_5SiB_2 phase is brittle and as it is shown in figure 2.7, it does not demonstrate plasticity until temperatures of about 1500°C . The Mo_5SiB_2 is extremely hard and the strength of this phase leads in extreme creep resistance. Ihara et al. have reported that single crystal of Mo_5SiB_2 shows some deformability along with extremely high strength at 1500°C for certain orientations [63, 64].

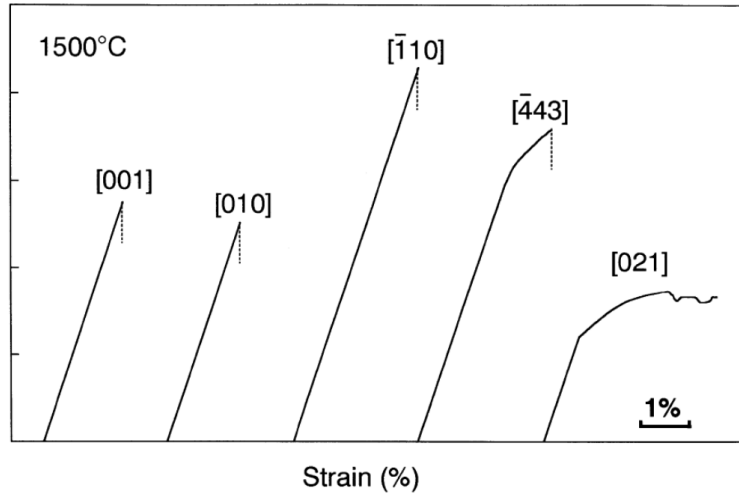


Figure 2.7: Stress-strain curves of Mo_5SiB_2 single crystals at 1500° [63].

Besides high temperature strength, Mo_5SiB_2 provides good oxidation resistance. The oxidation resistance of Mo_5SiB_2 phase is provided by forming a borosilicate layer in the early stages of oxidation. When the Mo_5SiB_2 is applied together with Mo_3Si , the borosilicate scale at the early stage of oxidation exposure, diffuses into the SiO_2 scale formed by Mo_3Si , which lowers the viscosity of the SiO_2 scale and leads to passivation of the scale [6, 18, 47, 48].

2.3 Mo_3Si (A15)

The intermetallic Mo_3Si phase is a cubic phase with A15 structure. The crystal structure is shown in Figure 2.8 [56]. Comparatively, little research has been devoted to the mechanical properties of Mo_3Si [65], however Swadener et al. have investigated the room temperature properties of single crystal Mo_3Si specimens [66] and Xu et al. have investigated the mechanical parameters from first-principles calculations to explore the plasticity of cubic A15-structured Mo_3Si [67]. The Mo_3Si is a high strength phase and therefore so brittle at room temperature [68]. Moreover, the Mo_3Si provides oxidation resistance with forming a SiO_2 scale over the oxidation surface [6, 18, 48].

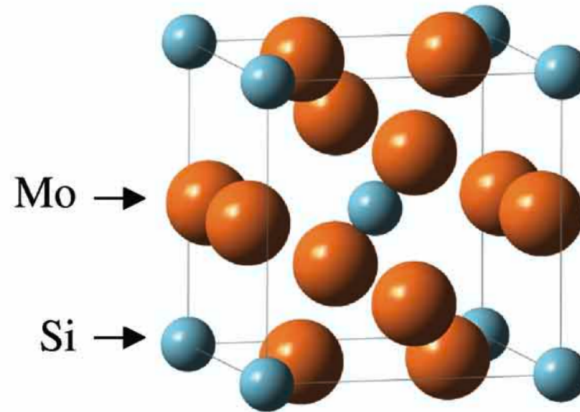


Figure 2.8: Crystal structure of Mo_3Si (A15) phase [56].

Considering formerly mentioned phases and their properties, it is worth to mention that intermetallic compounds Mo_3Si and Mo_5SiB_2 enhance the high temperature oxidation resistance and creep behavior of Mo-Si-B alloys. However, these alloys are brittle both in room temperatures and high temperatures [63, 69]. To try for improving the mechanical properties such as damage tolerance of brittle intermetallic solids, utilizing a of ductile material, usually metallic reinforcements could be effective. Since the presence of a ductile phase can dissipate the energy of crack initiation and propagation through plastic deformation and crack bridging [70–72], employing Mo_{ss} could be potentially effective attitude to toughen the intermetallics.

Mo-rich Mo-Si-B alloys can be categorized into two major groups from the point of microstructure-properties correlation; **I: alloys with a large volume fraction of continuous Mo_{ss} matrix and intermetallic particles** and **II: alloys with an intermetallic matrix and few amount of discontinuous Mo_{ss} phase**. The first type alloys provide a high fracture toughness because they benefit from the ductile Mo_{ss} matrix strengthened by second phase hardening mechanism. Whereas, the second type alloys represent good oxidation resistance behaviour and good creep resistance in case of a coarse-grained microstructure. All things considered, there should be a balance between the properties by balancing the existing phases for achieving the most proper alloy. In this regard, Krüger [73] has indicated that in order to obtain a balance between the high temperature properties such as: creep and oxidation resistance and room temperature properties such as fracture toughness, the volume fraction of Mo_{ss} phase should be around 50 %. Whereby, optimizing the microstructure through the traditional experimental methods to get to the optimized properties with regards to the considered application of the alloys is expensive and takes long times [74]. Considering this fact, the scope of the present work is to study the solidification behaviour including phase evolution and pattern formation through phase-field simulation of Mo-rich Mo-Si-B alloys located within the “Berczik triangle” [50, 51].

2.4 Phase diagram of Mo-Si-B system

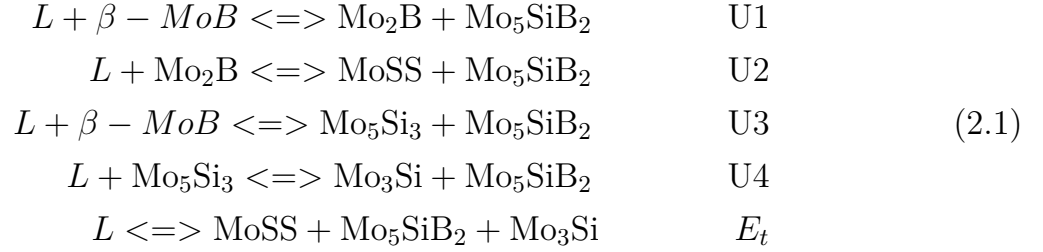
Phase diagram contains crucial information about the equilibrium constitutions, which a material system of a certain composition takes within various temperature and pressure and therefore are essential tools for the study and design of materials. Definition of phase diagram is a critical part of simulating the solidification process because the solidification process involves wide range of temperature the transformation of material takes place in correlation with the different equilibrium conditions during the temperature reduction. The transformations occurred during a certain solidification and the corresponding microstructure of the system can be understood with the help of phase diagrams. With assistance of the phase diagrams, the single-phase regions and the regions which contain multiple coexisting phases at equilibrium can be realized. Besides, the fraction of considered phases can be determined by the application of the lever rule. The other important information which are inferred from phase diagrams are the invariant reactions which take place at certain temperatures and compositions such as eutectic solidification.

The first investigation on the Mo-Si-B system, particularly the first isothermal section of the ternary phase diagram at 1600 °C was performed by Nowotny et al. [54]. Their proposed isothermal section got later on improved by Perepezko et al. [55, 75]. Ha et al. [53] have proposed an isothermal section at 1800 °C of Mo-Si-B system.

Beside the binary phase diagrams and isothermal sections in ternary systems, liquidus projections are very critical for exploring the phase diagram and studying the phase equilibria at certain compositions and/or temperatures. Besides, they are crucial to investigate the cooling behavior and solidification paths of the alloys. Having a deep sight of the solidification path and reaction sequences during solidification, further helps to understand solidification processes.

The first examination on liquidus projection of Mo-rich portion of Mo-Si-B diagram was performed by Nunes et al. [76]. Consequently the Mo-Si-B ternary phase diagram got refined further. Nunes et al. [76] have determined six primary solidification regions in Mo-rich portion of Mo-Si-B system based on microstructure evolution and solidification behavior of arc melted alloys. The primary solidification regions are; Mo_{ss} , Mo_2B , MoB , Mo_3Si , Mo_5Si_3 and Mo_5SiB_2 . The considered primary solidification areas are separated by binary eutectic valleys which contribute to four preitectic phase transition reactions (U-type) which are referred as U, and one ternary eutectic (referred as E_t) four-phase reactions in 2.1. However they have not investigated the ternary eutectic

composition.



Katrych et al. [77] have studied the phase reactions and their sequences in Mo-Si-B system and except the reaction sequence, the confirmed most of reports of Nunes et al. [76].

The liquidus projection of Mo-rich region of Mo-Si-B alloys was studied further by Yang and Chang [78, 79]. The thermodynamic description for the Mo-Si-B system developed by Yang and Chang [78, 79] represents the phase stability, the liquidus projection and the solidification paths of considered compositions based on the thermodynamic description and comparison with the experimental observations. Based on their findings, Yang and Chang [78, 79] have confirmed the reported binary eutectic reactions between Mo_{55} and Mo_5SiB_2 and the reactions between Mo_5Si_3 and Mo_5SiB_2 as well as the ternary eutectic reaction of Mo_{55} , Mo_3Si and Mo_5SiB_2 which was explained by Nunes et al. [76].

Ha et al. [80] investigated the liquidus surface of Mo-rich alloys in Mo-Si-B system through performing experimental studies of the binary Mo_{55} - Mo_5SiB_2 and Mo_3Si - Mo_5SiB_2 eutectics and the ternary eutectic of Mo_{55} - Mo_5SiB_2 - Mo_3Si . In order to conduct their investigations, they have studied different alloys with compositions near the eutectic valleys. Using scanning electron microscopy (SEM), electron probe microanalysis (EPMA) and transmission electron microscopy (TEM) Ha et al. [80] have investigated the microstructures of the considered alloys fabricated via arc melting and their observations on the eutectic microstructures of Mo_{55} - Mo_5SiB_2 , Mo_{55} - Mo_5SiB_2 - Mo_3Si and Mo_5SiB_2 - Mo_3Si were compared to Yang and Chang's calculated liquidus surface [78, 79] and the isothermal section of the phase diagram at 1800 °C from their previous work [53]. The results obtained by Ha et al. [80] are in agreement with Yang and Chang's [78, 79] calculations and confirmed their sequence of multiphase reactions during the solidification.

Recently Hasemann et al. [81] have performed a comprehensive study on liquidus surface of Mo-rich portion of Mo-Si-B system by choosing 59 different alloy compositions near ternary eutectic point and studying the microstructure evolution and the solidification reactions of alloys. They have re-investigated the liquidus projection very

carefully by assessing the microstructure evolution for every alloy composition and evaluated their solidification path by employing the Alkemade theorem [82]. In their study, Hasemann and coworkers have paid a certain attention to the microstructure formation and chemical composition of the ternary eutectic reaction and solidification primary areas in Mo-rich region of Mo-Si-B system, in particular Mo_3Si primary solidification area. The outcome of their research have proved that the primary Mo_3Si phase region is larger in comparison with present literature data. They have also confirmed the eutectic point to contain 17 ± 1 at.% silicon, and 7.5 ± 0.5 at.% boron. Figure 2.9 compares the Mo-Si-B liquidus projection predicted among Yang and Chang's calculations [78, 79], with the outcome of the experimental investigations performed by Hasemann et al. [81]. As it is shown in this figure, the ternary eutectic point predicted by Hasemann et al. [81] is slightly different with the findings of Yang and Chang [78, 79], However, the Mo_5SiB_2 region contains a wider range of compositions.

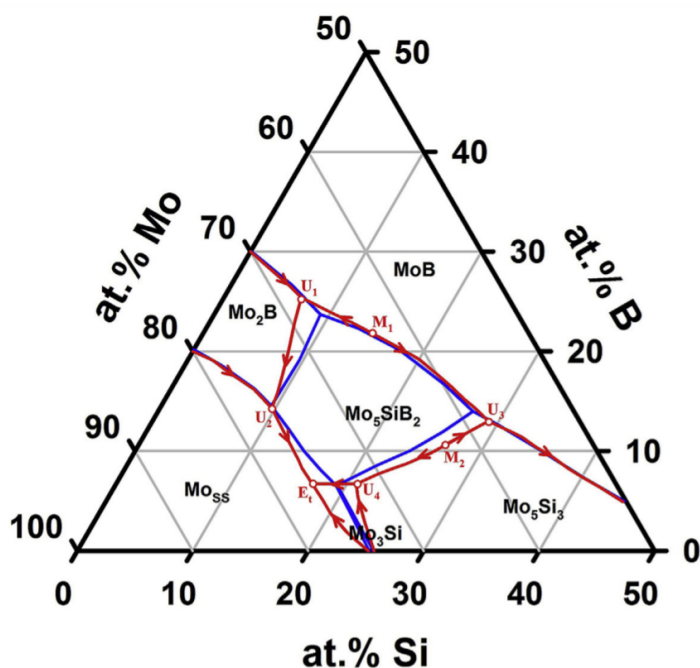


Figure 2.9: Comparison of the Mo-Si-B liquidus projection predicted by Yang and Chang [78, 79] (shown in blue) with the experimental results obtained by Hasemann et al. [81] (shown in red).

2.5 Numerical studies on Mo-Si-B system

Besides the referred experimental studies which have been discussed so far, Mo-Si-B alloy system has been investigated numerically. Biragioni et al. [83] have developed an FEM-model to investigate microstructures of Mo-Si-B alloys for predicting the elastic properties of Mo-Si-B composite materials with varying microstructures. Brindley et al. [84] have developed an interactive model to optimize the mechanical properties

for three-phase Mo-Si-B alloys. In their research, they have employed three different modeling tools to re-generate the microstructure, to capture microplasticity and to evaluate the important mechanical properties such as; the effects of microstructure on elastic modulus, yield strength, fatigue resistance, and susceptibility to brittle microcracking. In order to re-generate the microstructure, they have applied a model based on an ellipsoidal packing algorithm developed by Przybyla [85], which includes a simulated anneal algorithm for space filling. In order to capture the microplasticity, Brindley et al. [84] have considered crystal microplasticity constitutive equations implemented within finite element method and to investigate the mechanical properties, they have applied the reduced-order models [86]. Despite the discussed numerical studies, still a comprehensive simulations to study and evaluate the phase formation and microstructure evolution of Mo-Si-B alloys during the solidification has not been performed.

The microstructure formed during the solidification, has a great impact on the properties of the considered alloys. Being able to predict the microstructure resulting from solidification phenomena through arbitrary conditions enables us to have well control on the properties of the desired alloy. Therefore, **simulation of solidification**, is a very important tool in the field of computer-aided design of materials. Although significant attention has been paid to the understanding of solidification of Mo-Si-B alloys, particularly through the experimental investigations, there is not sufficient simulation studies allocated to study the solidification behavior, principally the microstructure evolution and phase transition reactions during solidification process of this system. In the case of modeling the solidification in which, the solidification front evolves freely into the liquid, the microstructure of solidification is deeply dependent on the interfacial interactions. Therefore having a reliable model which considers interfacial interactions is crucial for studying solidification behavior of the considered system. During the past decade, the phase-field approach has demonstrated to be an effective model for the simulation of solidification processes in which describes the microstructure of a complex system with aiming a set of field variables. The behavior of a provided microstructure over time is simulated by solving evolution equations written in terms of the minimization of the free energy of the entire system. The free energy of the system is written as functional of the field variables as well as their gradients and with the considered free energy functional, the governing equations (phase-field equation, diffusion equation, heat equation and so on) are solved throughout the entire space domain. In this work, a comprehensive phase-field model is presented for solidification processes considering the microstructure evolution and phase transition reactions through the solidification of the Mo-rich Mo-Si-B alloys.

3 Description of the phase-field method

The phase-field method has recently emerged as a convenient computational approach to modeling evolution of systems with complex geometries such as microstructural transformations and predicting mesoscale morphology. During the past decades, the phase-field has become a widely used model in the field of computational material science and has been applied in many fields of research, such as solidification and engineering mechanics. The principal approach of phase-field is to describe a microstructure using a set of conserved and non-conserved field variables that are continuous across the interfacial regions of considered phases. The basic concept of the phase-field model which was introduced by Ginzburg and Landau [87] and Cahn and Hilliard [88], is to use diffusive interfaces. The concept of diffuse interface was introduced by Van der Waals more than a century ago [89]. A schematic view of the diffusive interface is shown in the figure 3.1a. In contrast with diffusive interface model, in the traditional modeling of phase transformations and microstructure evolution, the interfaces between different domains used to be considered infinitely sharp (Fig. 3.1b).

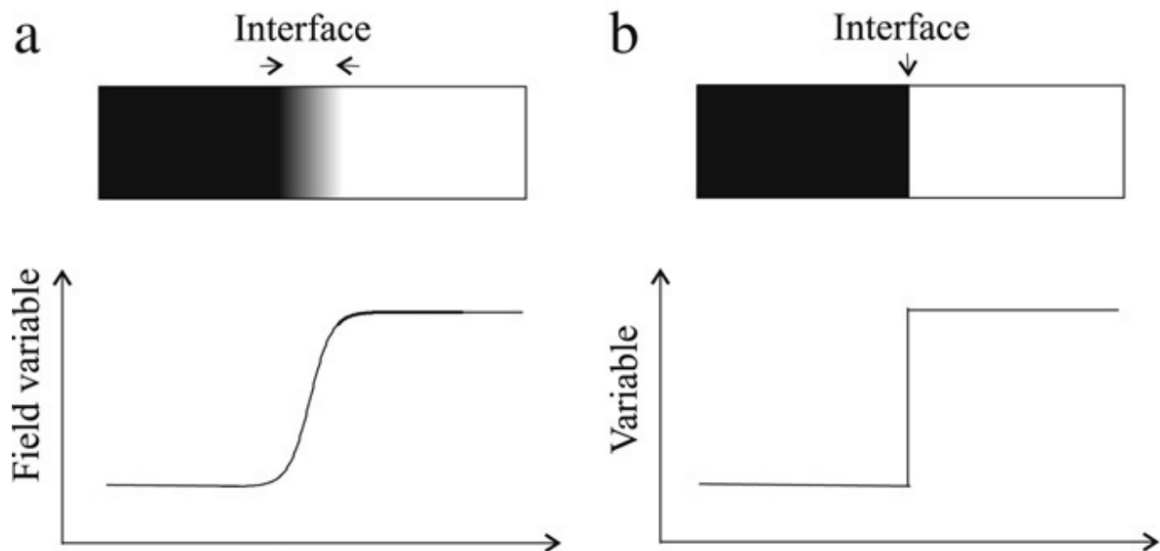


Figure 3.1: Diffusive interface versus sharp interface, a) variables grow continuously in diffusive interface model, b) variables are discontinues at the interface [32].

The concept of diffuse interface got extended later on by Ginzburg and Landau by introducing the “order parameter” through formulating a model for superconductivity using order parameter and its gradients [87]. The concept of order parameter was

later on applied by Landau for the description of phase transformations that associate a symmetry reduction [90]. In the Landau's approach, the order parameter was considered to be non-conserved and each phase is defined with an order parameter and the energy functional of a system is defined as a function of the order parameters and the temperature. The free energy minima determines the existing phase which contributes to the minima. Technically said, order parameters are considered to describe the pattern changes in the system. The differential equations describing dynamics of the order parameters are derived assuming the maximum energy dissipation of the system.

Cahn and Hilliard [88, 91–93] as well as Allen and Cahn [94] have later described the evolution equations of the order parameters as derivation of partial differential equations from the energy functionals of Ginzburg-Landau. In other words, they defined parameter evolution as the time-dependent Ginzburg-Landau energy functional. Accordingly, the evolution of the order parameters as well as the transformation from one phase to another, is driven by the energy minimization of the total system.

The evolution equations for the conserved order parameters like the composition follow the time-dependent Cahn-Hilliard equation [88, 91–93]:

$$\frac{\partial c}{\partial t} = \nabla(M(c)\nabla\frac{\partial F}{\partial c}) \quad (3.1)$$

Where $M(c)$ is the mobility of the diffusing species. The evolution of the non-conserved parameters follows the Allen-Cahn [94] equation:

$$\frac{\partial \phi}{\partial t} = -M(\phi)\frac{\partial F}{\partial \phi} \quad (3.2)$$

The phase-field model was further developed by introducing the phenomenological order parameter so called phase-field parameter (ϕ) by Langer [95]. Resembling the other considered order parameters, phase field parameter is a function of space and time. ϕ can take the values between 0 and 1, and may relate to any desired feature of intended system. For example, in the case of studying the solidification process, this order parameter may relate to the fraction of a specific phase [96].

In the case of solidification for example, the ϕ could be defined as following:

$$\phi = 1 \quad \text{for liquid and} \quad \phi = 0 \quad \text{for solid} \quad (3.3)$$

And at the interface of the liquid and solid phases, ϕ varies continuously between 0 and 1.

Considering this method of microstructure definition, the evolution of microstructure means to identify the time derivative of the $\phi(\vec{x}, t)$ which in following discussions is

shown as $\dot{\phi}(\vec{x}, t)$. In this regard and to develop the phase-field method for simulating microstructural evolution of materials and different technical processes containing multiple phases and multiple components, Wheeler et al. [97] have proposed a phase-field model for investigating the binary alloys. Their proposed model got extended by several researchers and many phase-field models have been developed based on their phase-field approach. One of the most critical improved models are implemented by Steinbach et al. [98] and Nestler et al. [99]. Steinbach et al. [98] and Nestler et al. [99] have introduced multi-phase and multi-component models to describe the complex microstructures based on a free energy functional. The free energy functional of a volume (V) of an isotropic system of nonuniform composition (c) could be expressed as following [88]:

$$F[c, \nabla c] = \int_V (f(c) + k(\nabla c)^2) dV \quad (3.4)$$

$f(c)$ refers to homogeneous free energy density and ∇c is the composition gradient of component. k is a constant called the gradient energy coefficient parameter which in general may be dependent on composition (c) and temperature, but for a simplified solution is considered to be constant.

It should be considered that in the proposed model of Steinbach et al. [98] and Nestler et al. [99], the free energy density is derived through an interpolation of the bulk free energy densities of the individual phases. The proposed models had a problem which was pointed out by Kim [100] as well. Considering the interpolation of the free energy densities, an excess energy would arise from the variation of the grand potential across the interface. This excess energy increases with the difference between the equilibrium compositions of the phases and contributes to the interfacial energy. Thereafter results in a reduced equilibrium width of the interface between contributing phases. In order to overcome this problem, the systems with considerably different equilibrium compositions should be simulated with smaller length scales. Consequently, the equilibrium interface widths has to be much smaller than the smallest morphological feature. However, these length scales are not interesting for studying the solidification processes. The solution for this restriction was proposed by using of individual concentration fields for all phases [100–102]. So that it is possible to simulate the solidification process with considering the appropriate length scales. Plapp and coworkers [103] have proposed an alternative to the use of separate concentration fields. Their proposed model is based on a grand potential functional. The simulations performed in this work are conducted with MICRESSTM which is based on a common free energy functional considering the diffusive interface and applies the most recently improved multiphase-field model by Eiken et al. [102, 104].

In their proposed model, Eiken et al. [102], formulated a general model of the free energy as an integral of the density functional over the domain Ω , in which the density

functional is a function of multiple phase fields $\{\phi_\alpha\}$ and the phase composition fields $\{\vec{c}_\alpha\}$. The following details will discuss their model briefly and the reader is referred to reference [102] for full details.

Eiken et al. [102] considered the density functional split into the interface energy density ($f^{intf}(\{\phi_\alpha\})$) and the chemical free energy density ($f^{chem}(\{\phi_\alpha\}, \{\vec{c}_\alpha\})$) as following:

$$F(\{\phi_\alpha\}, \{\vec{c}_\alpha\}) = \int_{\Omega} f^{intf}(\{\phi_\alpha\}) + f^{chem}(\{\phi_\alpha\}, \{\vec{c}_\alpha\}) \quad (3.5)$$

The interfacial free energy density is expanded in the phase-field variables $\phi_{\alpha=1,\dots,\nu}$ of the system with ν phases considering the constraint $\sum_{\alpha=1}^{\nu} \phi_\alpha = 1$ so that:

$$f^{intf} = \sum_{\alpha,\beta=1}^{\nu} \frac{4\sigma_{\alpha\beta}}{\eta_{\alpha\beta}} \left(-\frac{\eta_{\alpha\beta}^2}{\pi^2} \nabla\phi_\alpha \cdot \nabla\phi_\beta + \phi_\alpha\phi_\beta \right) \quad (3.6)$$

Where the $\sigma_{\alpha\beta}$ is the interface energy between phase α and phase β and the $\eta_{\alpha\beta}$ denotes the interface width. For the free energy density of a multicomponent multiphase system, they have the Gibbs free energy considered, which can be described by the chemical potentials μ_α^i of the every component i in the phase α and respective moles number n_α^i :

$$G = \sum_{\alpha=1}^{\nu} \sum_{i=0}^k \mu_\alpha^i n_\alpha^i \quad (3.7)$$

where

$$\mu_\alpha^i = \left(\frac{\partial G_\alpha}{\partial n_\alpha^i} \right)_{n_\alpha^{j \neq i}, T} \quad (3.8)$$

They have considered $k + 1$ solute compositions (c_α^i) for each individual phase α and rewrote the Gibbs free energy as following:

$$G = \sum_{\alpha=1}^{\nu} n_\alpha \sum_{i=0}^k \mu_\alpha^i c_\alpha^i \quad (3.9)$$

with considering

$$c_\alpha^{i=0,\dots,k} = \frac{n_\alpha^i}{n_\alpha} \quad (3.10)$$

The considered solute composition in this equation, which show the mole fractions, must fulfill the constraint $\sum_{i=0}^k c_\alpha^i = 1$. Therefore, the component 0 was considered as solvent and consequently $k + 1$ dependent mole fraction $c_\alpha^{i=0,\dots,k}$ got reduced to k independent mole fractions $c_\alpha^{i=1,\dots,k}$ and the Gibbs free energy got reformulated as following:

$$G = \sum_{\alpha=1}^{\nu} n_\alpha \left(\mu_\alpha^0 c_\alpha^0 + \sum_{i=1}^k \mu_\alpha^i c_\alpha^i \right) \quad (3.11)$$

In which would be equal to:

$$G = \sum_{\alpha=1}^{\nu} n_{\alpha} (\mu_{\alpha}^0 + \sum_{i=1}^k \tilde{\mu}_{\alpha}^i c_{\alpha}^i) \quad (3.12)$$

With considering

$$\tilde{\mu}_{\alpha}^i = \mu_{\alpha}^i - \mu_{\alpha}^0 \quad (3.13)$$

The term indicated in parentheses in the equation 3.12 denotes the molar free energy density of phase α , and $\tilde{\mu}_{\alpha}$ is its partial derivative with respect to composition (g_{α}). With this definition we will have:

$$g_{\alpha} = \mu_{\alpha}^0 + \sum_{i=1}^k \tilde{\mu}_{\alpha}^i c_{\alpha}^i \quad (3.14)$$

With considering:

$$\tilde{\mu}_{\alpha}^i = \mu_{\alpha}^i - \mu_{\alpha}^0 = \left(\frac{\partial g_{\alpha}}{\partial c_{\alpha}^i} \right)_{c_{\alpha}^{j \neq i}, T} \quad (3.15)$$

It is worth to mention that gradient of the potential $\tilde{\mu}_{\alpha}^i$ determines the chemical driving force for solute diffusion within a phase and is called phase diffusion potential in the following considerations. The molar free energy density of the multicomponent multiphase system is derived from division of the free energy G by the total number of moles n and is formulated as following:

$$g = \frac{1}{n} \sum_{\alpha=1}^{\nu} n_{\alpha} g_{\alpha}(c_{\alpha}^i) \quad (3.16)$$

In which the g_{α} is considered to be as indicated in equation 3.14. The correlation 3.16 could be re-written in following form:

$$g = \sum_{\alpha=1}^{\nu} P_{\alpha} g_{\alpha}(c_{\alpha}^i) \quad (3.17)$$

Where the P_{α} denotes $\frac{n_{\alpha}}{n}$ and shows the phase fractions. The molar Gibbs free energy density of a multicomponent multiphase system is described by the sum of the free energy densities of the individual phases ($g_{\alpha}(\vec{c}_{\alpha})$) weighted by phase fractions P_{α} . It should be indicated that the free energy densities of the individual phases depend on the individual phase compositions c_{α}^i and the total molar fraction of a component i in the whole system follows the correlation below:

$$c^i = \frac{n^i}{n} = \frac{1}{n} \sum_{\alpha=1}^{\nu} n_{\alpha}^i = \sum_{\alpha=1}^{\nu} P_{\alpha} \vec{c}_{\alpha} \quad (3.18)$$

The phase fractions of the individual phases in the phase-field model proposed by Eiken et al. [102] are considered by the local values of the phase fields $\phi_\alpha(\vec{x}, t)$. According to equation 3.16, in order to formulate the chemical part of the free energy density functional for a multiphase system, the sum of free energy densities of the individual phases (f_α) weighted by respective phase field should be considered. The chemical free energy density could be shown as below:

$$f^{chem}(\phi_\alpha, \vec{c}_\alpha) = \sum_{\alpha=1}^{\nu} \phi_\alpha(\vec{x}, t) f_\alpha(\vec{c}_\alpha(\vec{x}, t)) \quad (3.19)$$

In the phase-field model of Eiken et al. [102], molar Gibbs free energy densities are considered for describing the total free energy functional. They have assumed that the molar volumes of all phases are equal and independent of composition could be expressed as: $\nu_\alpha^m = \nu_m$, so the volume free energy densities can be replaced by molar Gibbs free energy densities and the chemical free energy density could be formulated as follows:

$$f^{chem}(\phi_\alpha, \vec{c}_\alpha) = \frac{1}{\nu^m} g(\phi_\alpha, \vec{c}_\alpha) \quad (3.20)$$

In which

$$g(\phi_\alpha, \vec{c}_\alpha) = \sum_{\alpha=1}^{\nu} \phi_\alpha g_\alpha(\vec{c}_\alpha) \quad (3.21)$$

The Gibbs free energy densities g_α are functions of the local phase composition fields $\vec{c}_\alpha(\vec{x}, t) = (c_\alpha^i(\vec{x}, t), \dots, c_\alpha^k(\vec{x}, t))$. These phase compositions \vec{c}_α are non-conserved parameters and in this formulation are not independent parameters, but could be linked to the conserved and continuous mixture composition (\vec{c}) by the mass balance,

$$\vec{c}(\vec{x}, t) = \sum_{\alpha=1}^{\nu} \phi_\alpha(\vec{x}, t) \vec{c}_\alpha(\vec{x}, t) \quad (3.22)$$

Using the phase compositions as independent parameters got applied by integrating the mass balance into the functional by an additional Lagrange term $\vec{\mu}$.

$$g(\phi_\alpha, \vec{c}, \vec{c}_\alpha) = \sum_{\alpha=1}^{\nu} \phi_\alpha g_\alpha(\vec{c}_\alpha) + \vec{\mu}(\vec{c} - \sum_{\alpha=1}^{\nu} \phi_\alpha \vec{c}_\alpha) \quad (3.23)$$

The Lagrange multiplier is the mixture diffusion potentials and is defined as the correlation below:

$$\tilde{\mu}^i = \left(\frac{\partial g}{\partial c^i} \right)_{c^j \neq i, T} \quad (3.24)$$

According to the equation 3.20, the mixture diffusion potentials are linked to the individual phase diffusion potentials through the following correlation:

$$\tilde{\mu}^i = \sum_{\alpha=1}^{\nu} \phi_\alpha \sum_{j=1}^k \tilde{\mu}_\alpha^j \frac{\partial c_\alpha^j}{\partial c^i} \quad (3.25)$$

Eiken et al. [102] have made an assumption that local mass transport between co-existing phases within the infinitesimally small volume at position \vec{x} , can occur instantaneously. The phase compositions of all phases and components can thus adjust, leaving the phase field and the mixture compositions constant, but changing the diffusion potentials until a partial minimum of the local free energy is reached in each infinitesimally small volume. This partial minimum, which we call quasiequilibrium, is reached if independent variation of the functional with respect to the c_α^i is equal to zero;

$$\frac{\partial g(\phi_\alpha, \vec{c}, \vec{c}_\alpha)}{\partial c_\alpha^i} = \phi_\alpha \frac{\partial g_\alpha}{\partial c_\alpha^i} - \phi_\alpha \tilde{\mu} = 0 \quad (3.26)$$

Which leads to the constraint that all phase diffusion potentials equal the mixture diffusion potential and thus implicitly equal each other:

$$\vec{\mu}_\alpha = \vec{\mu} \quad (3.27)$$

Considering the quasiequilibrium constraint, the phase compositions get functions of the phase-field parameters and the mixture concentrations. Taking equation 3.27 together with equation 3.11 into account, the functional can be written as follows:

$$g(\{\phi_\alpha\}, \vec{c}) = \sum_{\alpha=1}^{\nu} \phi_\alpha [g_\alpha(\vec{c}_\alpha) - \tilde{\mu}_\alpha \vec{c}_\alpha] + \vec{\mu} \vec{c} \quad (3.28)$$

Which is equal to:

$$= \sum_{\alpha=1}^{\nu} \phi_\alpha \mu_\alpha^0(\{\phi_\alpha\}, \vec{c}) + \vec{\mu} \vec{c} \quad (3.29)$$

Where μ_α^0 is the chemical potential of the solvent component.

The equations from 3.5 to 3.29 show how Eiken et al. [102] have gathered the free energy functional to be applied in the phase-field model. As it was mentioned before, investigating the evolution of the phases during a phase transition requires to determine the changes of phase-field variable ϕ which is shown as $\dot{\phi}$. According to [105] the multiphase-field equations are derived for general multiphase transformations in multiple junctions follows:

$$\dot{\phi}_\alpha = - \sum_{\beta=a}^{\tilde{\nu}} \frac{\tilde{M}_{\alpha\beta}}{\tilde{\nu}} \left(\frac{\partial F}{\partial \phi_\alpha} - \frac{\partial F}{\partial \phi_\beta} \right) \quad (3.30)$$

Where the $M_{\alpha\beta}$ stands for the interface mobilities. The parameter $\tilde{\nu}$ denotes the number of phases which are locally in contact. In this regard, $\tilde{\nu}=1$ represents the bulk, $\tilde{\nu}=2$ shows the dual interfaces and $\tilde{\nu}=3$ denotes the triple junctions.

The common numerical method for phase-field modeling method is finite difference approach. To discretize the equations, an ordinary first approach is applied for the

first and second spatial derivatives:

$$\nabla(c) \simeq \frac{c_{i+1} - c_{i-1}}{2x} \quad (3.31)$$

and

$$\nabla^2(c) \simeq \frac{c_{i+1} + 2c_i - c_{i-1}}{x^2} \quad (3.32)$$

As it is mentioned before, the phase-field modeling is powerful method to investigate the phase evolution during the transitions. For the present work, the phase-field method was applied to investigate the development of different phases under various alloying conditions such as temperature and composition of components within Mo-Si-B system. The following chapters provide more details on considering the parameters for setting up the model and corresponding results.

4 Aim and outline of the present thesis

Simulations provide the ability to investigate the engineering processes within fewer time consumption in comparison to experiments. Besides, it was shown in chapter 2 that the Mo-Si-B system offers a wide range of opportunities for being applied in future high temperature industries. But devising an alloy presenting optimized microstructure with balanced properties for using in the high temperature applications is still challenging. Mechanical properties of materials are inspired by microstructure and in order to understand the microstructure evolution of the considered alloy systems, the solidification path and sequence of solidification reaction should be studied. From the literature and previous works it is conferred that the liquidus projection and solidification path of the Mo-rich Mo-Si-B alloys and chemical composition of formed phases are not sufficiently well investigated numerically. Specifically, a comprehensive model which is capable to explore microstructure and solidification behavior of Mo-rich Mo-Si-B alloys has been never developed.

Considering the criteria which are discussed so far, the objective of the present research is to develop a phase-field based model to study the phase transition and microstructure development of Mo-rich Mo-Si-B alloys which are located in so called “Berczik triangle” [50, 51] region. To achieve this goal, it is considered that the model must be capable to simulate the solidification behavior of alloy with ternary eutectic composition, as well as the alloys which present Mo_{55} , Mo_5SiB_2 and Mo_3Si primary phase during the solidification. In case of studying the solidification behavior of ternary eutectic composition alloy, the volume fraction of different phases as well as the chemical composition of the constituting phases has been monitored to monitor the accuracy of the outcome of the model. Moreover, the influence of different operational situations on the growth stability of eutectic lamellae within the solidification domain was evaluated. In order to investigate the accomplishment of the developed model in simulating the solidification behavior of the alloys with near eutectic composition, several compositions were selected from Mo_{55} , Mo_5SiB_2 and Mo_3Si primary regions based on the thermodynamic calculations of Yang and Chang [78, 78] and the phase transition reactions as well as the microstructure evolution and chemical composition of the formed phases have been evaluated to monitor the reliability of the model.

In the following chapters the simulation procedures will be explained and the obtained results in terms of microstructure evolution and solidification path of the considered alloys will be presented and discussed. In the section 6.1 the microstructure,

fraction of different phases and concentration of the components within different phases formed during ternary eutectic solidification are shown and discussed. In the section 6.1.3, the circumstances leading to most stable ternary eutectic Mo-Si-B lamellae growth at specific solidification velocity is evaluated and compared to the analytical expression of Jackson and Hunt [106]. This is proved that there is an acceptable concordance between the theoretical expression of Jackson-Hunt theory, and obtained phase-field simulation results.

Thereafter, the microstructure and phase composition for different near-ternary eutectic Mo-Si-B alloy compositions are presented and discussed. Particularly, the solidification path for the considered alloys is demonstrated. Investigating the solidification path identifies the sequence of phase transition reactions arising during solidification of the considered alloys. Thus, this work provides a comprehensive and important contribution for understanding the solidification behavior of Mo-rich Mo-Si-B alloys.

5 Simulation procedure

This chapter provides the detailed overview of the thermodynamic and kinetic parameters applied to phase-field model for simulating the solidification procedure of different alloys with various considered compositions. In order to develop a model which is capable to simulate the solidification behavior of alloys located at “Berczik” area, adequate number of alloy compositions from this region were considered in the simulations. The considered compositions include the ternary eutectic composition and the compositions located in three primary solidification regions; Mo_{55}Si , Mo_5SiB_2 and Mo_3Si based on thermodynamic calculations of Yang and Chang [78, 79]. In the framework of the present thesis, a 2D simulation domain was considered to model the solidification behavior of ternary eutectic Mo-Si-B alloy composition and the outcome of the model including the phase distribution pattern and volume fraction of the phases as well as distribution pattern of the components within the phases have been compared to the experimental observations of Krüger et al. [27]. Moreover, the growth behavior of the eutectic lamellae has been evaluated under different solidification conditions and the outcome of the model has been compared to the analytical expression of Jackson and Hunt [107]. Although the 2D simulations have resulted in precise prediction of solidification behavior of the ternary Mo-Si-B composition, the morphology of the referred composition was not visually absolutely compatible with the experiments. Therefore, the simulations got extended to 3D by considering the third simulation domain boundary. Which resulted in very precise prediction of microstructure of ternary Mo-Si-B composition however, the required simulation time turned to be very long considering the available processors. Therefore, to eliminate the time barriers of the 3D simulations, the simulations for the near eutectic compositions which have a primary solidification phase were performed in 2D. In order to apply thermodynamic parameters of the Mo-Si-B system within the developed model, Yang and Chang’s thermodynamic calculations [78, 79] were considered. It is worth to mention that the thermodynamic calculations of Yang and Chang [78, 79] are not the most recent evaluation of the Mo-Si-B system and as the Hasemann et al. [81] have reported in their recent experimental investigation, there are a few uncertainty in the thermodynamic calculations of Yang and Chang [78, 79]. However, the investigations of Hasemann et al. [81] is a state of the art research and their achievements are not still transferred to thermodynamic databases. As it is discussed before, the outcome of the Hasemann et al. [81] work reveals that the primary solidification regions, specially Mo_3Si region contains a wider range of compositions in comparison with the calculations of Yang and Chang [78, 79]. This implies that there are more

alloy composition within Mo-Si-B system which tend to form Mo_3Si primary phase during solidification. Besides the Mo_3Si primary area, the Mo_5SiB_2 region contains slightly wider range of compositions as well. Wider Mo_5SiB_2 primary region makes the $\text{Mo}_{5\text{SS}}$ to include slightly fewer range of alloy compositions. Therefore, in order to select the alloy compositions for considering within the model, it has been tried to consider the calculations of Yang and Chang [78, 79] as well as the work of Hasemann et al. [81] to make sure that both researches have agreement on the primary phase during the solidification of selected compositions. As conclusion it can be mentioned that the present work has been conducted within two major categories: the phase-field based simulations for modeling the microstructure and phase distribution pattern of the ternary eutectic Mo-Si-B alloy composition in both two dimensional and three dimensional simulation domain, and the simulations for investigating the solidification behavior of near eutectic alloys within 2D simulation domain. The figure 5.1 gives a schematic overview of the work flow followed in the present work.

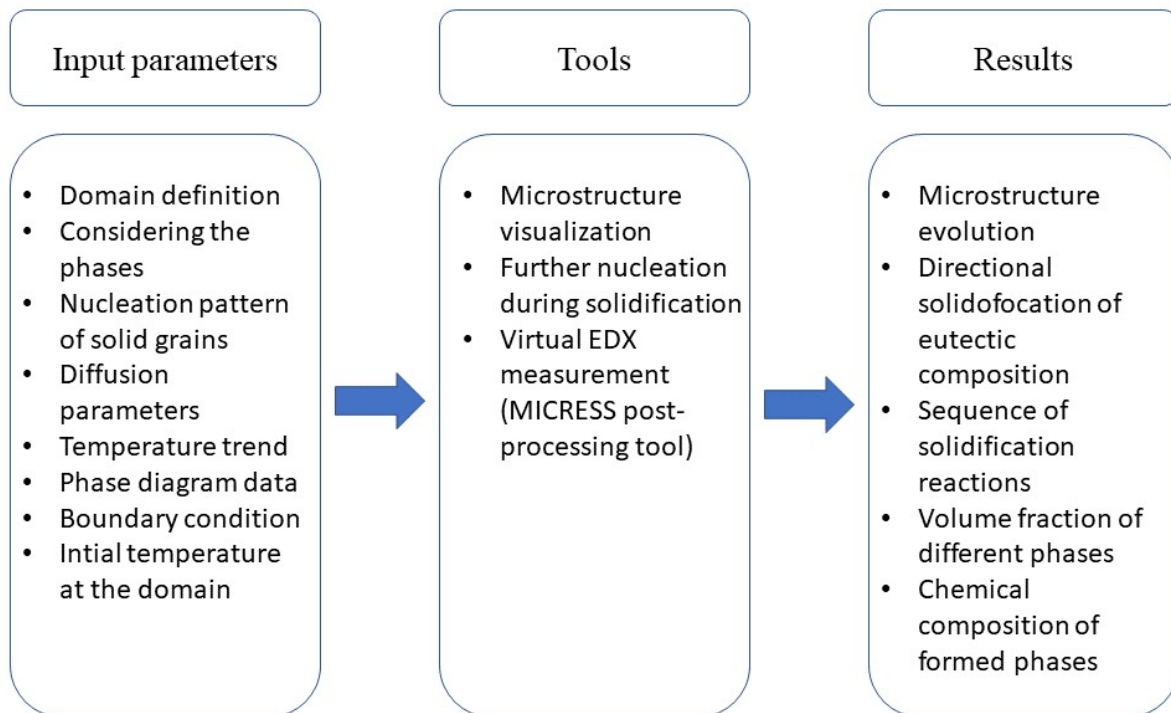


Figure 5.1: The work flow followed in present research for performing the phase-filed simulation of microstructure evolution.

5.1 Diffusion parameters

According to the definition and formulation of the phase-field method, described in chapter 3, diffusion coefficients must be specified for all contributions, i.e. for each component in each phase which is required to consider the concentration field within phase-field simulation. The diffusion flux of the corresponding elements into the considered phases is given by the Fick's first law [108]:

$$J = -D \frac{d_c}{d_x} \quad (5.1)$$

Where J is the flux of the species ($molcm^{-2}s^{-1}$), D represents the diffusion coefficient (cm^2/s) and c is the concentration of the component. It is considered that the diffusion of every component into a phase is caused by the composition gradient of the same element. At the time of writing this thesis, there is no experimentally verified diffusion information for the considered intermetallics. Therefore the required diffusion parameters were considered through approximating the values based on diffusion parameters of materials with similar lattice structure and inverse optimization. Afterwards the accuracy of the considered values were verified by controlling the chemical composition of the formed phases during the solidification as well as the volume fraction of the corresponding phases. For controlling the reliability of the results, an special attention has been paid to the outcome of the ternary eutectic solidification modeling. The reason for calibrating the diffusion parameters based on the solidification behavior of ternary eutectic composition is because of eutectic growth mechanism. Understanding the microstructure evolution mechanism eutectic solidification has been a major topic of several researches in the field of solidification science. The efforts on understanding the mechanism of eutectic solidification has been conducted since 1900s [109]. Brandt [110] has considered the eutectic growth as a diffusion controlled process and introduced the solution for the diffusion equation of eutectic transition. This was the most significant quantified understanding of eutectic growth at the time and all of the proceeding efforts to understand and describe the eutectic growth is based on the Brandt [110] work. Considering the ternary eutectic reaction as a diffusion controlled invariant phase transition without degree of freedom implies that having the precise diffusion information of the components within the phases is determinant milestone for achieving the most precise results through the simulations. Therefore, comparing the outcome of the model with experimental observations from the point of volume fraction of different phases and chemical composition of the corresponding phases is a certain method to validate the considered parameters. It should be pointed out that the required experimental investigations for validating the assumptions on considered diffusion parameters was performed by Krüger et al. [27]. Table 5.1 shows the considered values in this study.

interacting phases and component	Diff. coefficient prefactor (cm^2/s)
Si in melt	2.0E-04
Si in Mo_3Si	2.0E-05
Si in Mo_5SiB_2	2.0E-08
Si in Mo_{SS}	2.0E-08
B in melt	1.0E-04
B in Mo_3Si	1.0E-05
B in Mo_5SiB_2	1.0E-08
B in Mo_{SS}	1.0E-08

Table 5.1: Diffusion information for the considered species within the different phases

5.2 Temperature trend

As it is mentioned before, two major categories of simulations were performed during present study; **I) ternary eutectic composition alloy solidification simulation** and **II) near-eutectic composition alloy solidification simulation**. For conducting the phase-field simulation, each of these categories require specific temperature trend definition including temperature distribution within the solidification domain, velocity of the temperature changes (cooling rate) and the type of the velocity (stepwise or continuously), and the temperature of the domain at the beginning of simulations. Therefore, definition of the temperature trend was specified in two different ways.

5.2.1 Temperature trend for eutectic composition solidification

For performing the simulations of the ternary eutectic composition solidification Krüger et al.'s [27] experiments were followed and a directional solidification situation was considered so that the solid phases grow parallel to a presumed direction within the solidification domain. Applying the experimental parameters within the developed model provides an opportunity to evaluate the reliability of the model by direct comparison of the simulation results and experimental observations. Therefore, further investigations such as investigating the influence of different operating conditions on the stability of solidification and growth of eutectic composition would be feasible. In order to perform the simulations for studying the directional solidification such as directional solidification of eutectic composition alloy, the continuously changing temperature parallel to the growth direction of the solidification front should be considered. The change of temperature, which is known as thermal gradient (TG), is considered to be equal to $10 K/cm$ after the experimental procedure [27]. In order to apply the driving force for the solidification, the temperature at the bottom of domain where the solidification was supposed to start from, was applied slightly

less than ternary eutectic temperature. The ternary eutectic reaction's temperature was derived from thermodynamic simulations using FactsageTM software utilizing the Yang and Chang's [78, 79] calculated thermodynamic database [111], and is equal to 2264 K therefore, the initial temperature at the simulation domain was considered to be 2263 K to provide the sufficient driving force at the beginning of the simulation. Besides the thermal gradient and initial temperature of the simulation domain, a cooling rate should be considered within the simulation. According to the experimental operation parameter, the temperature of the solidification domain was considered to reduce continuously during the simulation with the rate of 200 K/s .

5.2.2 Temperature trend for near eutectic composition solidification

In order to perform the simulation of solidification for near eutectic alloy compositions, a specific attention should be paid to the temperature trend. The alloy compositions located near ternary eutectic point tend to perform primary solidification reaction. The nature of the arising primary phase depends on the position of the considered composition within the phase diagram and depending to the liquidus projection, the considered alloy composition performs coupled growth of eutectic phases during the solidification. However, the solidification behavior of the alloys with near eutectic composition is influenced by the projected undercooling during the solidification. As it is mentioned before, the considered compositions are located within the primary $Mo_{55}Si$, Mo_5SiB_2 and Mo_3Si region and these primary solidification areas have different liquidus surface slope. Therefore, the different phases show different behavior to the undercooling and consequently undercooling can affect the solidification path strongly. For more detailed information about this phenomenon, the reader is referred to the reference [112]. Moreover, the thermodynamic data applied in the present research are derived from thermodynamic calculations of Yang and Chang [78, 79] which are calculated under equilibrium phase transition assumption. Therefore, to meet the principles of the Yang and Chang [78, 79] calculations, the thermal gradient is not considered within the corresponding models and a very slight amount of continuous cooling rate was applied (1 K/s) consequently. In the simulations, where the directional solidification is not supposed to take place, the temperature is considered to be equal in all voxel cells through the simulation domain. It is worth to mention that the considered temperature trend has resulted in a equilibrium phase transition which was compatible with the thermodynamic calculations of Yang and Chang [78, 79].

5.2.3 Initial temperature

The solidification process is a liquid to solid(s) phase transition. Thus simulation of solidification process requires that the considered domain should be completely occupied with melt at the beginning of simulation (t_0). Therefore, depending the

composition of the considered alloy, the temperature of the domain at the initiation of simulation, which is referred as initial temperature in following for every simulation is derived from thermodynamic database and is considered in such a way that the considered alloy is molten at t_0 . The comprehensive information of the considered temperatures is included in the appendix.

5.3 Phase diagram input data

Thermodynamic data have a great impact on simulating the solidification process. In this regard, the phase diagram input data have been defined for the all phases which have interactions through the solidification process. In order to explain the interaction between phases, data of the liquidus and solidus surfaces of ternary phase diagram at every temperature is required. In this regard, the phase diagram information containing the composition of the phases at different temperatures was derived from various isotherm cross section over the Mo-Si-B ternary phase diagram derived from Yang and Chang [78, 79] thermodynamic database generated by FactsageTM from the reference [111].

To define the constitution of different phases over temperature reduction within the simulations, e.g. from hypothetical temperature A to hypothetical temperature B, two corresponding points at two different temperatures A and B were selected from the both liquidus and solidus surface. Afterwards, the temperature, composition of the points and also the slope of the connecting line between two corresponding points were defined to the simulations. Therefore, the simulations could predict the component distribution and constitution of different phases precisely by considering the rule of lever. It should be considered that the liquidus surface is not uniform therefore the the slope of the connecting line between two corresponding points located at liquidus surface does not preserve a constant value. Hence, several isotherms at phase diagram should be considered and the mentioned phase diagram information should be defined at different temperatures. Figure 5.2 shows the linear phase diagram definition procedure graphically.

5.3.1 Phase diagram input data for eutectic composition solidification

Table 5.2 shows the considered values of phase diagram input data applied in the ternary eutectic solidification simulations. Exploring the data from linerized phase diagram revealed that the liquidus surface at ternary eutectic point becomes very sharp and the slope of the temperature over change of components (dT/dc) tends to infinity. Therefore a certain number (-999) was considered for the infinite slopes within the model. The reason for choosing this number is according to the instruction of the applied software package.

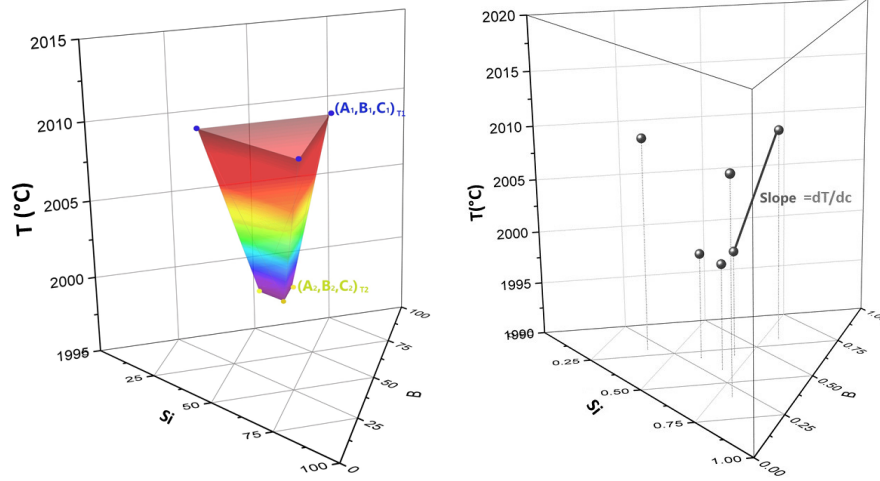


Figure 5.2: Phase diagram linerisation process; two different isotherm cross sections are selected from Mo-Si-B ternary phase diagram and the composition of two corresponding points are derived; one at each temperature. The compositions along with the slope of connecting points are defined to the simulations.

interactive phases	melt and Mo_3Si	melt and Mo_5SiB_2	melt and Mo_{55}
Si content at reference point 1	17	17	17
B content at reference point 1	7	7	7
Si content at reference point 2	25	12.5	0.2
B content at reference point 2	0	25	0.01
Slope $m = dT/dC$ at reference point 1 for Si	80	-80	-80
Slope $m = dT/dC$ at reference point 1 for B	-80	180	120
Slope $m = dT/dC$ at reference point 2 for Si	-999	-999	-999
Slope $m = dT/dC$ at reference point 2 for B	-999	-999	-999

Table 5.2: Phase diagram input data for ternary eutectic solidification simulations derived from [111].

5.3.2 Phase diagram input data for near eutectic compositions

As it is shown in the figure 5.3, the liquidus surface does not change linearly over the temperature, consequently the slope of the compositions over the temperature which is described in this section, would not change linearly. Hence using constant values for the phase diagram input data does not lead to precise prediction of solidification behavior. This concept implies the necessity of defining multiple phase diagram inputs for simulation of the solidification of the near eutectic compositions. In this regard, two isotherm cross sections at 2340 (K) and 2268 (K) have been selected at the phase

diagram and the slope of the change of different components within the considered temperature range have been investigated and applied within the model.

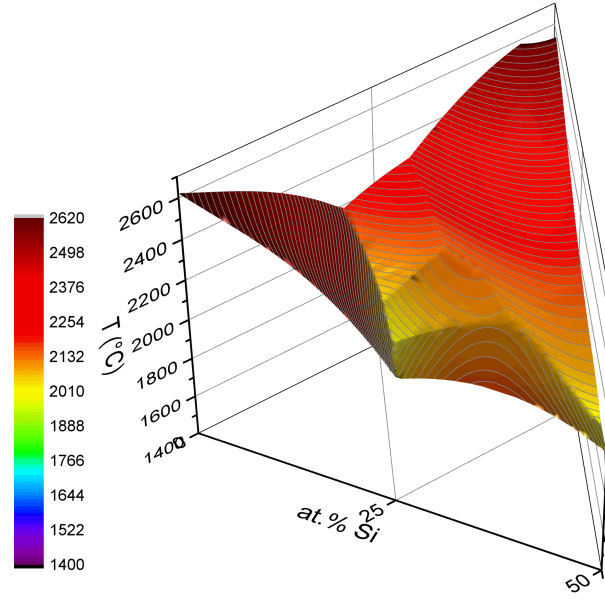


Figure 5.3: Liquidus surface of Mo-Si-B, data based on reference [111].

Table 5.3 and 5.4 show the considered input parameters to describing the phase diagram for alloy compositions located in the Mo_{55} primary solidification region.

interactive phases	melt and Mo_3Si	melt and Mo_5SiB_2	melt and Mo_{55}
Si content at reference point 1	17.9	17.1	16.8
B content at reference point 1	7.2	8.7	6.5
Si content at reference point 2	25	12.5	0.2
B content at reference point 2	0	25	0.01
Slope $m = dT/dC$ at reference point 1 for Si	5	-16.25	-81
Slope $m = dT/dC$ at reference point 1 for B	-5	10	80
Slope $m = dT/dC$ at reference point 2 for Si	-999	-999	-999
Slope $m = dT/dC$ at reference point 2 for B	-999	-999	-999

Table 5.3: Phase diagram input data for solidification simulations of near eutectic alloy compositions for the temperature between 2340 (K) and 2268 (K) based on the information of [111].

interactive phases	melt and Mo ₃ Si	melt and Mo ₅ SiB ₂	melt and Mo ₅ Si
Si content at reference point 1	18.4	17.1	16.5
B content at reference point 1	7.2	12.4	6.5
Si content at reference point 2	25	12.5	0.2
B content at reference point 2	0	25	0.01
Slope m = dT/dC at reference point 1 for Si	8	-24	-82
Slope m = dT/dC at reference point 1 for B	-7.5	10	65
Slope m = dT/dC at reference point 2 for Si	-999	-999	-999
Slope m = dT/dC at reference point 2 for B	-999	-999	-999

Table 5.4: Phase diagram input data for solidification simulations of near eutectic alloy compositions for the temperature between 2268 (K) and below [111].

Table 5.3 and 5.4 show the considered input parameters to describing the phase diagram for alloy compositions located in the Mo₅Si primary solidification region. In order to consider various phase diagram, the simulations have been performed in several steps. At first step, simulation was followed to the destination temperature and in order to consider the updates in phase diagram input data for rest of simulations, the second step of simulation was conducted by applying the outputs of first step as input of simulation with considering the corresponding phase diagram data. This task was provided by MICRESSTM software package.

5.4 Simulation domain

The simulation domain for 2D simulations was considered as a square domain with 48 μm size in X and Y directions. The grid resolution of the simulations domain should be defined so that the most precise results would be achieved within the shortest simulation time. Performing the simulations with several grid resolution has resulted that the considering 600 grid cells in every direction results in desired performance. In order to be able to extend the simulation results to an infinite domain, periodic boundary condition was considered at the solidification domain boundaries. The considered domain and boundary conditions for the simulations of ternary eutectic composition solidification and near eutectic compositions are almost the same but the top boundary at the simulation domain for ternary eutectic solidification simulation is considered to have a fixed boundary condition for concentration fields. Fixed boundary condition considers a fixed value of the composition fields for the boundary cells therefore performing a directional solidification simulation in the direction of bottom to top

boundary would be possible. For the simulations performed within a 3D domain, a 120 μm boundary was considered in third direction (Z).

5.5 Phase interaction data

Interactions between all the considered phases have been defined to fulfill the requirements of phase-field model. The mobility of phases and interfacial energy of all pair wise considered phases; melt, Mo_{SS} , Mo_3Si and Mo_5SiB_2 have been included. Table 5.5 shows the information included in the simulations to define the interactions between phases.

interacting phases	interfacial energy (J/cm^2)	kinetic coefficient cm^4/Js
melt and solids	1E-3	3E-3
solid and solid	1E-3	no mobility

Table 5.5: Data for phase interaction between different phases

5.6 Emerging solid nuclei

The nucleation of the solid phases inside the solidification domain is one of the most important circumstances which should be considered carefully. Technically said, the nucleation of solid grains is the process by which a new grains form within the melt. The complexity of forming a new grain is that the free energy of an emerging nuclei includes both the interfacial and chemical energy density in the formulation and because of the slight surface the interfacial term is relatively high. Therefore, to preserve the energy equilibrium between the nuclei and the melt, a temperature below the melting point of emerging nuclei is required. Depending to the radius of curvature in rising nuclei, there is a certain temperature of equilibrium with the melt and in the case of distinct undercooling, there is a certain amount of curvature radius for nuclei, which is so called “critical radius” and determines how big a nuclei should be to have equal probability of growth or melting. The emerging new solid phases are considered in present research to occur stochastic during the solidification for each phase individually. The considered potential locations for formation of the nuclei were specified both within the melt and at the interface of melt and solid phases. Formation of the solid nuclei of an specific phase depends on the melting point of the considered phase. Therefore, to define the feasible temperature range of solidification, the melting temperature of every phase was considered. Table 5.6 shows the applied criteria for nucleation of solid phases.

parameter	value
position of nucleation seeds	interfaces and bulk of melt
orientation of nuclei	random
checking frequency	every time step
max. temperature for Mo_3Si nuclei (K)	2298
max. temperature for Mo_5SiB_2 nuclei(K)	2473
max. temperature for Mo_{55} nuclei (K)	2896

Table 5.6: considered criteria for predicting the nucleation behaviour of different solid phases. The maximum temperature of nucleation of the solidi phases was derived from thermodynamic database [78, 79].

5.7 Morphology study of directional ternary eutectic solidification

The advantage of the eutectic materials is to provide the ductile phase toughened intermetallic composites. In this regard, the directionally solidified eutectic composites provide several advantages such as making components directly from the melt within a single stage process [113]. However, producing in-situ composites through directional solidification may result in a wide range of microstructure, from well-aligned lamellae to dispersed particles or fibers. The microstructure of the eutectic alloy has a significant impact on the properties of the alloy. For example, a well aligned regular structures containing the fibrous (rod-like) or lamellar constituents offer substantial increases in high-temperature strength, fracture properties, or creep resistance over non-eutectic conventionally cast alloys. Lamellar eutectic growth depends on the interaction between the diffusion required for phase formation and the energy required for formation of interphase boundaries. The lamellar spacing is the result of a balance between these two competing propensities. From one side, the system tends to minimize the lamellar spacing in order to shorten the diffusion path at the interface between the melt and solids, and from the other side, the system tends to increase the lamellar spacing to minimize the interfacial area and consequently the total interfacial energy. This phenomenon and treatment of the balance between these two competing tendencies is comprehensively described by Jackson and Hunt [107]. In order to evaluate the performance of the developed model in predicting the morphology of the ternary eutectic Mo-Si-B composition under different solidification conditions, several simulations with different parameters have been conducted and the outcome of the model was compared with the analytical expression of ternary eutectic solidification behavior provided Choudury et al. [114] which is based on eutectic growth expression of Jackson and Hunt [107].

During solidification of the liquids with eutectic compositions, the liquid decomposes into a composite of solid phases immediately. With applying a continuous thermal gradient in a particular direction, the interface between the melt and solid lamellae which is so called “solidification front” proceeds parallel to the thermal gradient direction. According to the analytical expression of Jackson and Hunt [106], for a constant solidification velocity, the evolution pattern of the lamellae is correlated to the corresponding undercooling at the solidification front. The mathematical expression of the correlation between phase evolution velocity and the size of evolving lamellar or rod like microstructure, and the resulting undercooling at the solidification front for directionally solidified binary eutectic in two dimension solidification domain was first introduced by Jackson and Hunt [115]. Equation 5.2 shows the average undercooling at the solidification front as a function of velocity of solidification front ν and the thickness of one lamellae pair:

$$\Delta T = K_1 \nu \lambda + \frac{K_2}{\lambda} \quad (5.2)$$

where the ΔT is difference between the average solidification front temperature and the eutectic temperature (so called under cooling) and K_1 and K_2 are constants related to the liquidus slopes at the eutectic temperature, the composition difference between the phases, the volume fractions of phases, the interfacial energies between solids and liquid, and the liquid–solid interface shape. According to their formulation, for every considered solidification velocity (ν) the minimum under cooling at solidification front results in most stable growth of eutectic lamellae and the minimum solidification front undercooling happens at specific λ which is called λ_{JH} :

$$\lambda_{JH} = \sqrt{\frac{K_2}{K_1 \nu}} \quad (5.3)$$

Jackson-Hunt model and its successors have devoted their efforts to the binary eutectic systems and different pattern formation during solidification of binary eutectic alloys [106, 115]. The researches in this area got followed later by Himemiya and Umeda by extending the Jackson-Hunt approach to a two dimensional ternary eutectic with $\alpha - \beta - \alpha - \gamma$ pattern and three dimensional chain-like and hexagonal pattern [116, 117]. Choudury et al. [114] have proposed a model to investigate the ternary eutectics with randomly distributed lamellae. To investigate the growth pattern of ternary eutectic composition Mo-Si-B alloy, the proposed model of Choudury et al. [114] was considered in present study. The directional solidification simulation for ternary eutectic Mo-Si-B alloy was performed with considering different size of lamellae at constant solidification velocity and the undercooling at the solidification front for every simulation was measured. The correlation between the size of lamellae and the corresponding undercooling was monitored and the obtained results were compared

with analytical expression of Choudury et al. [114] and an acceptable compatibility between the simulations outcome and analytical expression was observed.

6 Results and discussion

The outcome of the present research endows insight into the phase transition reactions and microstructure evolution during the solidification of the Mo-rich Mo-Si-B alloy compositions. As it is pointed out before, two major group of simulations were performed in the framework of the present work. Firstly, a phase-field based model has been developed to investigate the solidification behavior of ternary eutectic Mo-Si-B composition in both two-dimension and three-dimension solidification domain. The outcome of the developed model including the microstructure evolution pattern, volume fraction of contributing phases and chemical composition of the formed the phases were compared to the experimental observations of Krüger et al. [27] and demonstrated an acceptable compatibility. Moreover, growth stability of lamellae eutectic pattern has been investigated under various operational parameters and the results were compared to analytical expression of Jackson and Hunt [106, 107]. The lamellae growth stability behavior of ternary eutectic Mo-Si-B composition predicted within the developed model has turned to be in an appropriate agreement with the analytical expression of Jackson and Hunt [106, 107].

Secondly, the solidification behavior of near eutectic composition alloys has been investigated through the phase-field based model by considering appropriate thermodynamic data calculated by Yang and Chang [78, 79]. The achievements of the simulations provide appropriate prediction of the sequence of phase transition reactions between the melt and corresponding solid phases as well as microstructure and phase evolution pattern within two dimensional simulation domain for different alloy compositions located in three primary solidification areas Mo_{55}Si , Mo_5SiB_2 and Mo_3Si . The Alkemade theorem was used to have a closer look into liquidus projection of Mo-rich Mo-Si-B alloys published by Yang and Chang [78, 79] and sequence of phase transition reactions predicted by phase-field based model was compared with the referred liquidus projection and it should be mentioned that the present work agrees with the solidification sequence provided by Yang and Chang [78, 79] for the considered alloy compositions. Furthermore, to control the nature of the generated phases during the solidification simulations, the chemical composition of the phases are investigated by exploring the distribution pattern of the components inside the phases.

As it is mentioned before, the most updated thermodynamic database of Mo-Si-B system is based on the Yang and Chang's calculation [78, 79]. However, Hasemann et al. [81] have illustrated within their recent work that there are some uncertainty

about the Yang and Chang's calculation [78, 79]. In particular, the Mo_3Si primary solidification region turned out to be broader in comparison to the liquidus projection predicted by Yang and Chang [78, 79]. The near eutectic alloy compositions considered in the framework of the present research meet the principles of the both works. Technically said, the liquidus projection developed by Yang and Chang's calculation [78, 79] and Hasemann et al.'s experimental investigations [81], agree on the primary solidification phase of the considered alloy compositions.

However, the different liquidus projection may result in different volume fraction of generated phases and consequently different microstructure. This is because with considering different liquidus projections, the considered compositions might be projected to different solidification path within the liquidus surface when the temperature reduces and therefore different solidification reactions might take place. In some instances the different liquidus projections might predict the similar solidification reactions, but the liquidus projections with broader region requires longer path to the constant reaction border, therefore in comparison with the solidification behavior based on the liquidus projection with smaller primary region, more primary phase would be formed during the solidification. In the following sections, a comprehensive comparison between the outcome of the model, thermodynamic calculations of Yang and Chang [78, 79] and experimental results achieved by Hasemann et al. [81] is presented and critically discussed.

6.1 Ternary eutectic solidification

Acquiring expanded functionality and increased efficiency of materials has become progressively more important for next generation innovations in advanced industries such as power generation, transportation and many others. A very useful approach for developing new materials which provide great potential in many applications is to generate multiphase structures directly from the melt through solidification process. Among these multiphase structures, the eutectic structure has absorbed a significant amount of attention because of their unique properties. The eutectic compositions offer relatively low melting points in which results in good fluidity and casting feasibility. Moreover, the possibility of forming in-situ composites within the solidification of eutectic composition alloys provides excessive potential for developing enhanced or new functionality in materials. However, understanding the wide range of possible structures during the eutectic solidification requires the investigation of coupled growth structures.

There are several researches performed on investigation of the solidification of various eutectic alloy systems [118–124]. However, despite showing promising potential for being applied in high temperature applications, a numerical investigation of the

eutectic Mo-Si-B solidification is missing. As it is mentioned before, the formation of a eutectic microstructure is a process controlled by diffusion and depending to the volume fraction of the contributing phases, the coupled growth of two phases results in a two major types of morphology which is either lamellar or rod-like [106, 107]. If the volume fractions of the eutectic phases are close to each other a lamellar structure is preferred and if the difference in volume fraction is large a rod-like or fibrous morphology would be shaped during the solidification. In this case the phase with the higher volume fraction forms the matrix and the minor phases would be distributed like fibers. It is worth to mention that the kinetics of crystal growth can be used to control the lamellar spacing and cell sizes [120, 121, 125].

In the framework of the present study, the pattern formation during Mo-Si-B ternary eutectic microstructures evolution was investigated within 2D and 3D simulation domain and the arrangement of different solid phases within the solidification domain were visualized. Solidification behavior, pattern formation and phase fractions were derived from simulations and compared to experimental observations of Krüger et al. [27].

Based on the thermodynamic calculations of Yang and Chang [78, 78] the eutectic point was found to have a nominal composition of Mo-17.5Si-8B (at.%). Exploring the chemical composition of the melt during the solidification has revealed that the Mo-17.5Si-8B (at.%) composition is preserved within the melt during the simulation, which is because of the considered boundary condition at the top of domain. Moreover, conducting the simulation and probing the growth pattern and arrangement showed that the solid phases tend to create a composite of Mo_5SiB_2 and $\text{Mo}_{5\text{Si}}$ lamellae within the matrix of Mo_3Si phase. Although an ordered lamellae pattern was not observed, however the arrangement pattern looks to be close enough to a semi-lamellae pattern. So for the further investigations we have considered it as lamellae configuration. The reason for not demonstrating obviously the lamellae pattern during the solidification may possibly be because of the volume fraction of the solid phases. According to the outcome of the simulations, the volume fraction of phases would be 50 % for the Mo_3Si , and the Mo_5SiB_2 and $\text{Mo}_{5\text{Si}}$ solid phases tend to have almost equal volume fractions. This circumstance was clearly observed within the experimental investigations of Krüger et al. [27]. Figure 6.1 shows the microstructure of ternary eutectic Mo-Si-B alloy compositions accomplished by simulations.

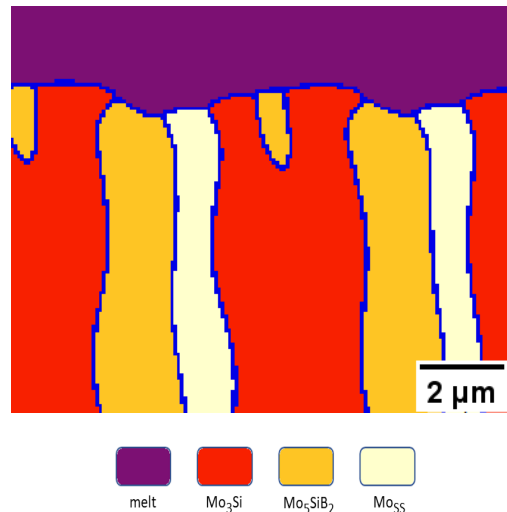


Figure 6.1: Microstructure and Lamellae growth pattern observed in the directional solidification simulations of ternary eutectic Mo-Si-B alloy composition.

6.1.1 3D simulation of eutectic solidification

The 2D simulation of the ternary eutectic Mo-Si-B alloy composition has revealed that morphology of the ternary eutectic Mo-Si-B composition is of lamellar pattern which demonstrates a cooperative growth of $\text{Mo}_{5\text{Si}}$ and $\text{Mo}_{5\text{SiB}_2}$ lamellae within the matrix of Mo_3Si . Although the 2D simulations have demonstrated the ternary eutectic phase transition precisely and have illustrated the fraction of different phases correctly, however they do not offer the appropriate visual expression of the microstructure of ternary systems as much as the 3D simulations do. The microstructure obtained through a 3D simulations seems more realistic than the microstructure achieved through 2D simulations. It may be expected that microstructure at the middle layer of added third dimension is quite similar to what is obtained from 2D simulations, but not necessarily similar to the other layers of the 3D picture. Thus 3D simulations offer more realistic vision of microstructure evolution of a ternary system than 2D simulations because they can capture composition gradients as well as boundary conditions along the third direction that is not considered in 2D simulations. However, the computational burden of a 3D simulation is higher than 2D simulation, therefore it is necessary to consider the interested directions of spatial gradients of the variables along with the simulation cost (e.g. time and required processors) as well as the accuracy of obtained results to make decision whether a 2D or 3D simulation is required. Therefore, to have a clear vision of the phase distribution pattern during the ternary eutectic Mo-Si-B solidification, a 3D simulation was conducted whereby the result is demonstrated in figure 6.2.

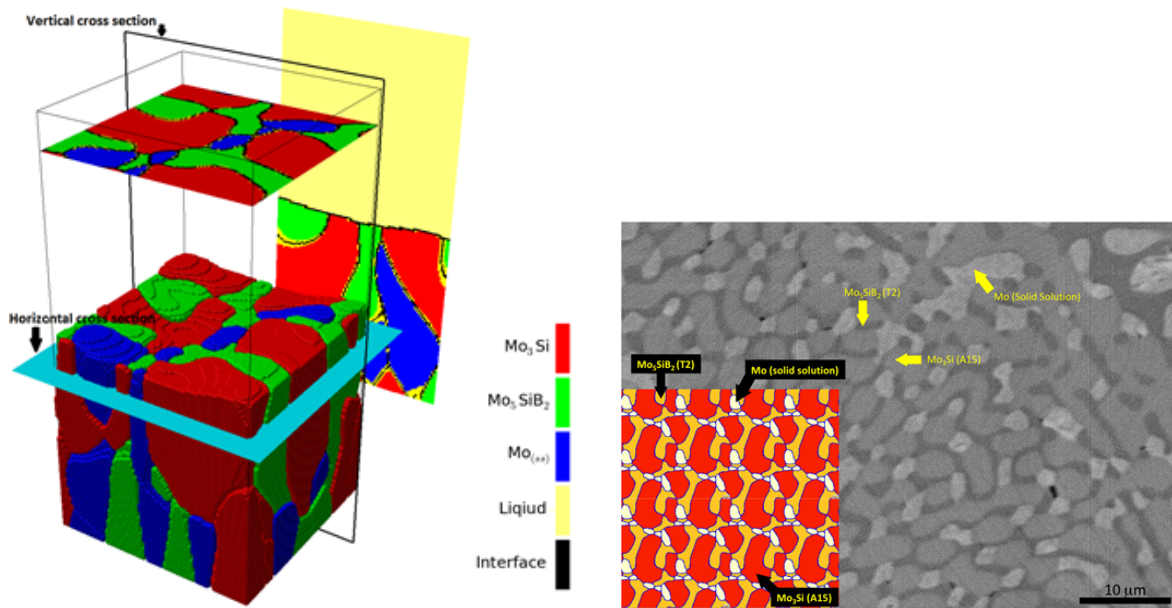


Figure 6.2: 3D simulation of ternary eutectic composition Mo-Si-B alloy solidification (left picture) and a perpendicular cross section of lamellae growth direction along with the experimental observations (right picture). On the left picture the data for the vertical and horizontal cross sections are projected onto a parallel virtual plane for better visualization.

6.1.2 Component distribution pattern

The chemical composition of the constituting phases was monitored within the simulation's results by observing the distribution of the components within the phases. In this regard, the element concentration along the indicated line in the figure 6.3 has been examined. It was observed that among the solid phases the elements have a constant concentration, however, at the interface between phases there is a thin diffusion boundary. The amount of the elements is in particularly good agreement with the expected concentrations in the three phases. The interfaces between phases were considered as a layer with three cells in width. This is in contrast to the classical sharp interface assumptions. During the evolution of the solidification, the non-required elements will be enriched in the interface, respectively. Therefore, a concentration gradient will result at the interface, which affects the average temperature and composition of the interface. This will consequently control the solidification instabilities and cause the potential initialization of further nucleation [126]. The concentration profiles showing small varieties of the phase compositions at the interfaces are presented in figure 6.3.

6.1.3 Effects of solidification conditions on lamellae growth structure

Several studies have reported that the microstructure can be controlled by the solidification conditions [113, 127, 128]. To evaluate the influence of the solidification condition on the ternary eutectic morphology, the solidification simulations were per-

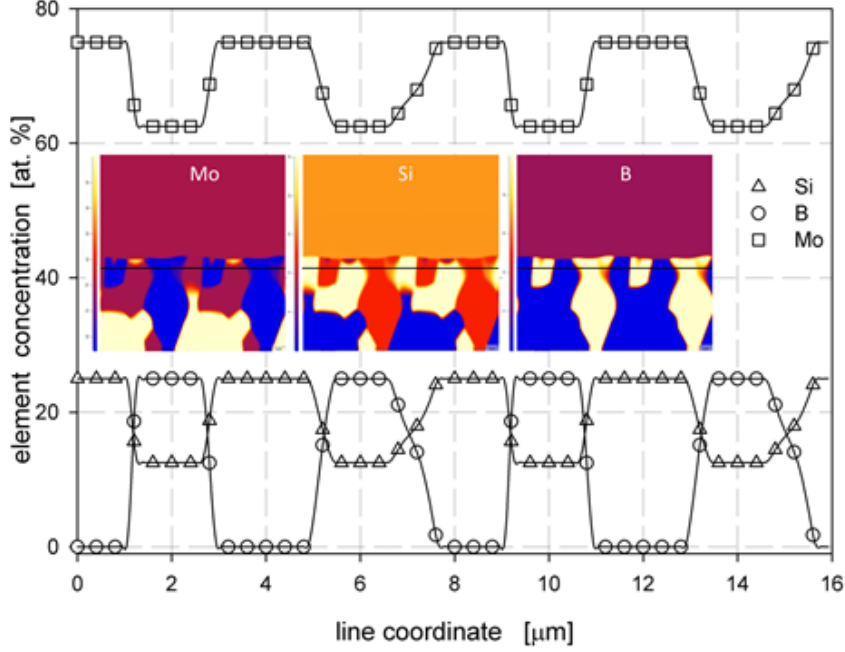


Figure 6.3: Concentration distribution of component. The value of each element along with the illustrated line is revealed.

formed with different conditions based on the assumption of Choudhury et al. [114] and the predictions of the model on the morphology of ternary eutectic Mo-Si-B got verified with the outcome of the analytical expression of Choudhury et al. [114].

To apply the hypothesis of Choudhury et al. [114], the simulations were performed at constant solidification velocity as adapted from [129] equal to $v = 0.05 \mu\text{m}/\text{s}$. The velocity got tracked during solidification by monitoring the progressing velocity of the solidification front into the melt. The simulations were performed with different lamellae spacing presenting $\text{Mo}_3\text{Si}-\text{Mo}_5\text{SiB}_2-\text{Mo}_{55}\text{Si}_{45}$ structure based on experimental observations [27] and consequently the undercooling at the solidification front were measured during the solidification. In order to measure the undercooling, the temperature at the interface of solids and melt was measured. For keeping the simplicity, it was assumed that undercooling at whole solidification front is unified. Table 6.1 shows the different considered lamellae spacing versus consequence undercooling.

lamellae spacing (μm)	1	2	3	6	7	12
resulting undercooling (K)	0.87	0.63	0.27	0.09	0.08	0.3

Table 6.1: Different considered lamellae spacing in simulation of ternary eutectic Mo-Si-B alloy solidification and corresponding undercooling at solidification front.

According to the table 6.1 and considering the theory of Jackson and Hunt, the most stable lamellae growth should emerge in the simulations with lamellar spacing equal to $6 \mu\text{m}$. As it is shown in the figure 6.4, the most stable and well-aligned lamellae growth without any tilting or oscillating emerges at the lamellae spacing of $6 \mu\text{m}$, where the minimum undercooling takes place according to table 6.1. Therefore, for the particularly specified solidification growth velocity, the λ_{JH} was defined equal to $6 \mu\text{m}$.

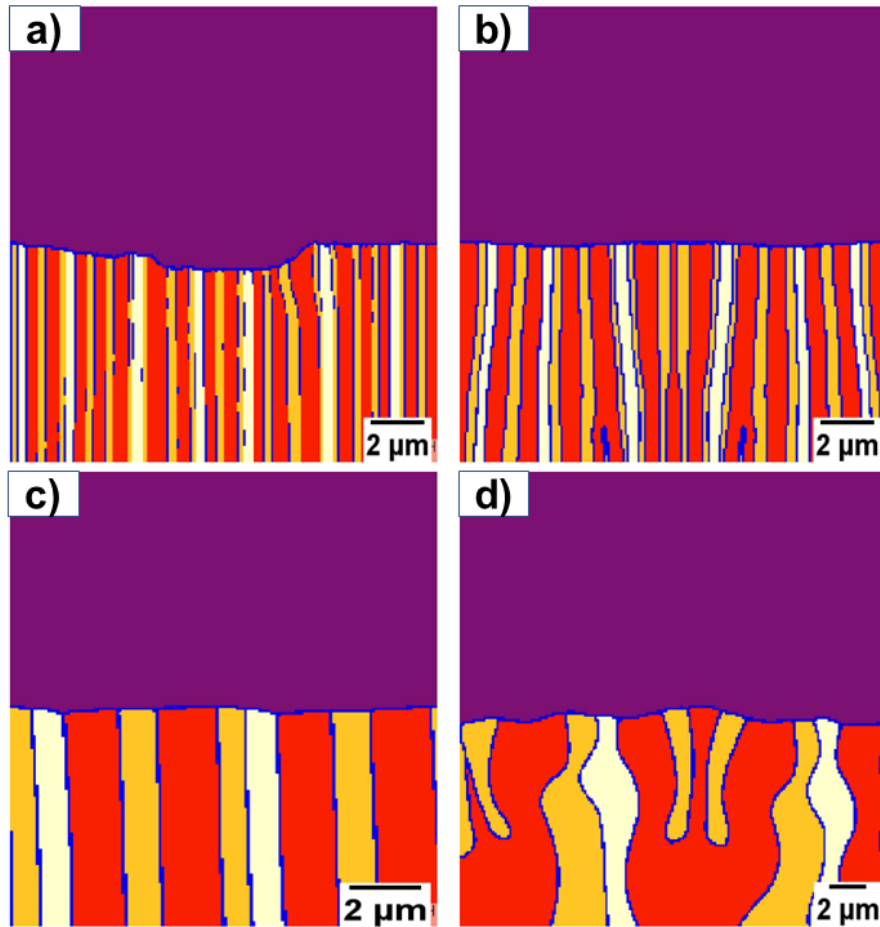


Figure 6.4: Different lamellar growth pattern predicted by the developed model at considered growth velocity for the various lamellae spacing: a)1 b)2 c)6 d)12 μm .

To evaluate the accomplishments of the model, the analytical expression proposed by Choudhury et al. [114] was modeled and the outcome of the Choudhury et al. model's prediction was compared to the phase-field simulation's result. According to the figure 6.5, predictions of phase-field simulations are in a good accordance with analytical expression.

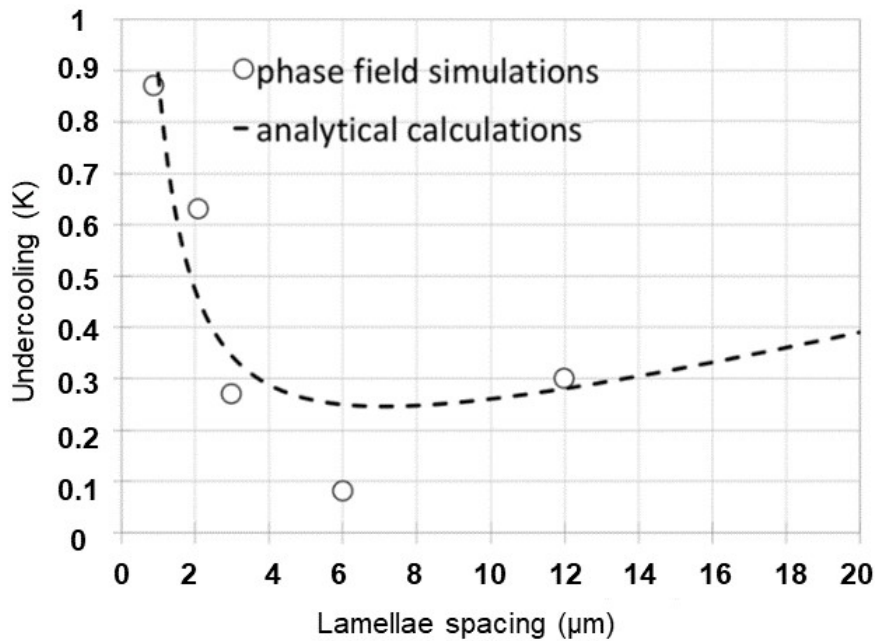


Figure 6.5: A comparison between the prediction of phase-field simulations of ternary eutectic Mo-Si-B alloy composition and analytical expression of Choudhury et al. [114].

6.2 Near eutectic compositions

In this section the outcome of the developed model for simulating the solidification behavior of the near eutectic alloy compositions is presented and discussed carefully. The considered compositions are located in different primary solidification regions and relatively close to the ternary eutectic point based on Yang and Chang's thermodynamic calculations [78, 79]. However, the validation of the developed model turned out to be challenging. Based on the performance of the model on the simulating the solidification behavior of the ternary eutectic Mo-Si-B alloy composition which is already discussed in the previous sections, the reliability of the model has been verified by direct comparison with the experimental observations. However, as it is mentioned before, the near eutectic compositions tend to form a primary phase during solidification. These primary solidification reactions change the composition of the melt toward various binary solidification regions. In order to verify the accuracy of the developed model and consequently the reliability of the considered parameters, it is crucial to observe the precise phase transitions reactions during the solidification simulations. Hence, the experimental observations are required to control the validity of the model. Various experimental investigations on the solidification behavior of the Mo-Si-B alloys have been conducted and their achievements are already reported within the literature [53, 80] which can provide the potential references for controlling the reliability of the developed model as well as the considered parameters. However, As it is referred

within the present thesis before, Hasemann et al. [81] have conducted the most comprehensive experimental investigation on the Mo-Si-B alloys. They have investigated solidification behavior of several alloy compositions and have reported that there are some uncertainties about the primary phase regions within the liquidus projection of Mo-Si-B system derived from Yang and Chang's thermodynamic calculations [78, 79]. Consequently, they have reported a new liquidus projection for Mo-Si-B system. According to Hasemann et al. [81], their experiments on the Mo-Si-B liquidus projection are in good agreement with the Yang and Chang's investigations [78, 78] in general. However, a much larger primary solidification area of the Mo_3Si phase was determined which has a significant impact on the microstructure evolution of alloys located in this primary solidification region.

In order to confirm that comparing the solidification path of the considered compositions within the simulations based on the thermodynamic data of Yang and Chang's calculations [78, 79] with experimental results of Haseman et al. [81] is an adequate approach for validation the reliability of the model, the liquidus projection represented by Yang and Chang [78, 78] has been compared with the liquidus projection represented by Hasemann et al. [81] by applying the Alkemade theorem. The Alkemade theorem indicates that if primary crystallization regions of two stoichiometric phases have a common boundary, then along this boundary the temperature is maximal at the point where it is crossed by a straight line which connects the composition points of these phases [82]. Therefore, it is possible to estimate local maxima (more precisely saddle points) along eutectic valleys by applying the Alkemade line. Knowing the local maxima is immensely helpful in determining solidification paths of various alloys in one system consequently can be useful to predict the possible phase transitions reactions. Figure 6.6 shows the liquidus surface predicted by Yang and Chang [78, 79] and achieved by hasemann et al. Hasemann et al. [81], including the Alkemade line between the stoichiometric Mo_3Si (Mo-25.0Si at.%) and Mo_5SiB_2 (Mo-12.5Si-25B at.%) phase to determine the different phase equilibria which are of the particular interest of the present study. As it can be seen in the pictures, due to the large Mo_5SiB_2 primary solidification area, the Alkemade line does not intersect with the corresponding Mo_5SiB_2 - Mo_3Si eutectic line. However, the referred eutectic line can then be extended until it intersects with the Alkemade line [82, 130]. According to the theorem, the temperature is decreasing left and right of the Alkemade line. Having a closer look at the figure 6.6 reveals that the primary solidification regions and the corresponding binary reactions lines which are the focus of the present thesis are in the same position relative to the Alkemade line within the considered liquidus projection of Yang and Chang [78, 78] and Hasemann et. al. [81]. Therefore, they agree on the solidification path of the alloys located in these regions in general. However, the primary solidification region of the Mo_3Si in the liquidus projection published by Hasemann et al. [81] contains wider range of compositions as compared to the liquidus projection calculated

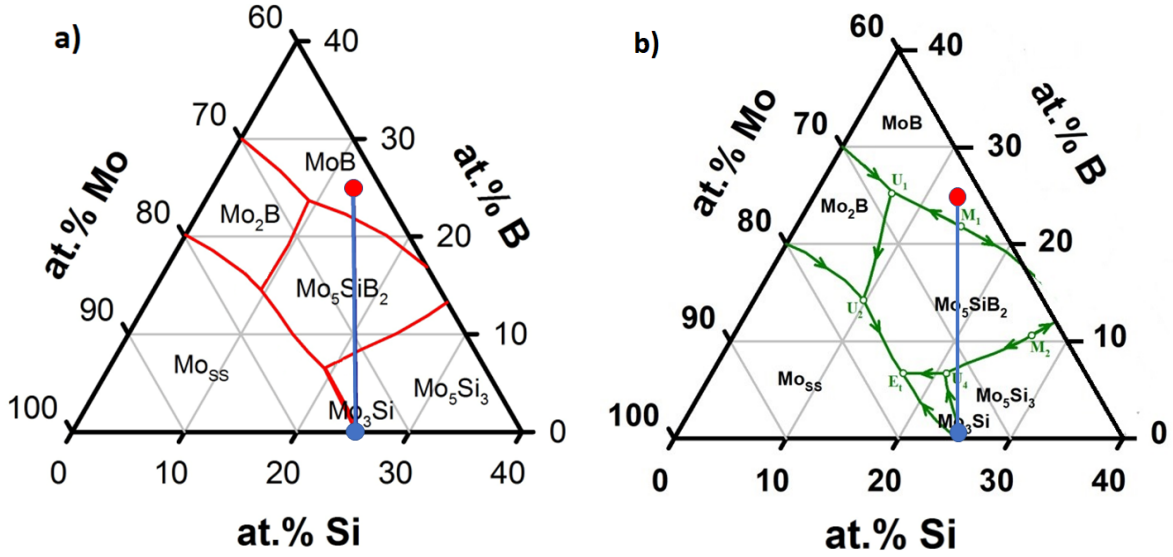


Figure 6.6: Alkemade line between the stoichiometric Mo_3Si (blue point) and Mo_5SiB_2 (red point) in the respective published liquidus projections, a) Yang and Chang [78, 79] b) Hasemann et al. [81].

by Yang and Chang [78, 78]. It conveys that there are some alloy compositions that the mentioned liquidus projections do not agree on their primary solidifying phase. Therefore, in order to select the referral alloy compositions for considering within the simulations of solidification, the alloy compositions are selected from Hasemann et al.'s experiments [81] in which, the primary solidification phase of the considered alloys does not defeat the calculations of Yang and Chang [78, 79]. Afterwards, the sequence of the solidification reactions of the considered compositions predicted by model is compared with the experimental observations of Hasemann et al. [81]. In this regard, the presence of different solid phases at several temperatures has been investigated during the solidification. Exploring the formation of the solid phases through exploring their volume fraction at different temperatures during the solidification provide valued information about the co-operative growth of different phases which leads to the microstructure of the alloy. However, does not provide sufficient information about the nature of the phase transition reactions. Therefore, to identify the phase transition reactions, the solidification path of the considered alloy has been monitored by exploring the chemical composition of the melt during the solidification and has been compared with the liquidus projection provided by Yang and Chang [78, 78].

Besides the solidification path and sequence of the phase transition reactions, the microstructure evolution of the considered composition during the solidification has been investigated. The prediction of the model on the microstructure evolution and phase distribution pattern is represented and compared with the experimental observations of Hasemann et al. [81] and the differences are carefully discussed. In the

framework of the present thesis, the phase diagram and liquidus projection calculated by Yang and Chang [78, 78] has been considered within the model, which is from some viewpoints different with the outcome of the Hasemann et al.'s experiments [81]. Therefore, comparing the predictions of the simulations with the experimental observations of Hasemann et al. [81] can be a useful approach to evaluate the effect of phase diagram, in particular the influence of considering different primary solidification regions on the morphology and phases distribution pattern during the solidification of the alloys. Moreover, in order to control the nature of the predicted phase during the simulations, the component distribution pattern within the solid phases has been monitored.

6.2.1 Selecting the referral compositions

Regarding to the objective of the present thesis, several referral alloys compositions were selected from the “Berczik triangle”, respectively from $\text{Mo}_{5\text{Si}}$, Mo_5SiB_2 and Mo_3Si primary solidification regions considering the criteria discussed so far. The considered compositions were applied within the simulations and their solidification behavior has been examined. The outcome of the simulations are discussed in details and the results of the simulations for different compositions are represented within different categories based on their primary solidifying phase. Table 6.2 shows the chemical composition of the considered alloy compositions.

number of alloy (#)	primary solidifying phase	Si content	B content	Mo content
1	$\text{Mo}_{5\text{Si}}$	15.0	8.0	balance
2	$\text{Mo}_{5\text{Si}}$	16.4	6.7	balance
3	Mo_5SiB_2	15.0	10.0	balance
4	Mo_5SiB_2	18.0	8.0	balance
5	Mo_3Si	20.4	5.0	balance
6	Mo_3Si	20.2	5.8	balance

Table 6.2: considered alloys within the simulations in the framework of the present thesis including their primary solidifying phase [78, 79]. The concentration of the components indicated within table are at. %.

6.3 Solidification reactions of considered compositions

6.3.1 Alloys with $\text{Mo}_{5\text{Si}}$ primary phase

The alloy compositions Mo-15.0Si-8.0B and Mo-16.4Si-6.7B (at.%) are located in the $\text{Mo}_{5\text{Si}}$ primary solidification area according to the both Yang and Chang [78, 78] and Hasemann et al. [81]. The alloys located in this area are supposed to perform a primary solidification reaction to form $\text{Mo}_{5\text{Si}}$ solid phase before going through any other solidification reaction during the solidification process. As it is considered in

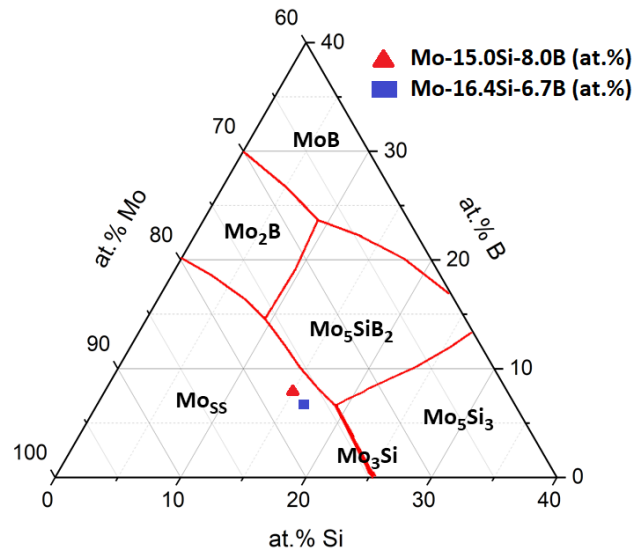


Figure 6.7: Examined alloys with Mo_{SS} primary solidifying phase considering the corresponding liquidus surface [78, 79].

Yang and Chang's calculation [78, 79] and later is verified in the Hasemann et al. work [81], the Mo_{SS} primary solidification area is located between different binary eutectic and peritectic reactions. The compositions considered in this study are chosen from the vicinity of ternary eutectic composition so that the simulations were obsessed only with Mo_3Si , Mo_5SiB_2 and Mo_{SS} phases. The position of the considered alloys from primary Mo_{SS} solidification region within the phase diagram considering the liquidus projection is shown in the figure 6.7.

6.3.1.1 Mo-15.0Si-8.0B (Alloy 1)

In order to have a comprehensive sight of the phase transition reactions during solidification of Mo-15.0Si-8.0B alloy composition, formation of different solid grains within solidification domain and their respective temperature have been monitored. As it is shown in the figure 6.8, the primary Mo_{SS} phase emerges at relatively high temperature. This behavior is expected and caused due to the high melting point of Mo component. Afterwards, a combination of Mo_{SS} - Mo_5SiB_2 forms until the domain reaches to ternary eutectic temperature and the remaining melt turns into ternary eutectic Mo_{SS} - Mo_5SiB_2 - Mo_3Si composition.

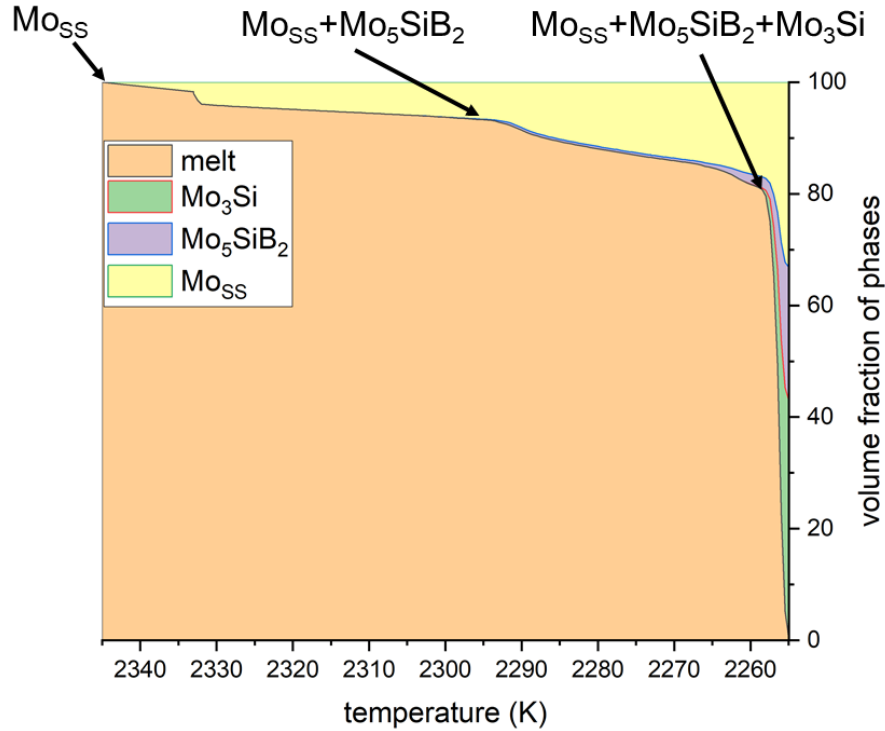


Figure 6.8: Sequence of solidification reactions and volume fraction of different solid phases generating during solidification of Mo-15.0Si-8.0B

Exploring the changes of the chemical composition of the melt during the solidification has revealed that since this composition lies within the single-phase region corresponding to Mo_{SS} phase, the limited amount of solid Mo_{SS} forms primarily from the liquid through the reaction of $L \rightarrow \text{Mo}_{\text{SS}}$. As the system cools down the liquid composition changes and follows the path to the binary Mo_{SS}-Mo₅SiB₂ eutectic valley, where the Mo₅SiB₂ phase is formed in parallel to the Mo_{SS} by the consumption of the liquid phase via $L \rightarrow \text{Mo}_{\text{SS}} + \text{Mo}_5\text{SiB}_2$ transition reaction. With formation of the referred phase through the binary reaction, the composition of the melt changes and solidification path follows the monovariant binary eutectic reaction line until it reaches the nonvariant ternary eutectic reaction point. Figure 6.9 shows the solidification path of the Mo-15.0Si-8.0B alloy composition.

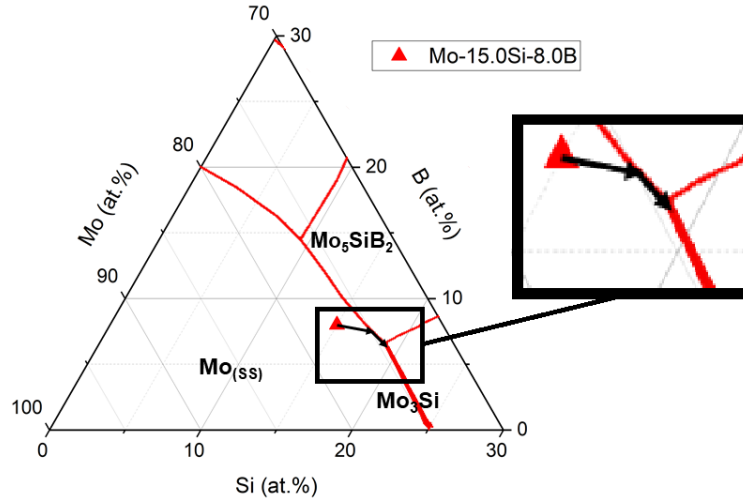


Figure 6.9: Solidification path of the Mo-15.0Si-8.0B alloy.

The outcome of the model is in an acceptable accordance with experimental observations of Hasemann et al. [81]. According to Hasemann et al. [81], the microstructure of this alloy contains primary Mo_{SS} solid phase and the presence of the binary eutectic $\text{Mo}_{\text{SS}}\text{-Mo}_5\text{SiB}_2$ and ternary $\text{Mo}_{\text{SS}}\text{-Mo}_5\text{SiB}_2\text{-Mo}_3\text{Si}$ eutectic solids has been verified. Based on their experiments, after the formation of primary solid Mo_{SS} phase, the composition of the melt changes and moves toward the mono-variant binary eutectic valley of $\text{Mo}_{\text{SS}}\text{-Mo}_5\text{SiB}_2$ and by proceed of the solidification process the composition of melt approaches the ternary eutectic composition. When the composition of melt is reached to ternary eutectic, the remaining melt solidifies within the invariant ternary eutectic reaction.

6.3.1.2 Mo-16.4 Si-6.7 B (Alloy 2)

The nominal composition is located within Mo_{SS} primary phase therefore, the emerge of the Mo_{SS} phase is expected at the initial stage of solidification. Figure 6.10 shows that generating the first primary Mo_{SS} solid phase initiates at around 2320 K, which is relatively high in comparison with the considered alloy compositions located in other primary solidification regions. This temperature is pretty close to the melting point of Mo and is the reason of the high temperature formation of primary phase during the solidification of the referred alloy composition. The next arising solid phases, which are combination of $\text{Mo}_5\text{SiB}_2\text{-Mo}_3\text{Si}$, appear at 2270 K, which is relatively wide range of temperature, in comparison with other considered compositions. However, the volume fraction of formed primary and binary eutectic phases are relatively few ($\sim 10\%$). This phenomenon can be explained by the distance of the Mo-16.4Si-6.7B composition from the ternary eutectic point. This composition is located near the ternary eutectic point based on the liquidus projection of Mo-Si-B alloy published by Yang and Chang [78, 79] and therefore, the solidification path toward ternary eutectic

point is quite short and hence, solidification domain is mostly occupied with ternary eutectic $\text{Mo}_{\text{SS}}\text{-Mo}_5\text{SiB}_2\text{-Mo}_3\text{Si}$ composites.

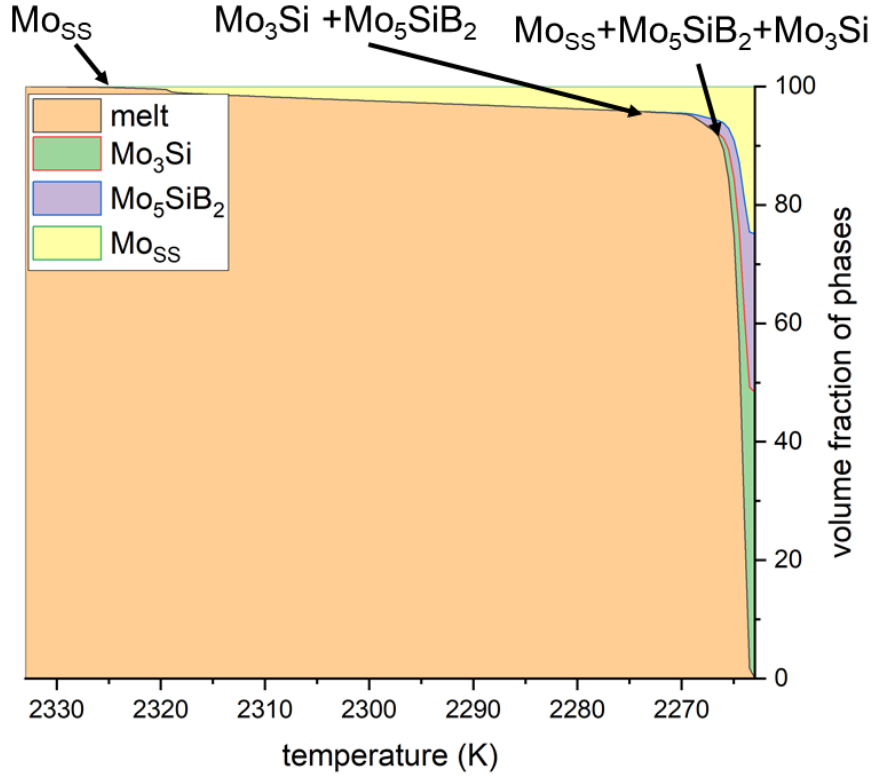


Figure 6.10: Formation sequence and volume fraction of different solid phases during solidification of Mo-16.4Si-6.7B.

Monitoring the composition of the melt during the solidification in correspond to the temperature of the melt which is shown in the figure 6.11 has proved that after the primary formation of Mo_{SS} phase, the composition of the remaining liquid phase changes toward the monovariant eutectic line. Therefore the microstructure evolution of alloy Mo-16.4Si-6.7B proceeds along the mono-variant binary eutectic valley of $\text{Mo}_5\text{SiB}_2\text{-Mo}_3\text{Si}$ and tends to perform the nucleation of both Mo_5SiB_2 and Mo_3Si solid phases in parallel within the melt by decomposition of the melt under reaction of $\text{L} \rightarrow \text{Mo}_5\text{SiB}_2 + \text{Mo}_3\text{Si}$. However, the borderline between the Mo_5SiB_2 and Mo_3Si phases is obviously small based on the considered thermodynamic data published by Yang and Chang [78, 79]. Therefore the solidification path along with $\text{Mo}_5\text{SiB}_2\text{-Mo}_3\text{Si}$ binary eutectic region is quite short. Afterwards, the composition of the melt changes toward the ternary eutectic composition and the remaining melt turns into ternary eutectic composite through $\text{L} \rightarrow \text{Mo}_{\text{SS}} + \text{Mo}_5\text{SiB}_2 + \text{Mo}_3\text{Si}$ reaction. Solidification simulation of alloy with this composition proved the existence of Mo_{SS} as primary forming solid phase through solidification of the melt which was followed by a few amount of binary eutectic growth of $\text{Mo}_5\text{SiB}_2\text{-Mo}_3\text{Si}$ and ternary eutectic growth of $\text{Mo}_{\text{SS}}\text{-Mo}_5\text{SiB}_2\text{-Mo}_3\text{Si}$

which is completely compatible with experimental observations of Hasemann et al. [81]. Although Hasemann et al. [81] have reported the detailed solidification process of the considered alloys, they have not investigated the volume fraction of the solid phases in their work, therefore a direct comparison between volume fraction of the phases predicted by simulations and experiments is not possible. However, comparing the outcome of the model with the available data within the literature has proved the reliability of the developed model.

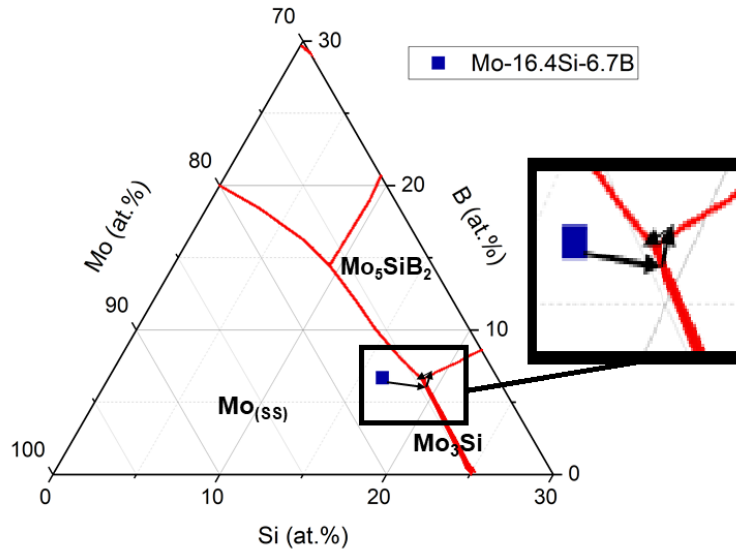


Figure 6.11: solidification path of the alloy Mo-16.4 Si-6.7 B. The composition of the melt was monitored during the solidification and has shown to be changing by formation of the solid phases.

This is crucial to control the validity of the model by controlling the nature of the formed phases. Therefore, the chemical composition of different phases participating in solidification of the alloys located in $Mo_{(ss)}$ primary area were examined through the simulations. Figures 6.12 and 6.13 show the component distribution pattern for the alloy compositions Mo-15.0Si-8.0B and Mo-16.4Si-6.7B respectively. As it is shown in the following figures, the components distribution pattern is compatible with the assumed chemical composition of the phases. Exploring the composition of generated Mo_3Si solid phase within the simulations demonstrated that the participation of the Si content within the solidified Mo_3Si grains is 25 at.% therefore preserves the stoichiometric feature of Mo_3Si phase. Moreover, it is obviously shown that at the interfaces between phases the distribution pattern of the components changes continuously which is in accordance with the diffusive interface considerations of the developed model. The measured quantity of the components is acceptably compatible with the considerations of Yang and Chang [78, 79].

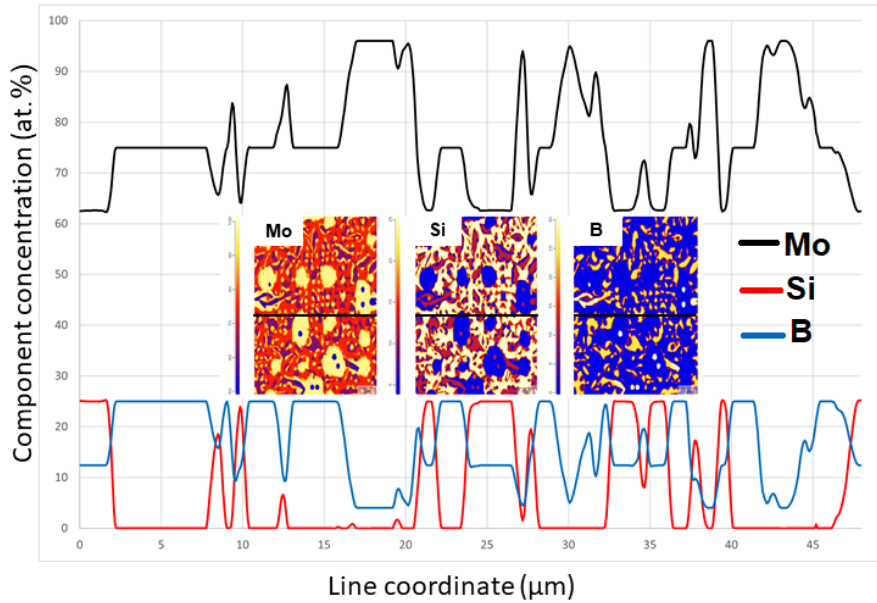


Figure 6.12: Chemical composition of different solid phases formed during solidification of Mo-15.0Si-8.0B. The value of each component along with the illustrated line is presented.

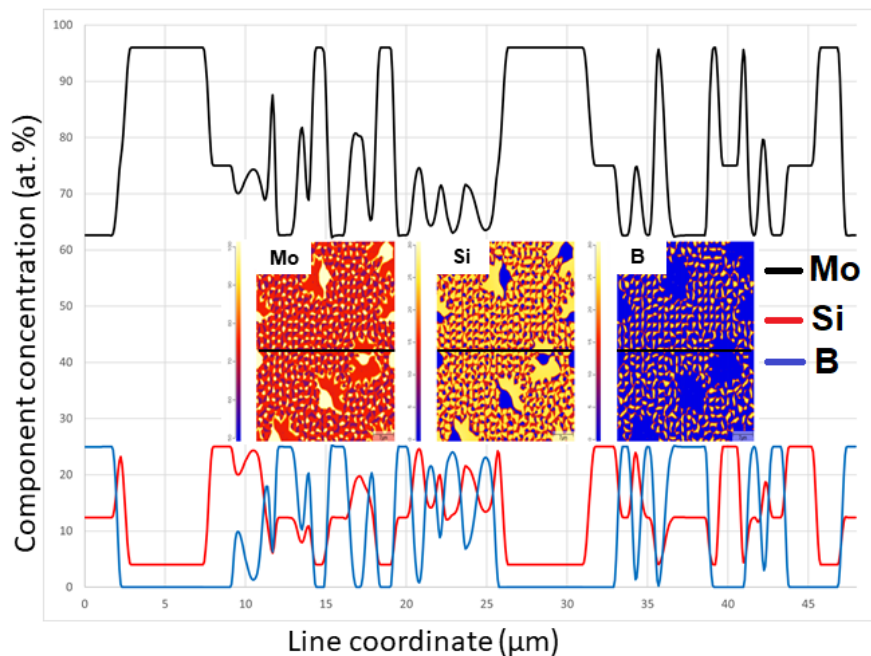


Figure 6.13: Component distribution pattern within the phases formed during solidification of Mo-16.4Si-6.7B alloy and the value of each component along with the illustrated line.

6.3.2 Alloys with Mo_5SiB_2 primary phase

Alloy compositions Mo-15.0Si-10.0B (at.%) and Mo-18.0Si-8.0B (at.%) are located within the Mo_5SiB_2 primary solidification region [78, 79]. According to the literature, [78, 79, 81], the Mo_5SiB_2 primary solidification region is surrounded by the two-phase saturation curves which are; U_1-U_2 , U_2-E_t , E_t-U_4 and U_4-U_3 regions. The U_1 , U_2 , U_3 , U_4 and E_t are the phase transition reactions which are already explained in 2.1. As discussed before, alloys with the compositions located in this region, tend to go through Mo_5SiB_2 primary solidification reaction in which formation of Mo_5SiB_2 solid crystals can be changing the composition of the residual melt so that it moves on the liquidus surface toward the two-phase reaction regions. Therefore, the fraction of formed primary phase is influential on the composition of the melt and consequently the arising binary reaction. Within the simulations, the emerging of the primary phase was observed in which afterwards, depending the alloy composition the nucleation and growth of the other phases during the solidification reactions took place until the solidification process ended up with the ternary eutectic reaction and residual melt turned in to Mo_3Si - Mo_5SiB_2 - Mo_{ss} eutectic composition of solids. Exploring the emerging phases during the solidification and deriving the fraction of formed phases at different temperatures confirms the development of binary and ternary solidification reactions. Alloys which are taken from the Mo_5SiB_2 primary solidification region are listed in figure 6.3.

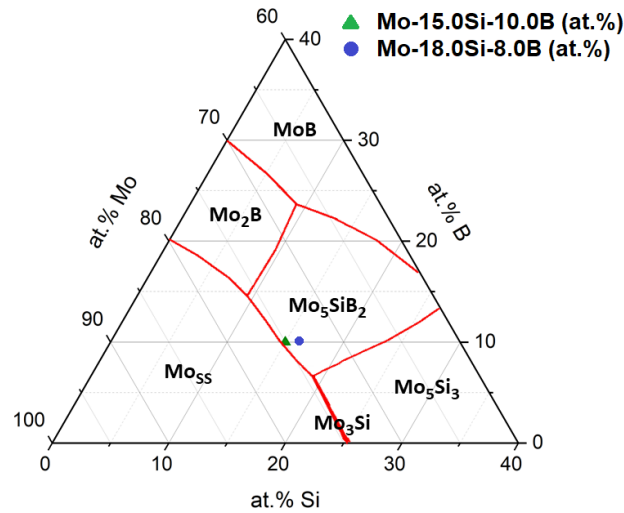


Table 6.3: composition of alloys solidifying with the Mo_5SiB_2 primary phase.

6.3.2.1 Mo-15.0Si-10.0B (Alloy 3)

Simulations have demonstrated that during the solidification of this alloy composition, primary Mo_5SiB_2 crystals will emerge by nucleation and growth of haphazardly distributed Mo_5SiB_2 solid nucleus. As it is shown in the figure 6.14, a limited amount

of primary solids form within the solidification domain which considering the distance between the considered alloy composition and the ternary eutectic point, the limited volume fraction of the primary phase is absolutely comprehensible. Afterwards, by reduction of melt's temperature, the residual melt will form a two-phase $\text{Mo}_{\text{SS}}\text{-Mo}_5\text{SiB}_2$ binary eutectic composite. The parallel growth of the binary $\text{Mo}_{\text{SS}}\text{-Mo}_5\text{SiB}_2$ composite is followed by ternary eutectic phase transition and the rest of melt turns in to $\text{Mo}_{\text{SS}}\text{-Mo}_5\text{SiB}_2\text{-Mo}_3\text{Si}$ solid composite. The sequence of different solidification reactions throughout temperature reduction at the melt is shown in the figure 6.14 for the Mo-15.0Si-10.0B alloy composition.

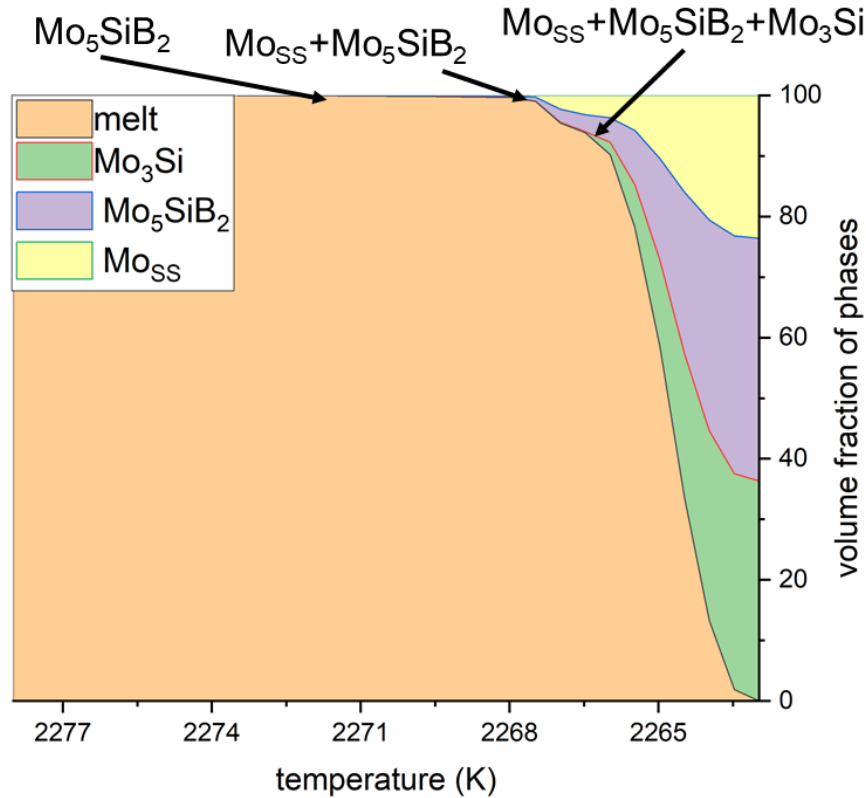


Figure 6.14: sequence of different solidification reactions and the corresponding temperatures during solidification of Mo-15.0Si-10.0B alloy composition.

As the temperature of the system reduces and melt cools down, the liquid composition follows the path of the binary $\text{Mo}_{\text{SS}}\text{-Mo}_5\text{SiB}_2$ valley, where Mo_{SS} phase is formed in parallel to Mo_5SiB_2 by the consumption of the residual liquid phase, via $\text{L} \rightarrow \text{Mo}_{\text{SS}} + \text{Mo}_5\text{SiB}_2$ phase transition reaction. From the simulations, it is observed that the amount of primary phase is very limited. Therefore the sufficient amount of liquid will be remaining to undergo to the binary and ternary eutectic reaction. By reduction of the temperature of the melt, the remaining liquid transforms directly into ternary eutectic composition.

Investigating the chemical composition of the melt during solidification has indicated that during the formation of the primary Mo_5SiB_2 solid phase which is performed by following the $L \rightarrow \text{Mo}_5\text{SiB}_2$ reaction, the composition of the melt changes toward the binary $\text{Mo}_{\text{SS}}\text{-Mo}_5\text{SiB}_2$ eutectic valley where the binary $L \rightarrow \text{Mo}_{\text{SS}} + \text{Mo}_5\text{SiB}_2$ reaction takes place. The solidification path of the Mo-15.0Si-10.0B (at.%) composition alloy is shown in the figure 6.15. The Mo_5SiB_2 is a B rich phase in which formation of the Mo_5SiB_2 primary solid grains will change the Si/B ratio within the melt and shifts the solidification path toward the monovariant $\text{Mo}_{\text{SS}}\text{-Mo}_5\text{SiB}_2$ binary eutectic reaction, where the Mo_{SS} phase grows joint with Mo_5SiB_2 . The Mo_{SS} phase contains a limited amount of Si which changes the Si/B balance in the melt in the opposite approach of Mo_5SiB_2 solid phase. The chemical composition of the melt moves along with the binary eutectic line toward the ternary eutectic point, where the remaining liquid transforms directly into ternary eutectic composite within $L \rightarrow \text{Mo}_{\text{SS}} + \text{Mo}_5\text{SiB}_2 + \text{Mo}_3\text{Si}$ invariant ternary eutectic reaction. According to the experi-

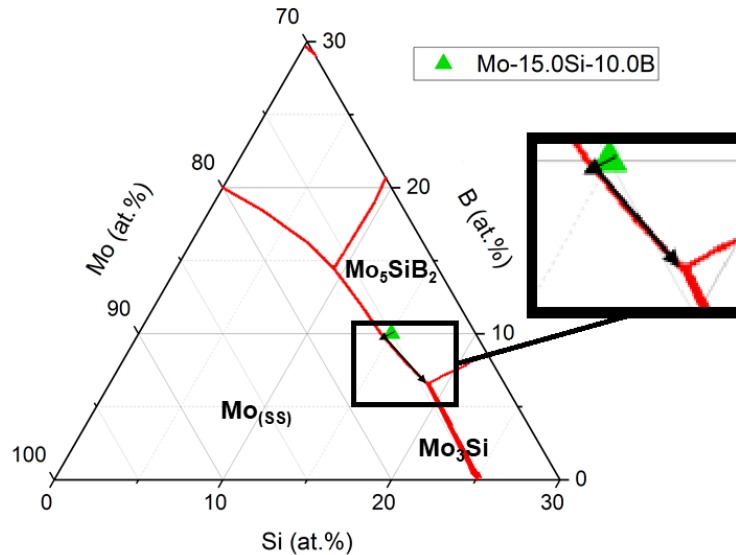


Figure 6.15: Schematic of the solidification path of Mo-15.0Si-10.0B alloy composition achieved through the simulations.

mental observations of Hasemann et al. [81], after the primary Mo_5SiB_2 crystal has formed, the alloy proceeds to solidify via the two-phase mono-variant $\text{Mo}_{\text{SS}}\text{-Mo}_5\text{SiB}_2$ eutectic and a ternary eutectic of $\text{Mo}_{\text{SS}}\text{-Mo}_5\text{SiB}_2\text{-Mo}_3\text{Si}$. Considering the solidification path achieved by the simulations, the outcome of the model for simulation the solidification of the Mo-15.0Si-8.0B alloy is acceptably compatible with experimental observation of Hasemann et al. [81].

6.3.2.2 Mo-18.0Si-8.0B (Alloy 4)

The nominal composition lies within the primary Mo_5SiB_2 phase region, which confirms Mo_5SiB_2 as primary phase formed from the liquid phase. According to the results

of the simulation which is shown in the figure 6.16, the volume fraction of the primary solid phase is very limited. This phenomena is caused by the composition of this alloy which is close to the binary reaction borderline as well as the ternary eutectic point based on [78, 79] and leads to the formation of the limited amount of primary solid phase according to the lever rule. Therefore, adequate amount of melt will remain within the solidification domain so that the binary phase transition reaction will be performed. After primary formation of the Mo_5SiB_2 phase, a parallel formation and growth of Mo_5SiB_2 and Mo_3Si solids was observed during the simulations. After formation of the binary $\text{Mo}_5\text{SiB}_2\text{-Mo}_3\text{Si}$ composite, the residual melt turns into ternary eutectic $\text{Mo}_{\text{SS}}\text{-Mo}_5\text{SiB}_2\text{-Mo}_3\text{Si}$ composite.

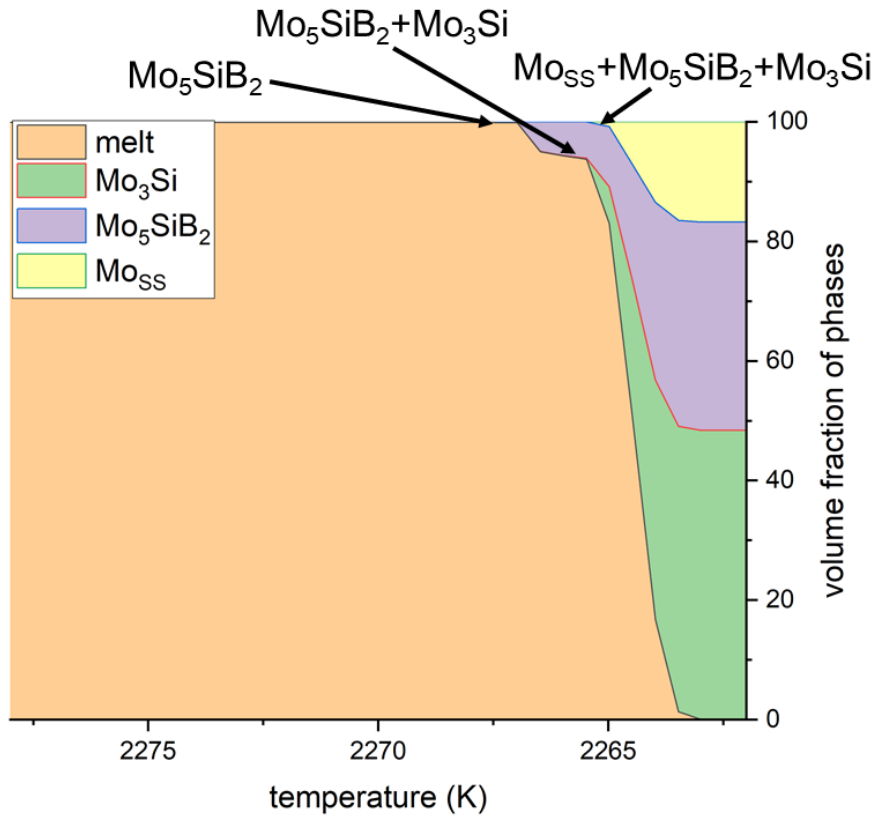


Figure 6.16: Portion of the volume of different rising solid phases within solidification process of Alloys with Mo-18Si-8B composition

By examining the chemical composition of the melt and determining the direction of the changes in the composition, the properties of the phase transitions reactions during the solidification of the Mo-18.0Si-8.0B (at. %) has been investigated. According to the outcome of the simulation which is shown in the figure 6.17, the first arising phase transition which was the consequence of the formation of the primary phase is through $L \rightarrow \text{Mo}_5\text{SiB}_2$ reaction. It has been confirmed that the formation of Mo_5SiB_2 primary phase changes the composition of the liquid phase toward binary $\text{Mo}_5\text{SiB}_2\text{-Mo}_3\text{Si}$ monovariant reaction region. In which the formation of Mo_3Si phase takes

place and the Mo_3Si phase is formed through a cooperative growth with Mo_5SiB_2 phase within $\text{L} \rightarrow \text{Mo}_5\text{SiB}_2 + \text{Mo}_3\text{Si}$ phase transition reaction. Formation and growth of the binary Mo_5SiB_2 - Mo_3Si composite changes the chemical composition of the melt toward the ternary eutectic reaction. Therefore, The solidification will continue along the binary borderline to the ternary eutectic point where the four-phase invariant reaction $\text{L} \rightarrow \text{Mo}_5\text{SiB}_2 + \text{Mo}_3\text{Si} + \text{Mo}_{\text{ss}}$ takes place and the residual melt turn into ternary eutectic $\text{Mo}_5\text{SiB}_2 + \text{Mo}_3\text{Si} + \text{Mo}_{\text{ss}}$ composite.

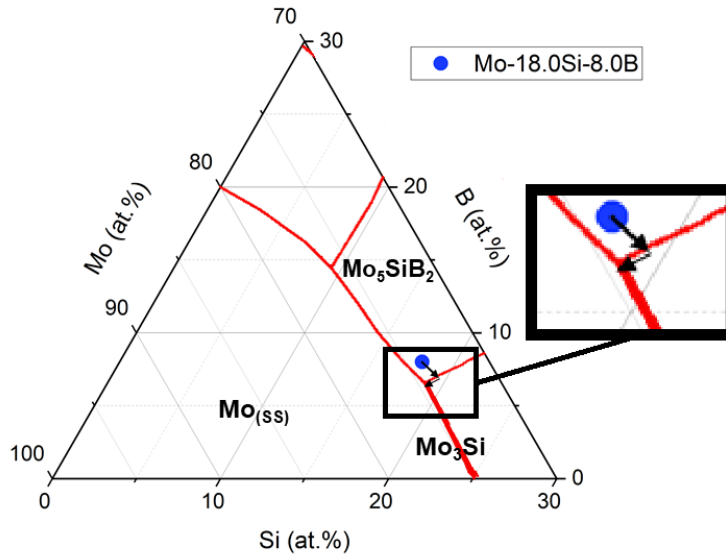


Figure 6.17: solidification path of the alloy Mo-18 Si-8 B. At the beginning of solidification the composition of the melt contains 18 at.% Si and 8.0 at.% B. However, by proceeding of the solidification the chemical composition of the melt changes and moves toward Mo_5SiB_2 - Mo_3Si eutectic valley. The solidification proceed until the composition of the melt reaches the ternary eutectic composition.

The experimental investigations of Hasemann et al. [81] has revealed that during the solidification of Mo-18.0Si-8.0B (at.%) alloy composition, the presence of the Mo_5SiB_2 , Mo_3Si and Mo_{ss} solid phases was confirmed. Besides formation of Mo_5SiB_2 primary solids and ternary eutectic composites, they have reported the presence of Mo_5SiB_2 - Mo_3Si binary eutectic regions within the solidified alloy which implies the accuracy of the developed model in predicting the binary eutectic reaction.

After probing the solidification path of the considered alloys, a careful investigation of the composition of the formed phases during the solidification has been performed to investigate the component distribution pattern within the solid phases and consequently to control the nature of the predicted phases within the model which is shown in the figure 6.18 and 6.19. It has been confirmed that there is an acceptable compatibility between the measurement of simulations and the chemical composition of the

considered phases. Therefore it can be concluded that the developed model predicts the solidification behavior of the alloy composition located in the Mo_5SiB_2 primary region very precisely.

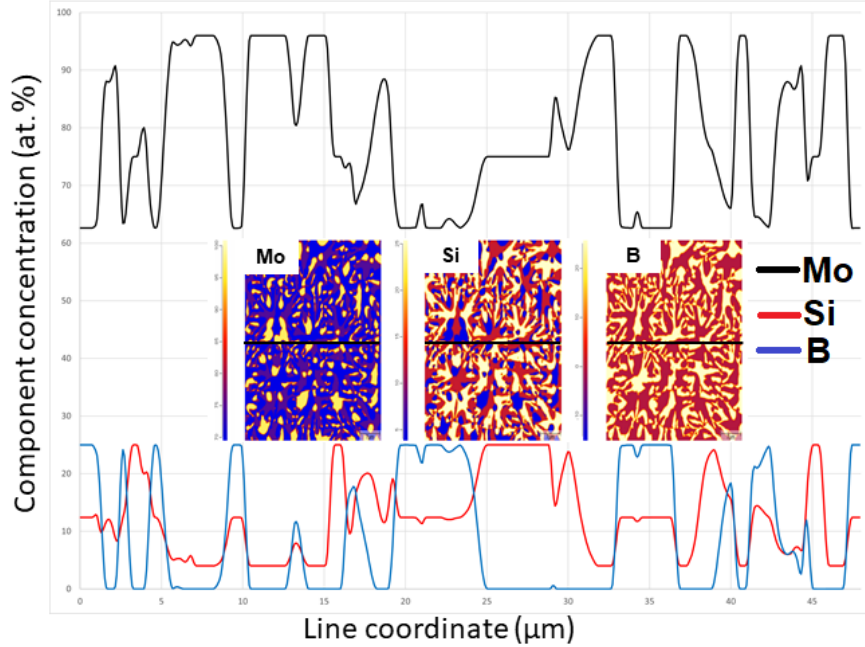


Figure 6.18: Distribution pattern of different elements among the solid phases within Mo-15.0Si-10.0B alloy and along with the illustrated line.

6.3.3 Alloys with Mo_3Si primary phase

The outcome of the model for simulating the solidification behavior of the alloys with Mo_3Si primary solidification phase is discussed in this section. According to the published data within the literature [78, 79, 81] the primary Mo_3Si region is surrounded by $\text{Mo}_{5\text{Si}}$, Mo_5SiB_2 and Mo_5Si_3 regions in which, depending to the alloy composition and operational condition, every composition from Mo_3Si region may perform a binary solidification reaction with the referred phases during solidification. Therefore, it is very important for validating the reliability of the model to achieve the precise prediction of the solidification path. Validating the accuracy of the solidification simulation of the alloys located within this region turned out to be very challenging. According to the thermodynamic calculations of Yang and Chang [78, 79], the Mo_3Si primary region is relatively small, in comparison to other primary solidification areas. Therefore the number of the alloy compositions which perform the Mo_3Si primary solidification is very limited. Besides, the experimental investigations of Hasemann et al. [81] which are the reference of the present study for controlling the validity of the developed model has reported a different Mo_3Si solidification region. However, the Mo-20.5Si-5.0B (at.%) and Mo-20.2Si-5.8 (at.%) compositions were considered to be applied in the simulations because these alloy compositions are supposed to have

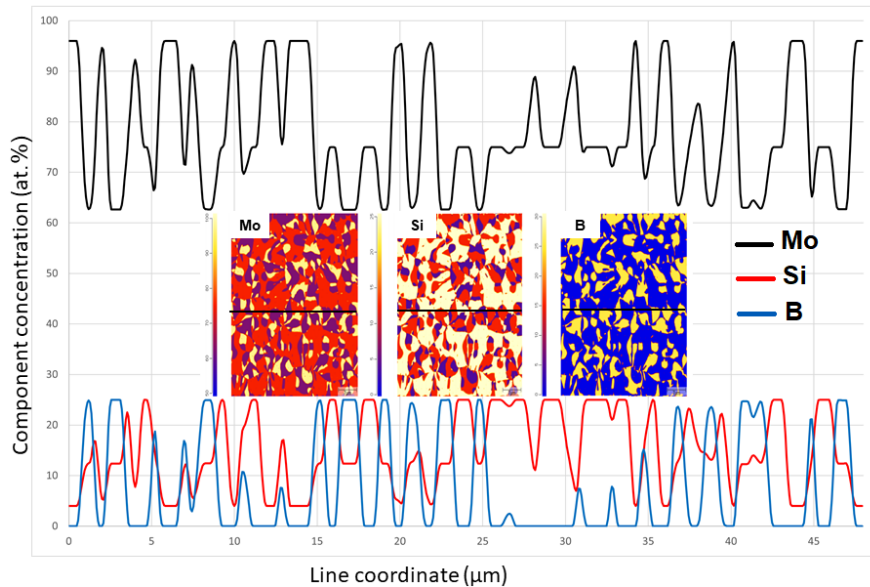


Figure 6.19: Pattern of distribution of the elements among the phases within solidified Mo-18 Si-8 B alloy, the amount of every component is demonstrated along with the illustrated line.

similar solidification behavior based on the both Yang and Chang' calculations [78, 79] and Hasemann et al.'s experiments [81]. Therefore, it is possible to validate the accuracy of the outcome of the model with experimental observation of Hasemann et. al [81]. Figure 6.20 shows the considered alloy compositions within the Mo-Si-B phase diagram based on the calculations of Yang and Chang [78, 79].

6.3.3.1 Mo-20.4 Si-5.0 B (Alloy 5)

This particular composition is located in Mo_3Si area, based on [81] as well as Yang and Chang [78, 79]. Therefore formation of the primary Mo_3Si solid dendrites is expected to be arising as primary solidifying phase. According to the simulations, the first primary Mo_3Si grains was formed at around 2275 K. Afterwards, as it is shown in the figure 6.22, the solidification of the Mo-20.4Si-5.0B (at.%) composition is followed by cooperative growth of Mo_5SiB_2 and Mo_3Si phases which initiates at around 2266 K. The evolution of Mo_5SiB_2 - Mo_3Si composition continued to 2264 K where the ternary Mo_{55} - Mo_5SiB_2 - Mo_3Si composite was formed within the melt and residual melt hast turned to ternary eutectic composite. The volume fraction of the binary Mo_5SiB_2 - Mo_3Si composite was relatively low ($\sim 3\%$) based on the outcome of the model. The temperature difference between the binary and ternary reactions is relatively low, therefore the binary Mo_5SiB_2 - Mo_3Si formations continuous for a quite short time.

In accordance with the solidification evolution of the alloy composition Mo-20.4Si-5.0B (at.%), investigating the chemical composition of the melt during the solidification process has revealed that formation of primary Mo_3Si solid phase from the $L \rightarrow$

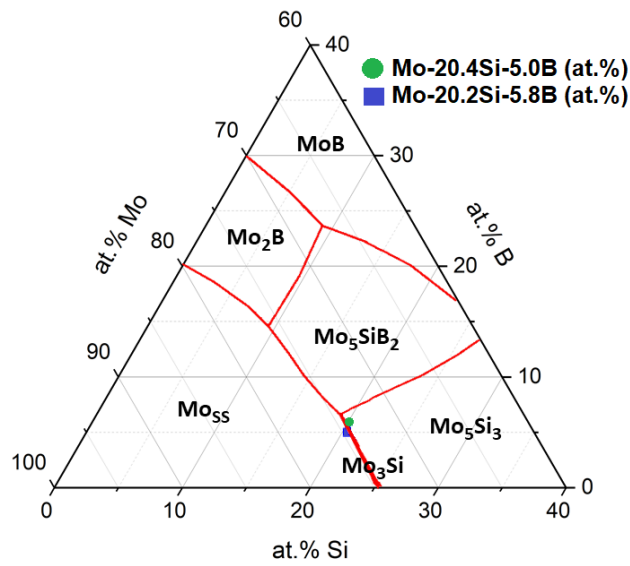


Figure 6.20: Considered alloy compositions within the Mo₃Si primary solidification area

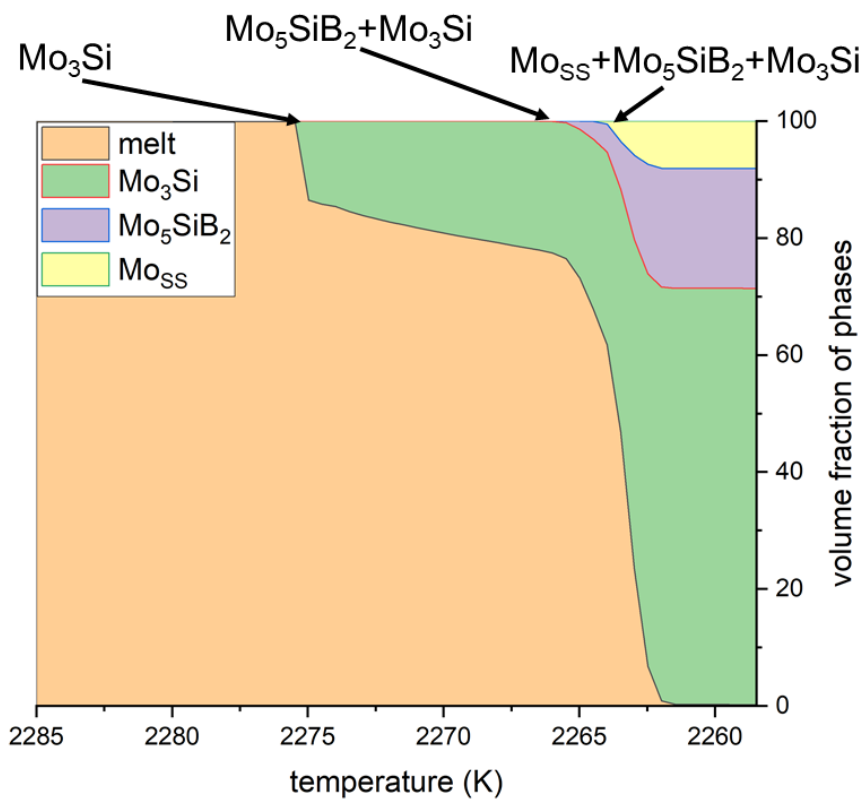


Figure 6.21: Formation sequence of different solid phases during the solidification simulation of Mo-20.4Si-5.0B (at.%) alloy.

Mo_3Si reaction changes the chemical composition within the melt toward the binary Mo_5SiB_2 - Mo_3Si eutectic region. Therefore it can be concluded that cooperative formation of Mo_5SiB_2 and Mo_3Si phases observed during the solidification comes from $L \rightarrow \text{Mo}_5\text{SiB}_2 + \text{Mo}_3\text{Si}$ binary eutectic reaction. By proceeding the binary eutectic reaction the chemical composition of the melt changes toward the ternary eutectic point where the residual melt undergoes the invariant ternary eutectic reaction $L \rightarrow \text{Mo}_{\text{SS}} + \text{Mo}_5\text{SiB}_2 + \text{Mo}_3\text{Si}$. The solidification path of the Mo-20.4Si-5.0B (at.%) composition alloy is shown in the figure 6.22. As it is discussed before, the volume fraction of binary eutectic Mo_5SiB_2 - Mo_3Si phase is quite few which may be because of few temperature difference between the binary eutectic reaction's temperature and the ternary eutectic reaction temperature. However, exploring the solidification path of the referred composition has revealed that besides the short temperature difference between the two following reactions, the low volume fraction of the binary Mo_5SiB_2 - Mo_3Si could be because of the very short Mo_5SiB_2 - Mo_3Si region considered within the thermodynamic data of Yang and Chang [78, 79].

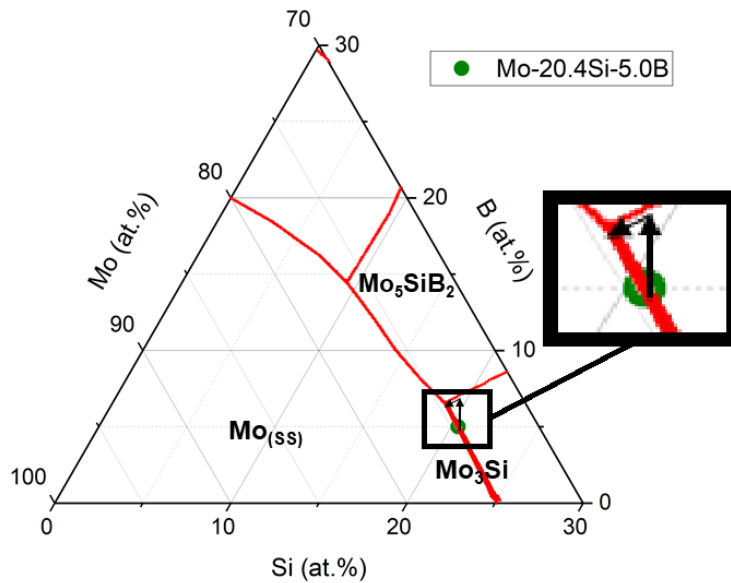


Figure 6.22: Solidification path of the Mo-20.4Si-5.0B (at.%) composition based on the outcome of the simulations.

The solidification behavior of the Mo-20.4Si-5.0B (at.%) composition predicted through the simulations is in an acceptable accordance with the experimental observations of Hasemann et al. [81]. According to their experiments, after the primary Mo_3Si dendrites have formed the solidification proceeds via a two-phase Mo_5SiB_2 - Mo_3Si eutectic. The remaining melt undergoes the ternary eutectic reaction during solidification of the referred alloy composition.

6.3.3.2 Mo-20.2 Si-5.8 B (Alloy 6)

The sequence of formation different solid phases during the solidification simulation of the Mo-20.2Si-5.8B (at.%) composition is shown in the figure 6.23. This composition lies within the Mo_3Si single-phase region, which based on the simulations forms primarily at the initial steps of solidification at around 2274 K. The primary solidification is followed by formation of the Mo_5SiB_2 - Mo_3Si composite which begins at around 2270 K. In comparison to the alloy composition Mo-20.4Si-5.0B (at.%), there was fewer amount of primary phase observed during the simulations which can be explained by considering the distance of two considered compositions with the ternary eutectic point. This alloy is closer to the ternary eutectic point in comparison to the alloy composition Mo-20.4Si-5.0B (at.%), therefore formation of more primary solid phase is absolutely comprehensible. Cooperative growth of Mo_5SiB_2 and Mo_3Si solid phases continues to 2264 K when the remaining melt turns into Mo_5SiB_2 - Mo_3Si - Mo_{SS} ternary eutectic composite.

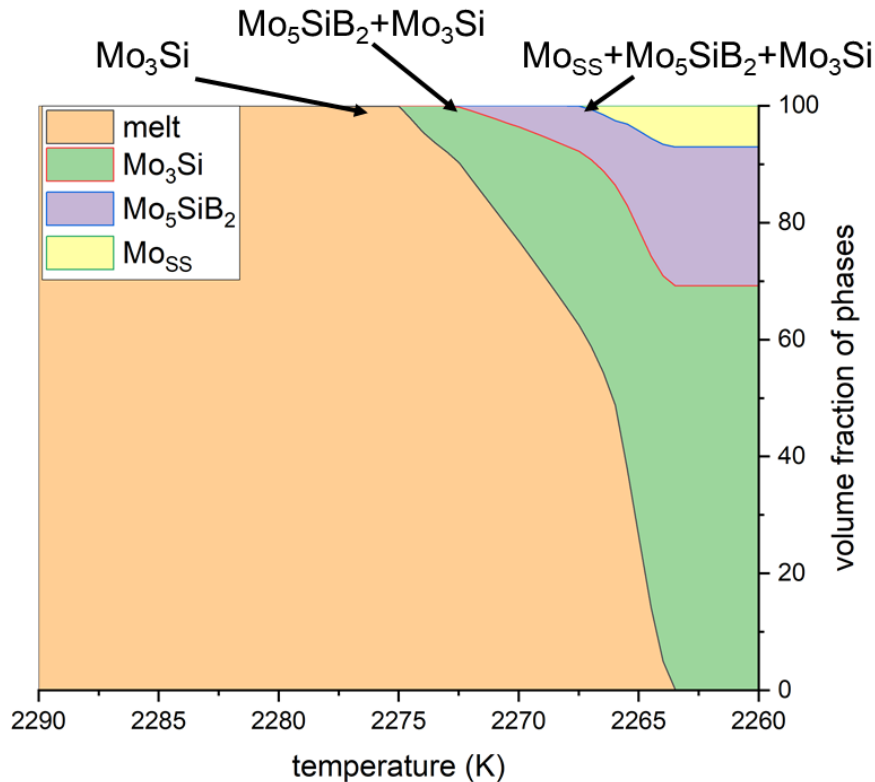


Figure 6.23: Solidification process of Mo-20.2Si-5.8B (at.%) based on the outcome of the simulations.

Investigating the chemical composition of the melt during the solidification has revealed that formation of the primary phase from the liquid phase through the $L \rightarrow \text{Mo}_3\text{Si}$ phase transition reaction changes the mixture of the melt toward the binary

eutectic $\text{Mo}_5\text{SiB}_2\text{-Mo}_3\text{Si}$ valley, where the Mo_5SiB_2 phase is formed within a monovariant binary eutectic reaction by the consumption of the liquid phase, via $\text{L} \rightarrow \text{Mo}_5\text{SiB}_2 + \text{Mo}_3\text{Si}$ phase transition reaction. As it is expected from the thermodynamic calculations, similarly to the alloy Mo-20.4Si-5.8B (at.%), the refereed alloy composition proceeds across the binary eutectic line until it reaches the ternary eutectic point. The residual melt undergoes invariant ternary eutectic reaction $\text{L} \rightarrow \text{Mo}_{\text{SS}} + \text{Mo}_5\text{SiB}_2 + \text{Mo}_3\text{Si}$ and forms the ternary eutectic composite. The solidification path of the Mo-20.2Si-5.8B (at.%) composition is shown in the figure 6.24. To evaluate the performance of the developed model in predicting the solidification behavior of the nominal alloy composition, the sequence of phase transition reactions across the temperature reduction has been compared with the outcome of Hasemann et al. [81] work. Their achievements have confirmed the absolute accuracy of the model's prediction of the solidification behavior of the Mo-20.2Si-5.8B (at.%) composition.

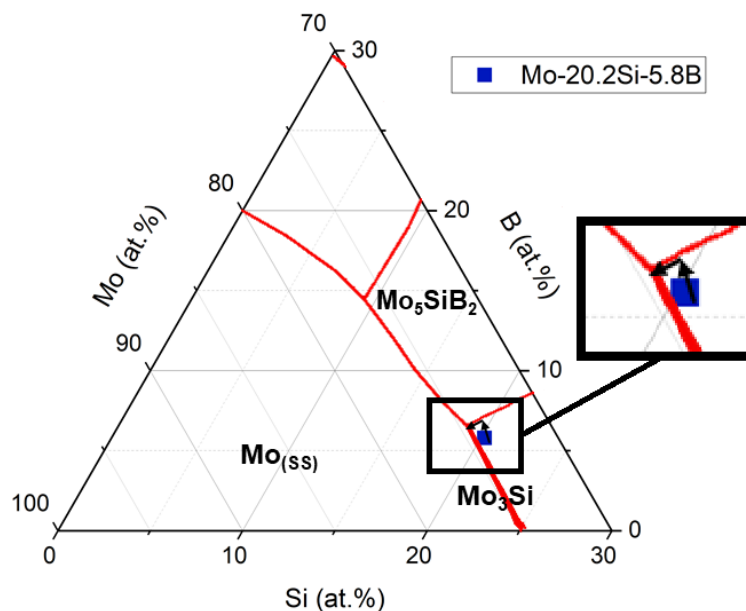


Figure 6.24: Solidification path of Mo-20.2Si-5.8B . By nucleation and growth of solid primary Mo_3Si phase, composition of the melt moves toward binary $\text{Mo}_5\text{SiB}_2\text{-Mo}_3\text{Si}$ eutectic valley. As the solidification proceeds, the composition goes toward ternary eutectic point. The process end by turning the residual melt into ternary eutectic composition.

Chemical composition of solid phases generated through solidification of alloy compositions with Mo_3Si primary phase was examined to control the nature of the generated phases and are shown in the figures 6.25 and refelements-20-25-8. Investigating the chemical composition of the generated phases during the solidification has proved the stoichiometric feature of the Mo_3Si phase by demonstrating the Si content of this phase to be equal to 25 at.%. Although it has been observed during the experiments

that Mo_3Si phase contains around 24.1 at.% of Si, but it is assumed to be an absolute stoichiometric phase containing 25 at.% of Si within thermodynamic calculations of Yang and Chang [78, 79]. Therefore the outcome of the developed model is completely compatible with the thermodynamic assumptions.

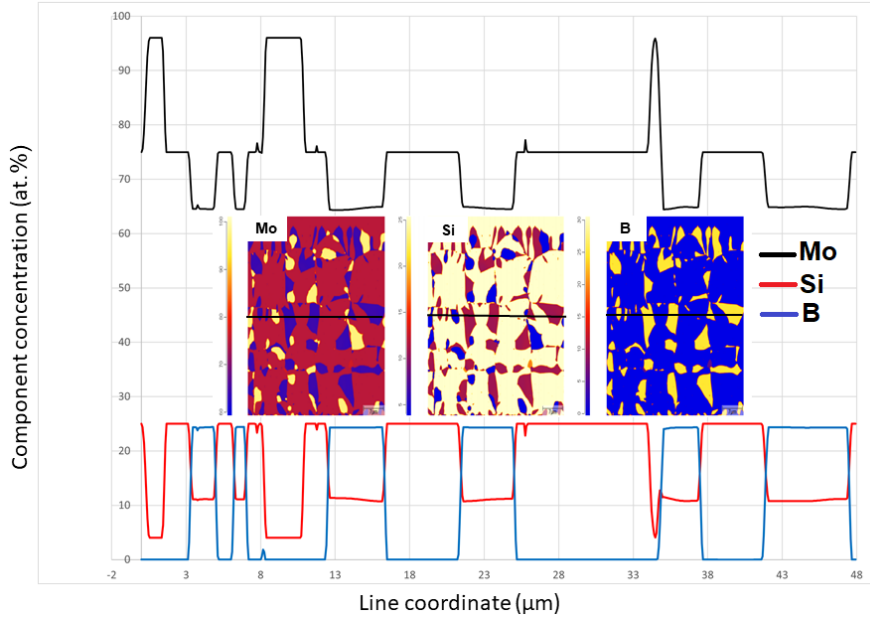


Figure 6.25: Distribution of the constituents within solid phases of alloy Mo-20.4Si-5.0B and along with the illustrated line.

As an outcome of this research, investigation of the Mo_3Si phase, particularly the distribution pattern of the elements inside the predicted phases are in very good agreement with the binary Mo-Si phase diagram [58] and confirm the stoichiometric composition of the intermetallic Mo_3Si phase.

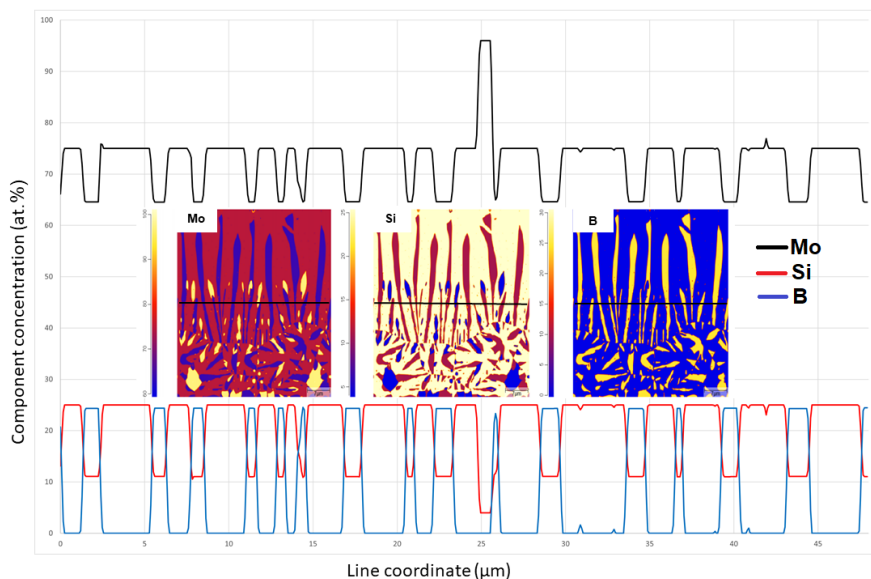


Figure 6.26: Distribution pattern of components inside the solid phases within alloy Mo-20.2Si-5.8B as well as along with the illustrated line.

6.4 Microstructure evolution of considered compositions

Microstructure evolution of the considered alloy compositions during the solidification based on the outcome of the model are represented in the following sections and are compared with the available data from experiments of Hasemann et al. [81] and the differences between simulation results and experimental observations are discussed comprehensively.

6.4.1 Alloys with Mo_{55} primary phase

The microstructure of the compositions Mo-15.0Si-8.0B (at.%) and Mo-16.4Si-6.7B (at.%) based on the simulations performed in the framework of present thesis and experiments of Hasemann et al. [81] are shown in the figure 6.27. As it is demonstrated in the picture, the both referred alloys tend to form relatively large primary Mo_{55} dendrites. According to the phase transition investigation which has been discussed in the section 6.3.1, After the formation of the primary Mo_{55} , the microstructure evolution of alloy Mo-15.0Si-8.0B (at.%) continues along the mono-variant binary eutectic valley of Mo_{55} - Mo_5SiB_2 and the residual melt solidifies within the invariant ternary eutectic reaction of Mo_{55} - Mo_5SiB_2 - Mo_3Si in which the binary and ternary regions can be detected from the microstructure. Regarding to the Mo-15.0Si-8.0B (at.%) alloy composition, there is an acceptable agreement between the microstructure achieved within simulations and experiments [81]. However, the Mo-16.4Si-6.7B (at.%) composition tends to perform a Mo_5SiB_2 - Mo_3Si binary eutectic reaction after formation of the primary Mo_{55} solid phase. The binary Mo_5SiB_2 - Mo_3Si region was observed clearly within the both simulations and experiments [81] and are marked within the

picture. After formation of the binary eutectic composite, the residual melt with turn into ternary $\text{Mo}_{55}\text{-Mo}_5\text{SiB}_2\text{-Mo}_3\text{Si}$ composite.

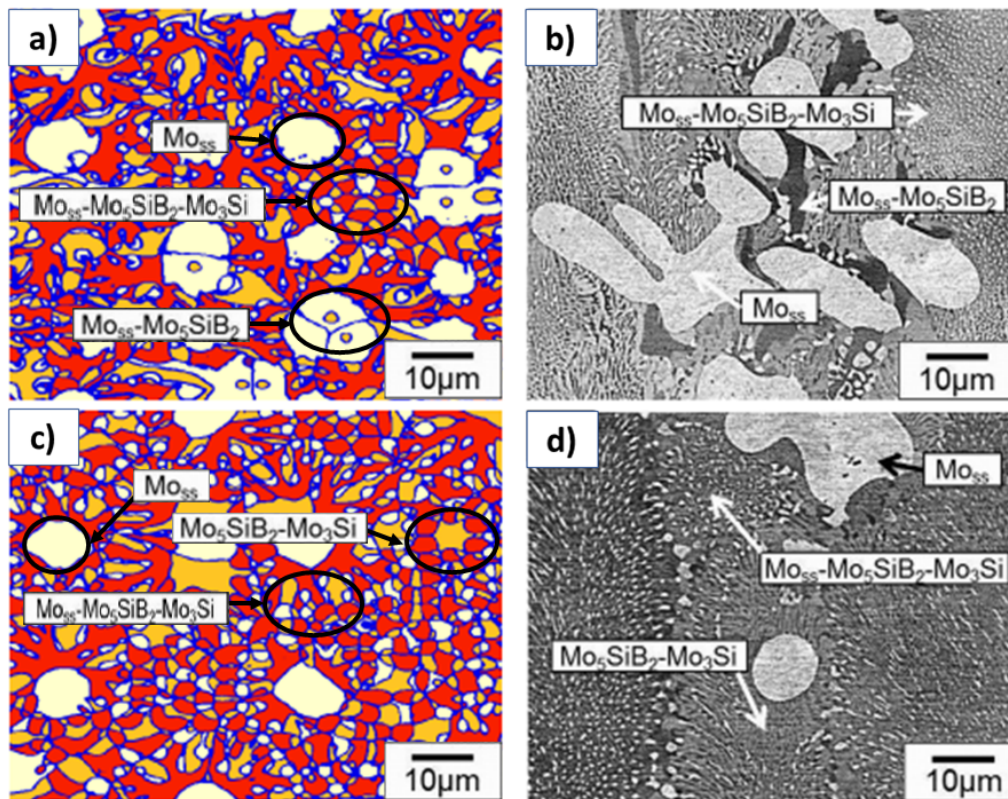


Figure 6.27: Microstructure of the Mo-15.0Si-8.0B (at.%) composition a) achieved by simulations b) observed in the experiments of Hasemann et al. [81] and Mo-16.4Si-6.7B (at.%) composition c) based on the simulations d) experiments of Hasemann et al. [81].

6.4.2 Alloys with Mo_5SiB_2 primary phase

The microstructure of the alloy compositions Mo-15.0Si-10.0B (at.%) and Mo-16.9Si-7.4B (at.%) predicted within the simulations and observed by Hasemann et al. [81] is represented in the figure 6.28. As this is already discussed in the section 6.3.2, after formation of the primary Mo_5SiB_2 crystal, the alloy composition Mo-15.0Si-8.0B (at.%) proceeds to solidify via the two-phase mono-variant $\text{Mo}_{55}\text{-Mo}_5\text{SiB}_2$ eutectic and the solidification process finishes by formation of the ternary eutectic $\text{Mo}_{55}\text{-Mo}_5\text{SiB}_2\text{-Mo}_3\text{Si}$ composite. The binary eutectic and ternary eutectic regions are clearly visible within the outcome of the simulations (a) and experiments (b) [81]. However, comparing to the simulation results, the primary regions predicted by Hasemann et al. [81] is relatively bigger and more coarse. The difference between the microstructure predicted by simulations and observed within the experiments [81] can be explained based on two major concepts. First, it should be considered that the simulations are performed in 2D. Therefore, some visual differences are expected based on the reasons that have

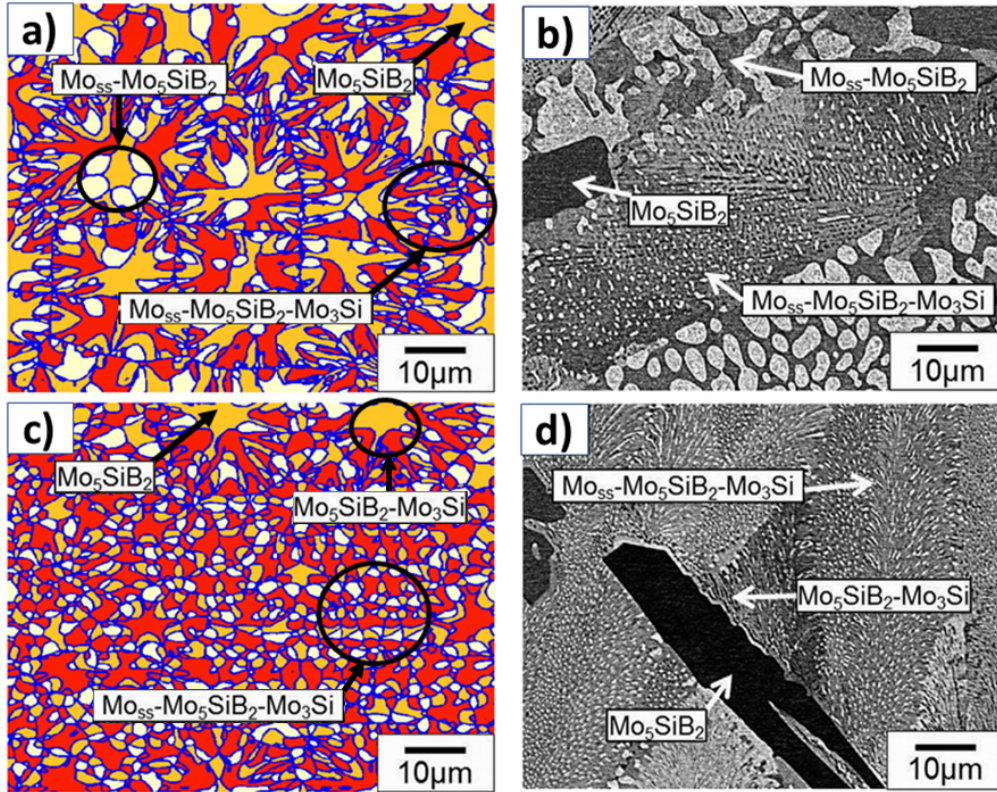


Figure 6.28: Microstructure of the Mo-15.0Si-10.0B (at.%) composition a) achieved by simulations b) observed in the experiments of Hasemann et al. [81] and Mo-18.0Si-8.0B (at.%) composition c) based on the simulations d) experiments of Hasemann et al. [81].

been discussed in the section 6.1.1. Moreover, as it is mentioned before, the liquidus projection of the Mo-Si-B system published by Hasemann et al. [81] is slightly different with the liquidus projection that is considered in the simulations. Therefore, some few differences between the morphology of the alloy compositions predicted by simulations and observed in the experiments [81] is anticipated. The difference between the two categories of microstructures becomes more obvious in the case of the Mo-16.9Si-7.4B (at.%) composition. However, as it is shown in the figure 6.28, comparing the microstructure of the Mo-16.9Si-7.4B (at.%) composition based on the simulations (c) and experiments (d) reveals that the $\text{Mo}_5\text{SiB}_2\text{-Mo}_3\text{Si}$ two-phase region and $\text{Mo}_{55}\text{-Mo}_5\text{SiB}_2\text{-Mo}_3\text{Si}$ three-phase regions are observed within the microstructure.

6.4.3 Alloys with Mo_3Si primary phase

Several alloy compositions from the Mo_3Si primary region have been investigated experimentally by Hasemann et al. [81] and among them Mo-20.4Si-5.0B (at.%) and Mo-20.2Si-5.8B (at.%) compositions were selected to investigate their solidification behavior within the developed model. However, microstructure of Mo-20.2Si-5.8B (at.%) has not been reported within the published data. Therefore, a direct compari-

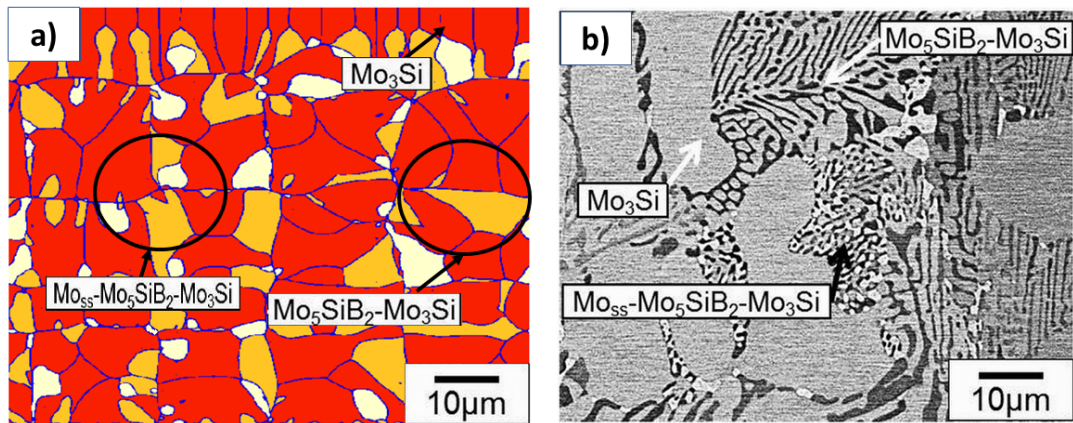


Figure 6.29: Microstructure of the Mo-20.4Si-5.0B (at.%) composition a) achieved by simulations b) observed in the experiments of Hasemann et al. [81].

son between the microstructure of this composition achieved through simulations with the real microstructure is not possible. However, the microstructure of the Mo-20.4Si-5.0B (at.%) composition is represented in the figure 6.29. According to solidification path of the alloy composition Mo-20.4Si-5.0B (at.%) discussed in the section 6.3.3 the microstructure evolution of the this alloy composition tends to solidify via a binary $\text{Mo}_5\text{SiB}_2\text{-Mo}_3\text{Si}$ eutectic reaction after formation of the primary Mo_3Si dendrites. The solidification proceeds to the ternary eutectic reaction and the remaining melt undergoes the ternary eutectic reaction. Therefore, the two-phase $\text{Mo}_5\text{SiB}_2\text{-Mo}_3\text{Si}$ region and three-phase $\text{Mo}_{\text{SS}}\text{-Mo}_5\text{SiB}_2\text{-Mo}_3\text{Si}$ region are expected to present within the microstructure which are clearly seen within both the simulations (figure 6.3.3-a) and experiments of Hasemann et al. [81] (figure 6.3.3-b). Therefore it can be concluded that there is an acceptable agreement between the microstructure of the Mo-20.4Si-5.0B (at.%) composition predicted by the developed model and the experiments.

6.5 Discussion

The solidification path of the considered compositions based on the outcome of the developed model is in agreement with experimental investigations by Hasemann et al. [81] and corroborates their solidification reaction sequence. Therefore, the developed model is undoubtedly reliable to predict the solidification behavior of the the considered alloy compositions. The considered compositions have different primary solidifying phase which include the entire primary regions of “Berczik triangle” within the Mo-rich region of Mo-Si-B system. Therefore, it can be concluded that the model is capable to predict the solidification behavior of the Mo-rich Mo-Si-B alloys and consequently can be very useful tool for devising new Mo-Si-B materials particularly for high temperature applications. However, there are some uncertainties within the microstructure of the compositions predicted by simulations. In particular, within the microstructure of the alloy composition Mo-16.9Si-7.4B (at.%) a large primary Mo_5SiB_2 crystal was observed within the experiments of Hasemann et al. [81]. As it is discussed before it might be because of performing the simulations within 2D domain. Alternatively, this discrepancy between simulation and experiments can be because of the slightly larger Mo_5SiB_2 primary region within the Hasemann’s proposed liquidus projection[81]. In order to explain the impact of the dimension of primary region on the phase distribution pattern, applying the rule of lever on a binary eutectic system should serve as an example.

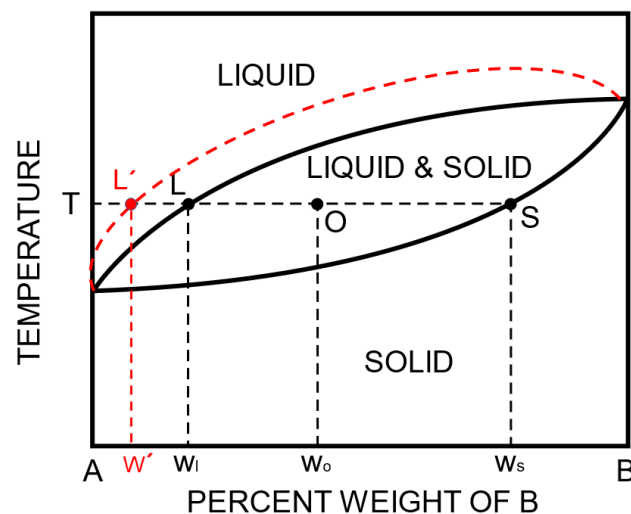


Figure 6.30: A phase diagram with tie lines for small solidification region (LS) and a bigger solidification region (L’S) for a binary system.

The lever rule is a method to determine the mole fraction or mass fraction of the constituent phases within a binary equilibrium phase diagram. Applying the lever rule, the fraction of liquid phase and solid phases for a distinct composition and temperature can be determined. In order to calculate the mass fraction of the constituent phases, in

the example of figure 6.30 solid and liquid at the temperature T for a given composition of W_o , a tie line should be drawn on the phase diagram. This tie line is drawn horizontally at the composition's temperature from the liquid to the solid. The mass fraction of component B at the liquidus of the diagram with smaller primary phase region (shown in black) is given by W_l in diagram and at the liquidus of the diagram with larger primary phase region (shown in red) is given by W' . Moreover, the mass fraction of component B at the solidus is given by W_s in the diagram. According to the lever rule by considering the smaller primary region, the the mass fraction of solid phase (ω_s) can then be calculated using the following equations:

$$\omega_s = \frac{W_o - W_l}{W_s - W_l} \quad (6.1)$$

and by considering the larger primary region is expressed by:

$$\omega_s = \frac{W_o - W'}{W_s - W_l} \quad (6.2)$$

Comparing the equation 6.1 and 6.2 indicates that for given composition W_o , more primary phase would be formed based on the larger liquidus region. Therefore, this is absolutely comprehensible that larger primary phase is observed within the experiments, as compared to the simulations. Having a direct comparison between the exact amount of the predicted primary phase predicted within the simulations and observed in the experiments can shed more light on the effect of the different primary regions on the volume fraction of the primary phase however, since such an information is not available within the published data this comparison is not possible.

7 Summary and Conclusion

Since Mo-Si-B alloys are potential candidates for being applied as structural materials in gas turbines or aircraft engines, it has been tried to develop a phase-field model to simulate the solidification behavior of different Mo-Si-B alloys. Mo-Si-B alloy system is a heterogeneous system including different phases with wide range of mechanical properties. The Mo-rich alloys were specific focus of the present PhD work because they provide both the high temperature and low temperature desired properties. Solidification process plays an important role in Mo-Si-B alloy preparation and although extensive works have been performed to study the Mo-Si-B system experimentally, this system is not well studied numerically and in particular, from the aspect of computational materials science, a comprehensive modeling of solidification process for this alloy system is still missing. The microstructure of the alloys has a significant impact on the properties of the corresponding alloys, therefore having a deep sight of the microstructure evolution during the solidification process is crucial for proper design of materials. Since having a deep sight of Mo-rich Mo-Si-B system's behavior inclusively the solidification behavior is necessary for devising a proper alloy for high temperature industries, the lack of numerical investigation of the nominated system provided sufficient motivation for conducting this research and developing a model based on phase-field method to study the solidification behavior of specifically Mo-rich Mo-Si-B alloy compositions. With the model developed in the framework of present thesis, it has been proved shown that it is possible to simulate the directional solidification of ternary eutectic microstructures as well as the alloys which conduct a primary solidification phase development within Mo-rich region of the Mo-Si-B system which is so called "Berczik triangle". Considering the ternary eutectic composition, besides the microstructure evolution in the ternary eutectic reaction, the growth stability of Mo-Si-B ternary eutectic lamellae has been investigated. The outcome of the phase-field simulations were compared to analytical expression of eutectic growth stability based on the expanded model of Jackson-Hunt theory. The phase-field simulations and developed model got further considered to investigate the solidification behavior of different alloy compositions. Moreover, the primary phase solidification and sequence of phase transition during the solidification of alloy with near-eutectic composition were investigated and the outcome of the proposed model showed appropriate compatibility with thermodynamic calculations and experimental investigations.

As a conclusion of the present thesis one can state that:

- It is feasible to simulate solidification of Mo-rich Mo-Si-B alloy through phase-field method. At the time of performing the present research, most of researches on the Mo-Si-B system have focused on devising alloy with desired properties experimentally. In order to develop a model which predicts the solidification behaviour including; microstructure evolution pattern, sequence of solidification reactions, phase arrangement and etc. a collection of thermodynamic and kinetic information of Mo-Si-B system is required. Lack of some these data such as diffusion coefficient of different elements inside the phases was one of the challenges of this research. However, by testing a wide range of feasible parameters, the approximate value of the required parameters was achieved.
- Microstructure evolution of the alloys during the solidification depends highly on the thermodynamics of the system. Regarding the nucleation and growth of the eutectic lamellae it is equitable but thermodynamic data is not the only influential parameter on stability and growth behavior of the eutectic solid phases. To have the precise control of the phase evolution in the system, other parameters such as solidification velocity should be controlled.
- Based on the Jackson-Hunt theory of eutectic growth stability and processors of this theory, there is a meaningful correlation between lamellae spacing, solidification velocity and undercooling at the solidification front. For the constant solidification velocities, stable eutectic lamellae growth happens at specific range of lamellae spacing which results in minimum under cooling at the solidification front. In this regard, a comprehensive amount of simulations were performed with different lamellae spacing for the constant velocity of solidification. It was observed that the most stable lamellae growth happens in the models which show minimum undercooling at the solidification front. Beside the phase-field simulations, an analytical approach to describe the correlation between velocity, lamellae spacing and undercooling for ternary eutectic reactions proposed by Choudhury et al. [114] was examined and accordance between the analytical approach and phase-field simulations' outcomes was observed.
- It might be very difficult to analyze the microstructure evolution and solidification path of the alloys with different compositions which perform primary solidification within 2D simulation domain. However, it was observed during the present research that considering the precise properties and parameters of the phase diagram would lead to an acceptable result. The microstructure evolution predicted by simulations were compared with available experimental data from literature and a good accordance between the simulations and experimental outcomes were found. Solidification path of every considered alloy was explored by monitoring the composition of the melt during the solidification. It was observed that formation of primary phase alters the chemical composition and consequently ratio

of the components of the melt so that the composition of the melt and subsequently the solidification path moves toward two-phase reaction. Comparing the predicted reactions with experimental observations has verified the reliability of outcomes of the developed model. Moreover, chemical composition of the phases was controlled to check the accuracy of the predicted phases.

A Initial temperature of the simulations

chemical composition of alloy (at.%)	initial temperature (K)
Mo-15.0Si-8.0B	2333
Mo-16.4Si-6.7B	2331
Mo-15.0Si-10.0B	2278
Mo-18.0Si-8.0B	2280
Mo-20.4Si-5.0B	2275
Mo-20.2Si-5.8B	2275

Table A.1: considered alloys and their corresponding initial temperature within the simulation domain (K) according to the thermodynamic data [78, 79].

B Additional simulation results

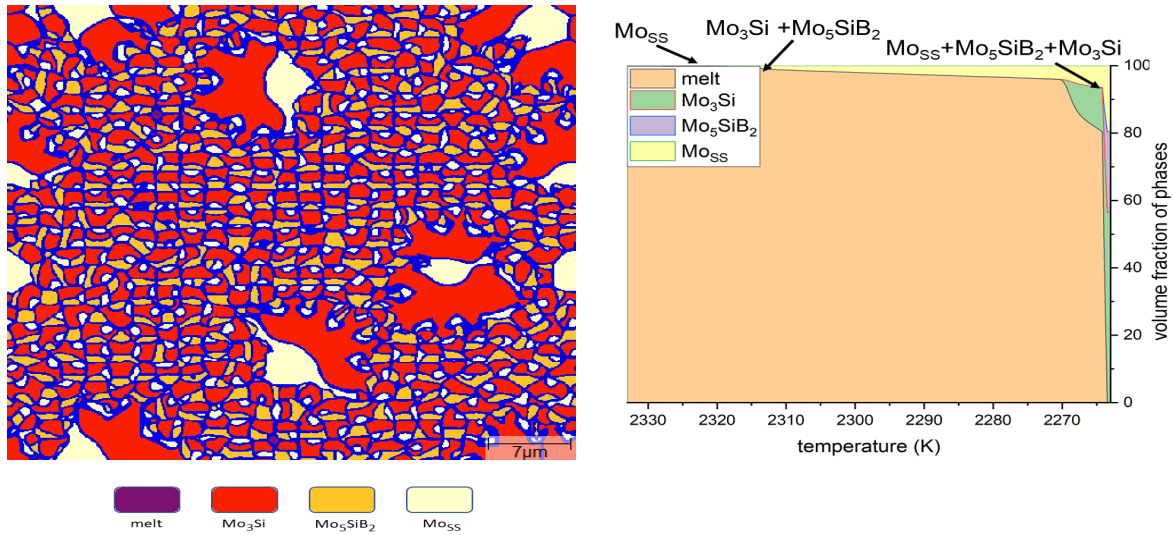


Figure B.1: Microstructure evolution and solidification reaction of Mo-18.3Si-4.7B (at.%) alloy composition.

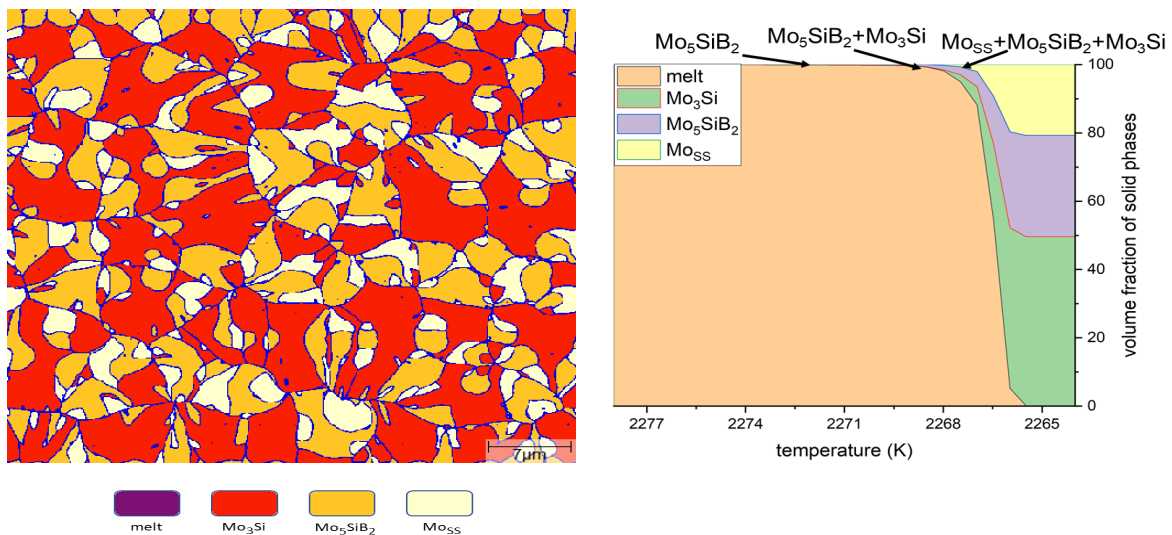


Figure B.2: Microstructure evolution and solidification reaction of Mo-16.9Si-7.4B (at.%) alloy composition.

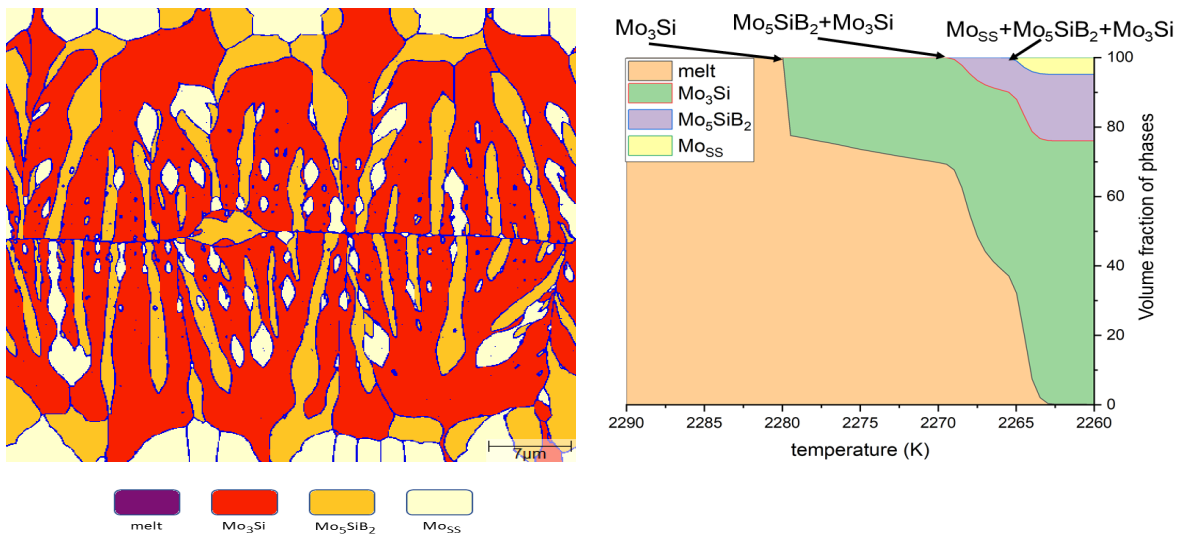


Figure B.3: Microstructure evolution and solidification reaction of Mo-21.3Si-4.7B (at.%) alloy composition.

Bibliography

- [1] Take a look under the hood of the gp7200. <https://www.enginealliance.com/gp7200/>, 2019.
- [2] J.H. Perepezko. The hotter the engine, the better. *Science*, 326(5956):1068–1069, 2009.
- [3] G.L. Erickson. The development of the cmsx-11b and cmsx-11c alloys for industrial gas turbine application. *Superalloys 1996*, pages 45–52, 1996.
- [4] Y. Koizumi. Development of next-generation ni-base single crystal superalloys. In *Proc. of the 10th International Symposium on Superalloys 2004*, 2004.
- [5] J.E. Jackson, D.L. Olson, B. Mishra, and A.N. Lasseigne-Jackson. Deposition and characterization of al–si metallic tbc precursor on mo–si–b turbine materials. *International journal of hydrogen energy*, 32(16):3789–3796, 2007.
- [6] J.A. Lemberg and R.O. Ritchie. Mo-si-b alloys for ultrahigh-temperature structural applications. *Advanced Materials*, 24(26):3445–3480, 2012.
- [7] A.P. Alur, N. Chollacoop, and K.S. Kumar. Creep effects on crack growth in a mo–si–b alloy. *Acta materialia*, 55(3):961–974, 2007.
- [8] K. Yoshimi, S. Nakatani, N. Nomura, and S. Hanada. Thermal expansion, strength and oxidation resistance of mo/mo₅sib₂ in-situ composites at elevated temperatures. *Intermetallics*, 11(8):787–794, 2003.
- [9] J. Cheng, S. Yi, and J.S. Park. Oxidation behaviors of nb–si–b ternary alloys at 1100° c under ambient atmosphere. *Intermetallics*, 23:12–19, 2012.
- [10] F. Gang, A. Kauffmann, and M. Heilmaier. Phase evolution in and creep properties of nb-rich nb-si-cr eutectics. *Metallurgical and Materials Transactions A*, 49(3):763–771, 2018.
- [11] A.A. da Silva, N. Chaia, F. Ferreira, G.C. Coelho, J.M. Fiorani, N. David, M. Vilasi, and C.A. Nunes. Thermodynamic modeling of the v-si-b system. *Calphad*, 59:199–206, 2017.
- [12] M. Krüger. High temperature compression strength and oxidation of a v-9si-13b alloy. *Scripta Materialia*, 121:75–78, 2016.
- [13] R.L. Fleischer. High-temperature, high-strength materials—an overview. *JOM*, 37(12):16–20, 1985.
- [14] R. Bürgel, R. Bürgel, H. Maier, and T. Niendorf. *Handbuch Hochtemperatur-Werkstofftechnik*. Springer, 1998.
- [15] P. Enghag. *Encyclopedia of the elements: technical data-history-processing-*

- applications*. John Wiley & Sons, 2008.
- [16] P. Jéhanno, M. Heilmaier, H. Saage, M. Böning, H. Kestler, J. Freudenberger, and S. Drawin. Assessment of the high temperature deformation behavior of molybdenum silicide alloys. *Materials Science and Engineering: A*, 463(1-2):216–223, 2007.
- [17] G. Hasemann, I. Bogomol, D. Schliephake, P.I. Loboda, and M. Krüger. Microstructure and creep properties of a near-eutectic directionally solidified multiphase mo–si–b alloy. *Intermetallics*, 48:28–33, 2014.
- [18] T.A. Parthasarathy, M.G. Mendiratta, and D.M. Dimiduk. Oxidation mechanisms in mo-reinforced mo₅sib₂ (t₂)–mo₃si alloys. *Acta Materialia*, 50(7):1857–1868, 2002.
- [19] M.G. Mendiratta, T.A. Parthasarathy, and D.M. Dimiduk. Oxidation behavior of α mo–mo₃si–mo₅sib₂ (t₂) three phase system. *Intermetallics*, 10(3):225–232, 2002.
- [20] Committee on Integrated Computational Materials Engineering. *Integrated computational materials engineering: a transformational discipline for improved competitiveness and national security*. National Academies Press Washington, DC, 2008.
- [21] J. Allison, D. Backman, and L. Christodoulou. Integrated computational materials engineering: a new paradigm for the global materials profession. *Jom*, 58(11):25–27, 2006.
- [22] Z.X. Guo. *Multiscale materials modelling: Fundamentals and applications*. Elsevier, 2007.
- [23] N. Provatas, J.A. Dantzig, B. Athreya, P. Chan, P. Stefanovic, N. Goldenfeld, and K.R. Elder. Using the phase-field crystal method in the multi-scale modeling of microstructure evolution. *Jom*, 59(7):83–90, 2007.
- [24] K.R. Elder and M. Grant. Modeling elastic and plastic deformations in nonequilibrium processing using phase field crystals. *Physical Review E*, 70(5):051605, 2004.
- [25] O. Kazemi, G. Hasemann, M. Krüger, and T. Halle. Phase field simulation of a directional solidification of a ternary eutectic mo–si–b alloy. In *IOP Conference Series: Materials Science and Engineering*, volume 118, page 012028. IOP Publishing, 2016.
- [26] O. Kazemi, G. Hasemann, M. Krüger, and T. Halle. Prediction of phase distribution pattern in phase field simulations on mo₅sib₂-primary areas in near eutectic mo–si–b alloy. In *IOP Conference Series: Materials Science and Engineering*, volume 181, page 012033. IOP Publishing, 2017.
- [27] M. Krüger, G. Hasemann, O. Kazemi, and T. Halle. Microstructure evolution of a directionally solidified ternary eutectic mo–si–b alloy. In *Materials Science*

- Forum*, volume 879, pages 1226–1232. Trans Tech Publ, 2017.
- [28] O. Sherepenko, O. Kazemi, P. Rosemann, M. Wilke, T. Halle, and S. Jüttner. Transient softening at the fusion boundary of resistance spot welds: a phase field simulation and experimental investigations for al–si-coated 22mnb5. *Metals*, 10(1):10, 2020.
- [29] A.A. Wheeler, N.A. Ahmad, W.J. Boettinger, R.J. Braun, G.B. McFadden, and B.T. Murray. Recent developments in phase-field models of solidification. *Advances in Space Research*, 16(7):163–172, 1995.
- [30] L.Q. Chen. Phase-field models for microstructure evolution. *Annual review of materials research*, 32(1):113–140, 2002.
- [31] W.J. Boettinger, J.A. Warren, C. Beckermann, and A. Karma. Phase-field simulation of solidification. *Annual review of materials research*, 32(1):163–194, 2002.
- [32] N. Moelans, B. Blanpain, and P. Wollants. An introduction to phase-field modeling of microstructure evolution. *Calphad*, 32(2):268–294, 2008.
- [33] I. Steinbach. Phase-field models in materials science. *Modelling and simulation in materials science and engineering*, 17(7):073001, 2009.
- [34] I. Singer-Loginova and H.M. Singer. The phase field technique for modeling multiphase materials. *Reports on progress in physics*, 71(10):106501, 2008.
- [35] D.M. Dimiduk, D.B. Miracle, and C.H. Ward. Development of intermetallic materials for aerospace systems. *Materials Science and Technology*, 8(4):367–375, 1992.
- [36] K. Takagi and Y. Yamasaki. Effects of mo/b atomic ratio on the mechanical properties and structure of mo₂nib₂ boride base cermets with cr and v additions. *Journal of Solid State Chemistry*, 154(1):263–268, 2000.
- [37] X. Chong, Y. Jiang, R. Zhou, and J. Feng. Stability, chemical bonding behavior, elastic properties and lattice thermal conductivity of molybdenum and tungsten borides under hydrostatic pressure. *Ceramics International*, 42(2):2117–2132, 2016.
- [38] M. Zhang, H. Yan, Q. Wei, and H. Wang. Pressure-induced phase transition and mechanical properties of molybdenum diboride: First principles calculations. *Journal of Applied Physics*, 112(1):013522, 2012.
- [39] D. Sturm, M. Heilmaier, J.H. Schneibel, P. Jéhanno, B. Skrotzki, and H. Saage. The influence of silicon on the strength and fracture toughness of molybdenum. *Materials Science and Engineering: A*, 463(1-2):107–114, 2007.
- [40] H. Saage, M. Krüger, D. Sturm, M. Heilmaier, J.H. Schneibel, E. George, L. Heatherly, C.h. Somsen, G. Eggeler, and Y. Yang. Ductilization of mo–si solid solutions manufactured by powder metallurgy. *Acta Materialia*, 57(13):3895–3901, 2009.
- [41] M. Meyer, M. Kramer, and M. Akinc. Boron-doped molybdenum silicides. *Ad-*

- vanced Materials*, 8(1):85–88, 1996.
- [42] M.K. Meyer and M. Akinc. Isothermal oxidation behavior of mo-si-b intermetallics at 1450° c. *Journal of the American Ceramic Society*, 79(10):2763–2766, 1996.
- [43] M.K. Meyer, M.J. Kramer, and M. Akinca. Compressive creep behavior of mo₅si₃ with the addition of boron. *Intermetallics*, 4(4):273–281, 1996.
- [44] M.K. Meyer, A.J. Thom, and M. Akinc. Oxide scale formation and isothermal oxidation behavior of mo–si–b intermetallics at 600–1000 c. *Intermetallics*, 7(2):153–162, 1999.
- [45] M. Akinc, M.K. Meyer, M.J. Kramer, A.J. Thom, J.J. Huebsch, and B. Cook. Boron-doped molybdenum silicides for structural applications. *Materials Science and Engineering: A*, 261(1-2):16–23, 1999.
- [46] P. Mandal, A.J. Thom, M.J. Kramer, V. Behrani, and M. Akinc. Oxidation behavior of mo–si–b alloys in wet air. *Materials Science and Engineering: A*, 371(1-2):335–342, 2004.
- [47] K. Yoshimi, S. Nakatani, T. Suda, S. Hanada, and H. Habazaki. Oxidation behavior of mo₅sib₂-based alloy at elevated temperatures. *Intermetallics*, 10(5):407–414, 2002.
- [48] F.A. Rioult, S.D. Imhoff, R. Sakidja, and J.H. Perepezko. Transient oxidation of mo–si–b alloys: effect of the microstructure size scale. *Acta Materialia*, 57(15):4600–4613, 2009.
- [49] R. Mitra. Mechanical behaviour and oxidation resistance of structural silicides. *International Materials Reviews*, 51(1):13–64, 2006.
- [50] D.M. Berczik. Oxidation resistant molybdenum alloy, December 2 1997. US Patent 5,693,156.
- [51] D.M. Berczik. Method for enhancing the oxidation resistance of a molybdenum alloy, and a method of making a molybdenum alloy, January 21 1997. US Patent 5,595,616.
- [52] J.H. Schneibel, M.J. Kramer, Ö. Ünal, and R.N. Wright. Processing and mechanical properties of a molybdenum silicide with the composition mo–12si–8.5 b (at.%). *Intermetallics*, 9(1):25–31, 2001.
- [53] S.H. Ha, K. Yoshimi, K. Maruyama, R. Tu, and T. Goto. Compositional regions of single phases at 1800° c in mo-rich mo–si–b ternary system. *Materials Science and Engineering: A*, 552:179–188, 2012.
- [54] H. Nowotny, E. Dimakopoulou, and H. Kudielka. Untersuchungen in den dreistoffsystemen: Molybdän-silizium-bor, wolfram-silizium-bor und in dem system: Vsi 2- tasi 2. *Monatshefte für Chemie und verwandte Teile anderer Wissenschaften*, 88(2):180–192, 1957.
- [55] R. Sakidja, J.H. Perepezko, S. Kim, and N. Sekido. Phase stability and structural

- defects in high-temperature mo–si–b alloys. *Acta Materialia*, 56(18):5223–5244, 2008.
- [56] D.M. Dimiduk and J.H. Perepezko. Mo-si-b alloys: developing a revolutionary turbine-engine material. *Mrs Bulletin*, 28(9):639–645, 2003.
- [57] J.H. Perepezko, R. Sakidja, and S. Kim. Phase stability in processing and microstructure control in high temperature mo-si-b alloys. *MRS Online Proceedings Library Archive*, 646, 2000.
- [58] A.B. Gokhale and G.J. Abbaschian. The mo-si (molybdenum-silicon) system. *Journal of Phase Equilibria*, 12(4):493–498, 1991.
- [59] N. Floquet, O. Bertrand, and J.J. Heizmann. Structural and morphological studies of the growth of mo₃ scales during high-temperature oxidation of molybdenum. *Oxidation of metals*, 37(3-4):253–280, 1992.
- [60] M Mousa, N Wanderka, M Timpel, S Singh, M Krüger, M. Heilmaier, and J. Banhart. Modification of mo–si alloy microstructure by small additions of zr. *Ultramicroscopy*, 111(6):706–710, 2011.
- [61] J. Becker and M. Krüger. Impact of phase distribution on the fracture toughness of high temperature resistant mo-si-b alloys. *Practical Metallography*, 52(6):295–313, 2015.
- [62] B. Aronsson. The crystal structure of mo₅sib₂. *Acta Chemica Scandinavica*, 12(1):31–37, 1958.
- [63] K. Ito, K. Ihara, K. Tanaka, M. Fujikura, and M. Yamaguchi. Physical and mechanical properties of single crystals of the t₂ phase in the mo–si–b system. *Intermetallics*, 9(7):591–602, 2001.
- [64] K. Ihara, K. Ito, K. Tanaka, and M. Yamaguchi. Mechanical properties of mo₅sib₂ single crystals. *Materials Science and Engineering: A*, 329:222–227, 2002.
- [65] I. Rosales, H. Martinez, D. Ponce, and J.A. Ruiz. Wear performance of nb-alloyed, pulsed plasma nitrided mo₃si intermetallic. *International Journal of Refractory Metals and Hard Materials*, 25(3):250–255, 2007.
- [66] J.G. Swadener, I. Rosales, and J.H. Schneibel. Elastic and plastic properties of mo₃si measured by nanoindentation. *MRS Online Proceedings Library Archive*, 646, 2000.
- [67] J. Xu, W. Hu, Y. Yan, X. Lu, P. Munroe, and Z.H. Xie. Microstructure and mechanical properties of a mo-toughened mo₃si-based in situ nanocomposite. *Vacuum*, 109:112–119, 2014.
- [68] I. Rosales and J.H. Schneibel. Stoichiometry and mechanical properties of mo₃si. *Intermetallics*, 8(8):885–889, 2000.
- [69] K.S. Kumar. Fatigue response of mo-si-b alloys. Technical report, BROWN UNIV PROVIDENCE RI DIV OF ENGINEERING, 2005.

- [70] H. Choe, D. Chen, J.H. Schneibel, and R.O. Ritchie. Ambient to high temperature fracture toughness and fatigue-crack propagation behavior in a mo–12si–8.5 b (at.%) intermetallic. *Intermetallics*, 9(4):319–329, 2001.
- [71] M. Gu, C. Huang, B. Zou, and B. Liu. Effect of (ni, mo) and tin on the microstructure and mechanical properties of tib2 ceramic tool materials. *Materials Science and Engineering: A*, 433(1-2):39–44, 2006.
- [72] L. Zhu, L. Luo, J. Li, and Y. Wu. The influence of powder characteristics on mechanical properties of al2o3–tic–co ceramic materials prepared by co-coated al2o3/tic powders. *International Journal of Refractory Metals and Hard Materials*, 34:61–65, 2012.
- [73] M. Krüger. *Pulvermetallurgische Herstellung und Charakterisierung von oxidationsbeständigen Molybdänbasislegierungen für Hochtemperaturanwendungen*. Logos, 2010.
- [74] S. Aryal, M.C. Gao, L. Ouyang, P. Rulis, and W.Y. Ching. Ab initio studies of mo-based alloys: Mechanical, elastic, and vibrational properties. *Intermetallics*, 38:116–125, 2013.
- [75] R. Sakidja and J.H. Perepezko. Phase stability and alloying behavior in the mo–si–b system. *Metallurgical and Materials Transactions A*, 36(3):507–514, 2005.
- [76] C.A. Nunes, R. Sakidja, Z. Dong, and J.H. Perepezko. Liquidus projection for the mo-rich portion of the mo–si–b ternary system. *Intermetallics*, 8(4):327–337, 2000.
- [77] S. Katrych, A. Grytsiv, A. Bondar, P. Rogl, T. Velikanova, and M. Bohn. Structural materials: metal–silicon–boron: on the melting behavior of mo–si–b alloys. *Journal of alloys and compounds*, 347(1-2):94–100, 2002.
- [78] Y. Yang. *Thermodynamic modeling and experimental investigation of the molybdenum-silicon-boron-titanium quaternary system*. The University of Wisconsin-Madison, 2004.
- [79] Y. Yang and Y.A. Chang. Thermodynamic modeling of the mo–si–b system. *Intermetallics*, 13(2):121–128, 2005.
- [80] S.H. Ha, K. Yoshimi, J. Nakamura, T. Kaneko, K. Maruyama, R. Tu, and T. Goto. Experimental study of moss–t2, moss–mo3si–t2, and mo3si–t2 eutectic reactions in mo-rich mo–si–b alloys. *Journal of alloys and compounds*, 594:52–59, 2014.
- [81] G. Hasemann, S. Ida, L. Zhu, T. Iizawa, K. Yoshimi, and M. Krüger. Experimental assessment of the microstructure evolution and liquidus projection in the mo-rich mo–si–b system. *Materials & Design*, 185:108233, 2020.
- [82] A.C. Van Rijn Van Alkemade. Graphical treatment of some thermodynamic problems with equilibrium states of salt solutions with solid phases. *Z. Phys. Chem*, 11:289–327, 1893.

-
- [83] P.G. Biragani and M. Heilmaier. Fem-simulation of real and artificial microstructures of mo-si-b alloys for elastic properties and comparison with analytical methods. *Advanced Engineering Materials*, 9(10):882–887, 2007.
- [84] K.A. Brindley, M.W. Priddy, and R.W. Neu. Integrative materials design of three-phase mo-si-b alloys. *Integrating Materials and Manufacturing Innovation*, 8(1):1–16, 2019.
- [85] C.P. Przybyla. *Microstructure-sensitive extreme value probabilities of fatigue in advanced engineering alloys*. Georgia Institute of Technology, 2010.
- [86] N.H. Paulson, M.W. Priddy, D.L. McDowell, and S.R. Kalidindi. Data-driven reduced-order models for rank-ordering the high cycle fatigue performance of polycrystalline microstructures. *Materials & Design*, 154:170–183, 2018.
- [87] V.L. Ginzburg and L.D. Landau. On the theory of superconductivity. *Zh. Eksp. Teor. Fiz.*, 20:1064–1082, 1950.
- [88] J.W. Cahn and J.E. Hilliard. Free energy of a nonuniform system. i. interfacial free energy. *The Journal of chemical physics*, 28(2):258–267, 1958.
- [89] J.S. Rowlinson. Translation of jd van der waals: The thermodynamik theory of capillarity under the hypothesis of a continuous variation of density. *Journal of Statistical Physics*, 20(2):197–200, 1979.
- [90] J.C. Toledano and P. Toledano. *The Landau theory of phase transitions: application to structural, incommensurate, magnetic and liquid crystal systems*, volume 3. World Scientific Publishing Company, 1987.
- [91] J.W. Cahn. Free energy of a nonuniform system. ii. thermodynamic basis. *The Journal of chemical physics*, 30(5):1121–1124, 1959.
- [92] J.W. Cahn and J.E. Hilliard. Free energy of a nonuniform system. iii. nucleation in a two-component incompressible fluid. *The Journal of chemical physics*, 31(3):688–699, 1959.
- [93] J.E. Hilliard and J.W. Cahn. On the nature of the interface between a solid metal and its melt. *Acta Metallurgica*, 6(12):772–774, 1958.
- [94] S.M. Allen and J.W. Cahn. A microscopic theory for antiphase boundary motion and its application to antiphase domain coarsening. *Acta metallurgica*, 27(6):1085–1095, 1979.
- [95] J.S. Langer. Models of pattern formation in first-order phase transitions. In *Directions in Condensed Matter Physics: Memorial Volume in Honor of Shang-Keng Ma*, pages 165–186. World Scientific, 1986.
- [96] G.J. Schmitz, B. Böttger, J. Eiken, M. Apel, A. Viardin, A. Carré, and G. Laschet. Phase-field based simulation of microstructure evolution in technical alloy grades. *International Journal of Advances in Engineering Sciences and Applied Mathematics*, 2(4):126–139, 2010.
- [97] A.A. Wheeler, W.J. Boettinger, and G.B. McFadden. Phase-field model for

- isothermal phase transitions in binary alloys. *Physical Review A*, 45(10):7424, 1992.
- [98] I. Steinbach, F. Pezzolla, B. Nestler, M. Seeßelberg, R. Prieler, G.J. Schmitz, and J.L.L. Rezende. A phase field concept for multiphase systems. *Physica D: Nonlinear Phenomena*, 94(3):135–147, 1996.
- [99] B. Nestler, H. Garcke, and B. Stinner. Multicomponent alloy solidification: phase-field modeling and simulations. *Physical Review E*, 71(4):041609, 2005.
- [100] S.G. Kim, W.T. Kim, and T. Suzuki. Interfacial compositions of solid and liquid in a phase-field model with finite interface thickness for isothermal solidification in binary alloys. *Physical Review E*, 58(3):3316, 1998.
- [101] J. Tiaden, B. Nestler, H.J. Diepers, and I. Steinbach. The multiphase-field model with an integrated concept for modelling solute diffusion. *Physica D: Nonlinear Phenomena*, 115(1-2):73–86, 1998.
- [102] J. Eiken, B. Böttger, and I. Steinbach. Multiphase-field approach for multi-component alloys with extrapolation scheme for numerical application. *Physical review E*, 73(6):066122, 2006.
- [103] M. Plapp. Unified derivation of phase-field models for alloy solidification from a grand-potential functional. *Physical Review E*, 84(3):031601, 2011.
- [104] J. Eiken. *A phase-field model for technical alloy solidification*. Shaker Verlag, 2009.
- [105] I. Steinbach and F. Pezzolla. A generalized field method for multiphase transformations using interface fields. *Physica D: Nonlinear Phenomena*, 134(4):385–393, 1999.
- [106] J.D. Hunt and K.A. Jackson. Binary eutectic solidification. *Trans. Metall. Soc. AIME*, 236(6):843–852, 1966.
- [107] J.D. Hunt and K.A. Jackson. Lamellar and rod eutectic growth. *Trans. Metall. Soc. AIME*, 236:1129–1142, 1966.
- [108] P. Atkins and J. De Paula. *Atkins’ physical chemistry*, 2006.
- [109] R. Vogel. Concerning eutectic crystallisation. *Zeitschrift Für Anorganische Chemie*, 76:425–436, 1912.
- [110] W.H. Brandt. Solution of the diffusion equation applicable to the edgewise growth of pearlite. *Journal of Applied Physics*, 16(3):139–146, 1945.
- [111] Dr.M Azim University of Siegen. Thermodynamic calculations using factsageTM. personal communication with Dr. G. Hasemann, University of Magdeburg.
- [112] W. Kurz and P.R. Sahm. *Gerichtet erstarrte eutektische Werkstoffe: Herstellung, Eigenschaften und Anwendungen von In-situ-Verbundwerkstoffen*. Springer, 1975.
- [113] S. Mazdiasni and D.B. Miracle. Survey of eutectic systems as potential in-

- termetallic matrix composites for high temperature application. *MRS Online Proceedings Library Archive*, 194, 1990.
- [114] A. Choudhury, M. Plapp, and B. Nestler. Theoretical and numerical study of lamellar eutectic three-phase growth in ternary alloys. *Physical Review E*, 83(5):051608, 2011.
- [115] K.A. Jackson and J.D. Hunt. Lamellar and rod eutectic growth. In *Dynamics of Curved Fronts*, pages 363–376. Elsevier, 1988.
- [116] T. Himemiya and T. Umeda. Three-phase planar eutectic growth models for a ternary eutectic system. *Materials Transactions, JIM*, 40(7):665–674, 1999.
- [117] T. Himemiya et al. Three-phase planar eutectic growth models with rod+hexagon or semi-regular structure for a ternary eutectic system. 1999.
- [118] S. Milenkovic, A.A. Coelho, and R. Caram. Directional solidification processing of eutectic alloys in the ni–al–v system. *Journal of crystal growth*, 211(1-4):485–490, 2000.
- [119] C.T. Rios, S. Milenkovic, S. Gama, and R. Caram. Influence of the growth rate on the microstructure of a nb–al–ni ternary eutectic. *Journal of crystal growth*, 237:90–94, 2002.
- [120] H. Bei, E.P. George, E.A. Kenik, and G.M. Pharr. Directional solidification and microstructures of near-eutectic cr–cr₃si alloys. *Acta materialia*, 51(20):6241–6252, 2003.
- [121] H. Bei and E.P. George. Microstructures and mechanical properties of a directionally solidified nial–mo eutectic alloy. *Acta Materialia*, 53(1):69–77, 2005.
- [122] S. Milenkovic and M. Palm. Microstructure and mechanical properties of directionally solidified fe–al–nb eutectic. *Intermetallics*, 16(10):1212–1218, 2008.
- [123] T. Haenschke, A. Gali, M. Heilmaier, M. Krüger, H. Bei, and E.P. George. Synthesis and characterization of lamellar and fibre-reinforced nial-mo and nial-cr. In *Journal of Physics: Conference Series*, volume 240, page 012063. IOP Publishing, 2010.
- [124] S. Milenkovic, A. Schneider, and G. Frommeyer. Constitutional and microstructural investigation of the pseudobinary nial–w system. *Intermetallics*, 19(3):342–349, 2011.
- [125] S. Milenkovic and R. Caram. Effect of the growth parameters on the ni–ni₃si eutectic microstructure. *Journal of crystal growth*, 237:95–100, 2002.
- [126] S.H. Davis. *Theory of solidification*. Cambridge University Press, 2001.
- [127] H. Bei, E.P. George, and G.M. Pharr. Effects of solidification parameters on lamellar microstructures of near eutectic cr–cr₃ si alloys. *MRS Online Proceedings Library Archive*, 753, 2002.
- [128] G. Duan and H.M. Wang. Microstructure of laser melted/rapidly solidified γ /cr₃

- si metal silicide “in situ” composites. *Journal of materials science*, 37(10):1981–1985, 2002.
- [129] S.G. Kim, W.T. Kim, T. Suzuki, and M. Ode. Phase-field modeling of eutectic solidification. *Journal of crystal growth*, 261(1):135–158, 2004.
- [130] D. West. *Ternary equilibrium diagrams*. Springer Science & Business Media, 2012.

Curriculum vitae

Omid Kazemi M.Sc.

Birth date/-place: 17.08.1987/ Amol-Iran

Address: Karl-hintze-weg 72, 38104 Braunschweig, Germany

Nationality: Iranian

Education

09/2006 – 07/2011 B.Sc., Material Science and Engineering,
University of Tehran, Iran

09/2011 – 06/2014 M.Sc., Material Science and Metallurgy Engineering,
Amirkabir University of Technology (Tehran Polytechnic), Iran

01/2015 – Present PhD, Institute for Material and Joining Technology,
University of Magdeburg, Germany, Group of
Prof. Dr.-Ing. habil. Halle and Prof. Dr.-Ing. habil. Krüger

Work Experience

06/2017 – 06/2020 Scientific researcher,
Institute for Material and Joining Technology,
University of Magdeburg, Germany

Omid Kazemi

Magdeburg, den 8. Februar 2021

Publications by the author

Peer-reviewed international journals:

- **Omid Kazemi**, Georg Hasemann, Manja Krüger, Thorsten Halle, “Microstructure evolution and sequence of phase transition reactions through the solidification of Mo-Si-B alloy; a phase-field study“, *Computational Materials Science*, under revision.
- Oleksii Sherepenko, **Omid Kazemi**, Paul Rosemann, Markus Wilke, Thorsten Halle, Sven Jüttner “Transient Softening at the Fusion Boundary of Resistance Spot Welds: A Phase Field Simulation and Experimental Investigations for Al-Si-coated 22MnB5“, *Metals*, 10(10), 2020.

Peer-reviewed proceedings:

- **Omid Kazemi**, Georg Hasemann, Manja Krüger, Thorsten Halle “Phase field simulation of a directional solidification of a ternary eutectic Mo-Si-B Alloy“, *IOP Conference Series Materials Science and Engineering*, 118 (1), 2016.
- Manja Krüger, Georg Hasemann, **Omid Kazemi**, Thorsten Halle “Microstructure Evolution of a Directionally Solidified Ternary Eutectic Mo-Si-B Alloy“, *Materials Science Forum*, 879: pages 1226-1232, Magdeburg, 2016.
- **Omid Kazemi**, Georg Hasemann, Manja Krüger, Thorsten Halle “Prediction of phase distribution pattern in phase field simulations on Mo₅SiB₂-primary areas in near eutectic Mo-Si-B alloy“, *IOP Conference Series Materials Science and Engineering*, 181 (1), 2017.

Omid Kazemi

Magdeburg, den 8. Februar 2021